STUDY OF PHOTONIC CRYSTAL STRUCTURES

BY THz-TDS

By

YUGUANG ZHAO

Bachelor of Science
Northwest Polytechnic University
Xi'an, China
1993

Master of Science
Rensselaer Polytechnic Institute
Troy, New York
2002

Submitted to the Faculty of the
Graduate College of the
Oklahoma State University
in partial fulfillment of
the requirements for
the Degree of
DOCTOR OF PHILOSOPHY
December, 2006

STUDY OF PHOTONIC CRYSTAL STRUCTURES

BY THz-TDS

Thesis Approved:

_____
Dr. Daniel Grischkowsky
Thesis Adviser

_____
Dr. Yumin Zhang

_____
Dr. Alan Cheville

_____
Dr. Bret Flanders

_____
Dr. Weili Zhang

_____
Dr. A. Gordon Emslie
Dean of the Graduate College

ACKNOWLEDGMENTS

First of all, I would like thank my major adviser, Dr. Daniel R. Grischkowsky, for sharing his unique view of science, for directing me to complete of the research, and for financial support throughout the study. Because of his distinguished contribution and as precursor in THz science, I am indebted to Dr. Grischkowsky for always standing at the front edge of the world in THz research.

I would also like to thank my co-adviser, Dr. Yumin Zhang, for introducing me to be a part of one of the best THz groups in the world, and for continuously encouraging and supporting me.

I extend my gratitude to Dr. Weili Zhang for many valuable discussions and advise from him. The talk and cooperation with him are a wonderful journey. I also need to thank him especially for his help in the semiconductor fabrication technique.

It is my pleasure to thank Dr. Alan Cheville, Dr. Bret Flanders, and Dr. Xincheng Xie, for serving in my advisory committee, and for their valuable time and suggestions.

I am also grateful to my colleagues, Abul Azad, Mufei Gong, Adam Bingham, Darpan Pradhan, Sharmila Rajendran and Sarika Atgur. Without their supporting, it is not easy to make experiments run smoothly.

To my family, my parents, my beloved wife, Kaiqian Li, and my lovely daughter, Keyla, I always cannot express enough thanks for their support in my life.

TABLE OF CONTENTS

Chapter	Page

LIST OF FIGURES

LIST OF THE SYMBOLS

α	absorption coefficient
ω	angular wave frequency
σ	complex conductivity
ε_c	complex dielectric constant
σ_{dc}	dc conductivity
ε_I	imaginary part of dielectric constant
ε_r	real part of dielectric constant
Δ	difference, usage as specified in text
1D	one-dimensional
2D	two-dimensional
3D	three-dimensional
a	lattice constant
Al	aluminum
Au	gold
B	magnetic flux density
c	speed of light in free space (2.998×10^8 m/s)
D	electric flux density
e	electric charge of an electron

E	electric field
E_x	Electric field amplitude in x-direction
E_y	Electric field amplitude in y-direction
E_z	Electric field amplitude in z-direction
FCC	face-centered cubic
FDTD	finite-difference time-domain
G	reciprocal vector
GaAs	Gallium Arsenide
GLAD	glancing angle deposition
H	magnetic field
H_x	Magnetic field amplitude in x-direction
H_y	Magnetic field amplitude in y-direction
H_z	Magnetic field amplitude in z-direction
J	current density
k	wave vector
k_x	wave vector in x-direction
k_y	wave vector in y-direction
k_z	wave vector in z-direction
LED	light-emitting diode
m^*	effective mass of electron
MEMS	micro-electro-mechanical-systems
N	free electron density
n	real part of refractive index

n_c	complex refractive index
n_i	imaginary part of refractive index
PBC	periodic boundary conditions
PBG	photonic band gap
PC	photonic crystal
PML	perfect matched layer
PPWG	parallel plate waveguide
PVD	physical vapor deposition
PWE	plane wave expansion
R	basis vector or primitive lattice vector
RIE	reactive ion etching
SEM	scanning electron microscope
Si	Silicon
t	time
T	transfer matrix
TE	transverse electric
TEM	transverse electromagnetic
THz	terahertz
THz-TDS	terahertz time-domain spectroscopy
TM	transverse magnetic
TMM	transfer matrix method
UV	ultra violet
ε	relative permittivity (dielectric constant)

ε_0	permittivity of vacuum, 8.85×10^{-12} F/m
λ	wavelength in free space
μ	relative permeability
μ_0	Permeability of vacuum, $4\pi \times 10^{-7}$ H/m
τ	carrier collision time
φ	phase angle, usage as specified in text (radians)
ω_τ	damping frequency
ω_p	plasma frequency

CHAPTER I

INTRODUCTION

The photonic crystal concept is originally from the solid state physics. As we all know, semiconductors have become very important materials in our daily life. The most critical property of a semiconductor is its energy gap or band structure. From the crystal structure map of a semiconductor such as a face-centered cubic lattice (FCC), we can see that the atoms are periodically arranged. Because of the periodic potential in this structure, the electrons can only occupy some certain energy bands that are separated by forbidden gaps. The energy versus effective momentum (E-k) relation shows the gaps very clearly. Analogically, if a material has periodic structure in space, a band structure is expected.

The study of periodic structured material can be traced to the nineteen century. Lord Rayleigh did some electromagnetic wave propagation experiments in one-dimensional media. In 1987, E. Yablonovitch and S. John proposed the concept of photonic crystals to summarize the periodic structured materials [1, 2]. Since then, the artificial photonic crystals have been studied intensively and great progress has been achieved. The developments of theories, experiments, fabrication techniques and applications of photonic crystals not only exist in the microwave and optical regions, but also extend to the infrared and far-infrared region, which includes the terahertz range.

1

1.1 Photonic Crystals

Photonic crystals, also named as photonic bandgap structures, are the materials with periodic structures that are formed naturally or artificially. The essential property of photonic crystals is the band gaps where light with certain wavelength cannot propagate through it. The photonic crystal can be divided into one-dimensional (1D), two-dimensional (2D) and three-dimensional (3D) structures [3]. Fig. 1-1 shows some schematic pictures of 1D, 2D and 3D photonic crystal structures. An example of 1D photonic structure is a dielectric mirror. The dielectric mirror consists of alternative layers with low and high refractive indices. 2D photonic crystals have periodicity along two axes, x and y. Along the z axis, the material is homogeneous. The pillar array and hole array are typical examples of a 2D photonic crystal. 3D photonic crystals have analogous structures as solid state crystals, such as semiconductors.

| 1D | 2D | 3D |
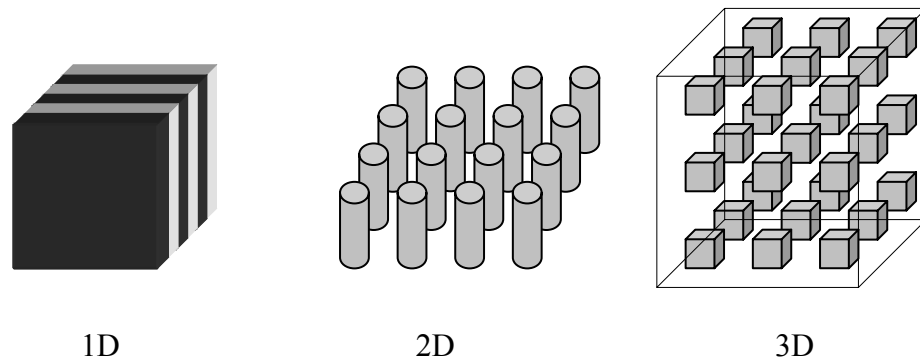
Figure 1-1. 1D, 2D and 3D photonic crystal structures

Because of the different properties of dielectrics and metal, the photonic crystals are also divided into dielectric photonic crystals and metallic photonic crystals [4]. In physics,

we know that microwaves propagate in metal waveguides or transmission lines while the optical, near infrared waves propagate in dielectric waveguides. The relative researches in different materials give us the information for applications [3].

The designed defect in photonic crystals is a very important issue. Most applications of photonic crystals are based on how to introduce the defects into the photonic crystals. By photonic crystals engineering, one can control, trap, or change the wave propagation. Basic photonic crystals defects have two types, point defect and line defect. The material property variation at one point or several points in the periodic structures forms the point defect. For example, in 2D photonic crystals, the usual methods to create defects include removing pillars, filling the holes, or changing the size of pillars or holes, etc. The point defect sometimes behaves like a cavity that has a very high Q factor. The line defects are sometimes treated as photonic crystal waveguide. The way to form line defects in 2D photonic crystals is by removing a line of pillars or filling holes. The wave modes within the photonic bandgap are confined in the photonic crystal waveguide. The bends made by photonic crystal waveguide have proved to be valuable. If the bends and photonic crystals are designed properly, certain frequency components can propagate with very low loss, even it has 90 degree bend [5].

In addition, some new physical phenomena appeared because of the photonic crystal structures. Negative refractive index, named left handed materials as well, was realized by periodic array of split ring resonators and continuous wires [6]. The optical diode, which has a unidirectional property, was demonstrated by nonlinear photonic crystals [7].
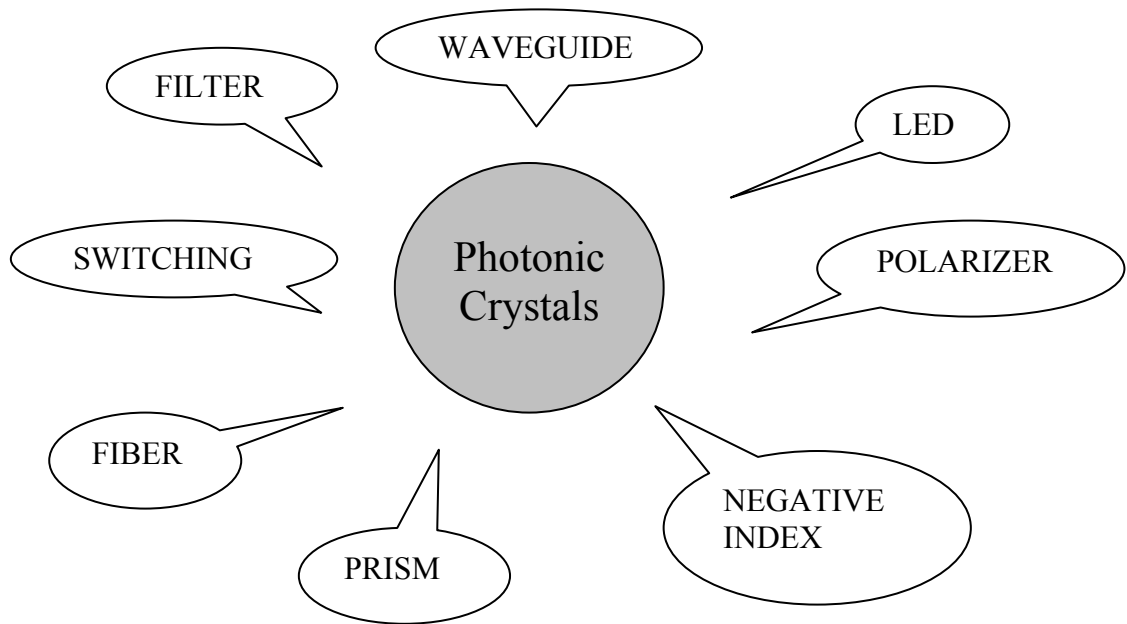
Figure 1-2. Applications of the photonic crystals

The photonic crystal products have been growing rapidly. After the early applications of highly reflecting mirrors and optical filters, the modern semiconductor lasers, photonic crystal fibers and high efficient LED emerge in the photonic market [3]. Some applications of photonic crystals are shown in Fig. 1-2.

1.2   Terahertz time-domain spectroscopy

Terahertz time-domain spectroscopy (THz-TDS) has demonstrated its powerful capability in material property characterization, imaging, ranging and sensing since the end of 1980s. THz-TDS can directly measure the electrical field of THz wave. The Fourier transform of this time domain data gives the amplitude and phase information of

the THz wave pulse, therefore, providing the wideband spectrum and the real and imaginary parts of the dielectric constant. This also allows precise measurements of the refractive index and absorption coefficient of samples [8, 9].
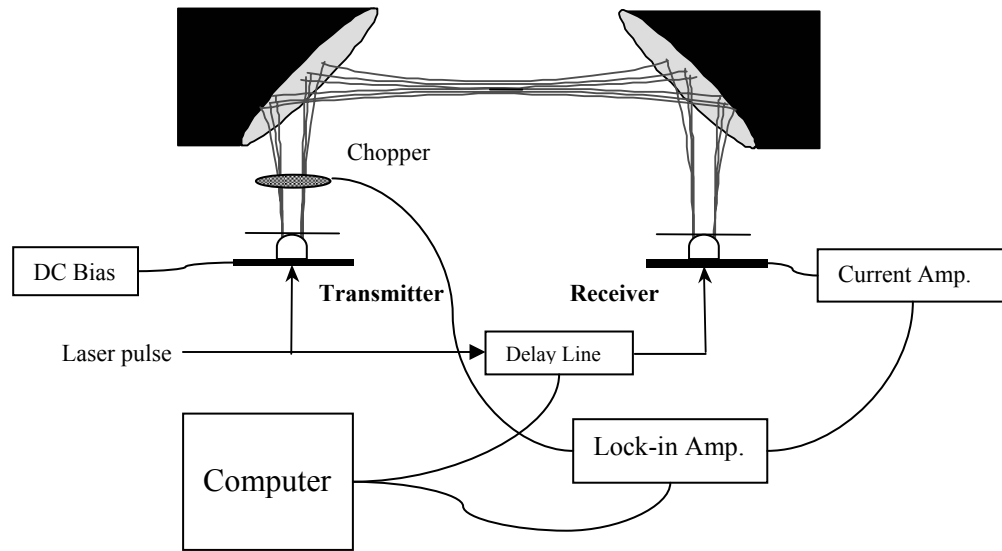
Figure 1-3. A typical THz-TDS system

A typical THz-TDS system is shown in Fig. 1-3 [8]. An ultrafast laser beam is split into two beams. One is the pump beam, which is employed to excite the transmitter. Another one is the probe beam for the receiver. The transmitter is based on photoconductive coplanar transmission lines and a high DC bias is applied between two transmission lines. Electron-hole pairs are created at one point between these two lines where it is bombarded by the ultra fast laser pulse. These free carriers are then accelerated in the static bias field to form a transient photocurrent, and this fast current radiates electromagnetic waves with the frequency just within the range of a few THz.

The THz radiation is collected by silicon lens that are attached on the back of chip, and then collimated by a paraboloidal mirror. Through the same structure with a paraboloidal mirror and silicon lens, the freely propagating THz radiation is collected by the receiver. The probe laser beam triggers the receiver's photo conductive switch and creates the current proportional to the amplitude of THz radiation received by the chip. By changing the path length of the probe laser beam, the time domain THz radiation pulse can be measured. The photo conductive switch is just like a sampling gate that opens for just several hundreds femtosecond signals. In this way, it is easy to get a THz pulse of time domain, as well as the frequency domain information by a Fourier transformation [8].

1.3   Progress in photonic crystals research in microwave and THz

   range

In order to understand the accomplishment and significance of the work presented in this thesis, we first review the microwave and THz experimental work on photonic crystals. This review section is similar to the review in Ref. 9. It is especially important to connect the recent THz work to the extensive microwave literature, because all of the THz guided wave demonstrations have their microwave counterparts, and because for both THz and microwaves the real part of the conductivity can be considered to be frequency independent and to be equal to the handbook dc value, in contrast to metallic conductivity at optical frequencies. Photonic crystals in the microwave and THz range

6

have been studied both experimentally [10-46], and theoretically [47-66] for more than a decade. Compared to microwaves, THz phenomena occur at a smaller spatial scale proportional to their shorter wavelengths. The corresponding frequency dependent losses are higher and the skin depths are smaller, but the basic phenomena are the same. The smaller THz spatial scale is especially convenient for the use of quasi-optics and associated techniques.

In contrast to the optical frequency range [67, 68], where submicron technology is needed to fabricate photonic structures, the microwave range allows for precise hand-assembly of photonic crystals composed of identical mm to cm sized components on repetitive lattice spacings with similar dimensions [10-46]. Most microwave photonic crystals have consisted of arrays of dielectric or metal spheres, arrays of cylinders, or arrays of square rods, sometimes supported by dielectric templates. These techniques have enabled the construction and experimental characterization of both two-dimensional (2D) [12-16, 23, 26, 29, 32, 34, 35, 37] and three-dimensional (3D) [17, 18, 20-22, 24, 25, 28, 33, 36, 43] photonic crystals. Typical photonic crystals are of the order of 10 lattice spacings long by 20 spacings wide with lattice spacings of the order of the wavelength. Although point source excitation and detection of the transmitted microwaves through the 3D photonic crystal was initially used with excellent results [11], more commonly, the crystals were characterized by input microwave beams with diameters smaller than the input face of the photonic crystal and radii of curvatures of several times the beam diameters. The first and quite notable 3D microwave characterization of photonic crystals [10, 11], reported the observation of a photonic band-gap between 13 and 16 GHz with a dynamic range of 50 dB and narrow donor and

acceptor modes with a dynamic range of 20 dB in a Yablonovitch type crystal made of Stycast dielectric. Ozbay's later approach of an orderly stacking of dielectric rods to fabricate 3D photonic crystals [17, 18], also enabled measurements of 3D photonic bandgaps between 12 and 14 GHz with a dynamic range of 50 dB and the observation of sharp defect structures with a dynamic range of 20 dB. Later the same approach, using metal rods, demonstrated a photonic bandgap with a dynamic range of 70 dB as well as a sharp defect line at 17.22 GHz with a dynamic range of 15 dB and a FWHM linewidth of 0.03 GHz [25].

The first precise microwave characterization of a 2D dielectric photonic crystal was reported in Ref. 12. The photonic crystal consisted of a 9 x 18 array of 1 cm long, 0.96 cm diameter alumina-composite cylinders on a square lattice with lattice constant 1.27 cm, as determined by a numerically drilled Styrofoam template. This structure was installed into a wide 2D parallel plate scattering chamber tapering to 8-12 GHz waveguide ports on each end. Here well defined photonic bandgaps were observed between 10 and 12 GHz with a dynamic range of 20 dB. Also, a sharp peak at 11.2 GHz was observed with a dynamic range of 10 dB due to a localized defect. An important advance at higher frequencies was the characterization from 15 to 150 GHz by Robertson [13] of a 2D dielectric array of long alumina-ceramic rods arranged in a square lattice. This measurement was made by transmitting the freely propagating and collimated beam from an optoelectronic source through the array. Photonic bandgaps were observed from 50 to 75 GHz with a dynamic range of 26 dB. Later work [23] with a 2D photonic crystal consisting of 10 cm long, 0.51 mm diameter cylinders of alumina-ceramic arranged in a square lattice with a lattice constant of 1.27 mm showed a deep photonic bandgap from

75-110 GHz. By removing two layers of cylinders from the middle of the photonic crystal, a quantum well type structure of barrier-well-barrier was produced [23]. For an optimum thickness of the barriers at 14 layers of cylinders, the quasi-bound state of the cavity was observed at 85.48 GHz with a linewidth of only 3.5 MHz corresponding to a cavity Q with the extraordinary value of 2.3×10^4 [23].

The photonic crystal research in THz region can be dated back to the early of 90's. The first 3D THz photonic crystal construction and characterization is described in Ref. 19. In this work, the crystal, built by the orderly stacking of dielectric rods, showed a photonic bandgap from 370 to 520 GHz with a dynamic range of 30 dB. In several years, the researches in terahertz region become more and more active. The subsequent THz characterization of a 2D metallic photonic crystal, consisting of a 2D honeycomb of metal 80 μm diameter cylinders threaded through two brass supporting meshes separated by 3 cm, was reported in Ref. 29. The measured transmission showed strong frequency dependence from 0.8 to 1.7 THz with a dynamic range of 10 dB. Another work measured THz phase shifts in a 2D photonic crystal fabricated by drilling holes in a methylpentene polymer [32]. Deep X-ray lithography has been used to fabricate 2D metallic photonic crystals, consisting of square and triangular lattices of nickel pillars [35]. For the square lattice of nickel pillars with a diameter of 26.4 μm and a lattice constant of 60 μm, transmission variations of 3 dB were observed from 1 to 6 THz [35]. In another THz experiment [38], metal 2D photonic crystals were constructed with nickel coated, 50 μm diameter silica cylinders confined and aligned between two parallel 70 μm square array brass meshes. Relatively sharp features were observed with the 2D crystal lattice constant of 140 μm. For a crystal length of 10 periods a 90 dB attenuation feature observed at 2.2

THz was identified as the center frequency of the photonic bandgap [38]. A THz 2D photonic crystal has been fabricated and characterized as a "Terahertz plasmonic high pass filter" [39]. This crystal was fabricated by layer-by-layer photopolymerization of UV curable resin, whereby the desired cross-section pattern was projected in UV light onto the resin. The resulting 2D photonic crystal consisted of 1 mm long, 30 μm diameter cylinders on a 120 μm square lattice, covered with a thin film of sputtered gold. The THz reflectivity was measured from 0.5 to 6 THz [39]. Deep reactive ion etching has also been used to fabricate a 2-D THz photonic crystal [40]. Here, 80 μm square holes on a 100 μm square lattice were etched through a 500 μm thick, high resistivity Si wafer. The resulting 2D slab waveguide showed a photonic bandgap from 0.9 to 1.2 THz with a dynamic range of 13 dB [40]. Recent work by Mittleman [42] has reported THz transmission studies of a hexagonal array of 360 μm diameter air holes with a 400 μm lattice constant in a 300 μm thick, high-resistivity silicon slab within a parallel plate metal waveguide. The THz-TDS characterization from 0.2 to 0.4 THz showed photonic bandgap features together with an observable defect mode in qualitative agreement with the transfer matrix method theory [47, 55].

Besides the investigation in theories and experiments, several groups also conduct research in some application areas. Frequency filtering is a basic application of photonic crystals due to the essential bandgap property. The general filter [69], high-pass filter [70] and tunable filter [71] are demonstrated in THz frequencies. The other applications include photonic crystal lens [72], photonic crystal waveguide [73], photonic fibers [74], THz generation [75], and biochemical sensing [76].

1.4　About this thesis

In this thesis, the study of THz photonic crystal structures will be discussed including theories, fabrication, experiments, and applications. Chapter 2 describes the theories of band structure of photonic crystals, the methods to calculate the photonic crystals and the Drude model of material that is used in analysis. Chapter 3 talks about the fabrication of the Micro-Electro-Mechanical-Systems (MEMS) with lithography method, as well as the back-end process, such as dicing. Chapter 4 describes the setup of our experiment system and the advantage of the setup. Chapter 5 shows and explains the results of a series of basic photonic crystal experiments. The results of the SU-8 (polymer) photonic crystals, metallic photonic crystals and metallic photonic crystals with defects are demonstrated and compared to the computation results. The good agreement indicates the success of experiment setup and sample quality. Chapter 6 discusses some applications of the THz photonic crystals. THz photonic crystal waveguide and tunable photonic bandgap structures are realized and demonstrated. Chapter 7 summarizes the whole thesis.

CHAPTER II

RELATED THEORIES

2.1 Basic analysis of photonic crystals

The fundamental theory of the band structure of photonic crystals is Maxell's equations. First, we need to know how the field in the media is determined.

Faraday's law: $\nabla \times \vec{E} = -\dfrac{\partial \vec{B}}{\partial t}$ (1)

Ampere's law: $\nabla \times \vec{H} = \vec{J} + \dfrac{\partial \vec{D}}{\partial t}$ (2)

For a source free field,

$\vec{J} = 0$

$\vec{B} = \mu_0 \vec{H}$ (μ=1 for most materials)

and $\vec{D} = \varepsilon \varepsilon_0 \vec{E}$

And we assume the field has harmonic time dependence, $e^{-i\omega t}$

$\nabla \times \vec{E} = i\omega \mu_0 \vec{H}$ (3)

$\nabla \times \vec{H} = -i\omega \varepsilon \varepsilon_0 \vec{E}$ (4)

We know the speed of light $c = \dfrac{1}{\sqrt{\varepsilon_0 \mu_0}}$, from (3) and (4), we get

$$\nabla \times (\frac{1}{\varepsilon} \nabla \times \vec{H}) = \frac{\omega^2}{c^2} \vec{H} \tag{5}$$

Consider (5) plus the condition $\nabla \cdot \vec{H} = 0$, we can solve this eigenvalue problem and find $\vec{H}$. In addition, $\vec{E}$ can be obtained from (4). [3]

But the solutions of the fields are not enough. There are mainly three supporting concepts used in band structure calculation of photonic crystals, Bloch's theorem, the reciprocal lattice and the Brillouin zone.

In typical photonic crystals, the materials are periodically distributed. We have $\varepsilon(r)$ $=\varepsilon(r+a)$, and here a is the periodic constant. Bloch's theorem states the wave in such material governed by a periodic envelope function multiplied by a plane wave. So the solution of (5) can be chosen as $\vec{H}(x) = e^{ikx} \vec{H}_{n,k}(x)$ with eigenvalue $\omega_n(k)$.

The reciprocal lattice describes a function such as $f(r)=f(r+R)$ in the periodic lattice induces $exp(iG{\cdot}R)=1$. The vector G, which defined by $G{\cdot}R=n2\pi$, is called reciprocal vector. The basis vectors in the lattice are R_1, R_2 and R_3, which are also termed as primitive lattice vectors. The reciprocal lattice vectors are defined by:

$$G_1 = 2\pi \frac{R_2 \times R_3}{R_1 \bullet R_2 \times R_3} \tag{6}$$

$$G_2 = 2\pi \frac{R_3 \times R_1}{R_1 \bullet R_2 \times R_3} \tag{7}$$

$$G_3 = 2\pi \frac{R_1 \times R_2}{R_1 \bullet R_2 \times R_3} \tag{8}$$

For the eigensolutions of $\omega_n(k)$, the solutions are the same at wave vector k or at k+G. This result suggests that the computation of the eigensolutions only needs to conduct in the primitive cell of reciprocal lattice [3]. Moreover, the wave vector k can be limited in the first Brillouin zone. Fig. 2-1 shows the band structure of silicon pillars with square arrangement. The band gap between 0.28 and 0.42 is very clear in this figure. [77]. The lines in the figure represent the eigensolutions along the edge of the first Brillouin zone.
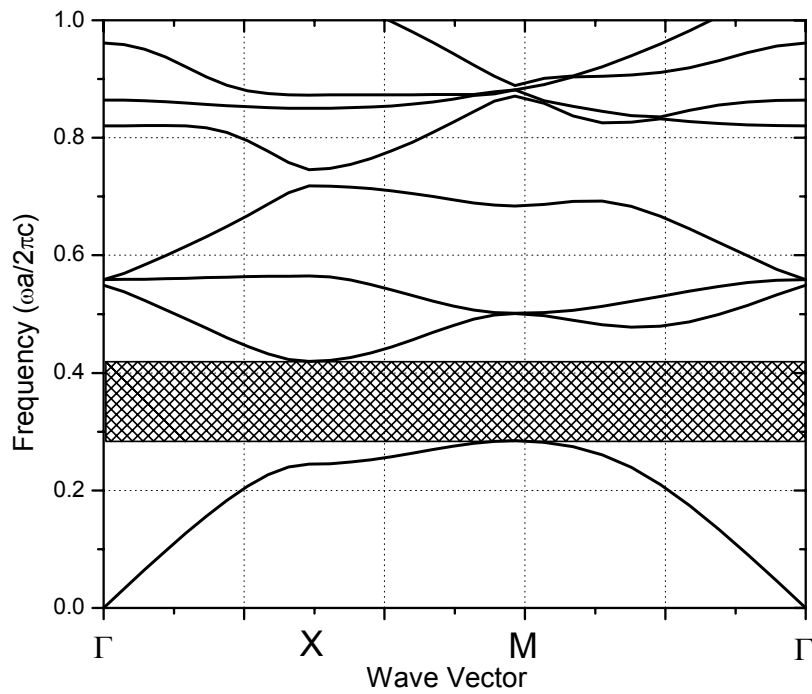
Figure 2-1. TM Band structure of 2D square silicon cylinder array with ε=11.7 and r/a=0.2, calculated by plane wave expansion method.

The band structure in Fig. 2-1 is calculated by plane wave expansion (PWE) method. For most dielectric structures without loss or with neglected loss, PWE is powerful tool to get band structure with very fast speed. The limitation of the PWE method is that cannot treat dispersion and loss problems, especially for metallic structures.

The calculation methods of band structure have been developed very fast in recent years and many practical theories are proved by many experiments. The main methods not only include PWE method [77], but also include the multi-scattering method, the transfer matrix method (TMM) [47, 55, 65], the finite difference time domain (FDTD) method [63, 64, 78] and so on. Each method has its advantages in solving certain types of band structure. Among these methods, FDTD and TMM are the most popular methods.

2.2   Finite Difference Time Domain (FDTD) method

In 1966, Kane S. Yee introduced this method [78], since then FDTD become very popular method to solve various electromagnetic problems, which include photonic crystal problems.

FDTD method is direct solution from Maxwell's time dependent curl equations.

$$\frac{\partial H_x}{\partial t} = -(\frac{\partial E_z}{\partial y} - \frac{\partial E_y}{\partial z})\frac{1}{\mu} \qquad (9)$$

$$\frac{\partial H_y}{\partial t} = -(\frac{\partial E_x}{\partial z} - \frac{\partial E_z}{\partial x})\frac{1}{\mu} \qquad (10)$$

$$\frac{\partial H_z}{\partial t} = (\frac{\partial E_x}{\partial y} - \frac{\partial E_y}{\partial x})\frac{1}{\mu} \qquad (11)$$

$$\frac{\partial E_x}{\partial t} = (\frac{\partial H_z}{\partial y} - \frac{\partial H_y}{\partial z})\frac{1}{\varepsilon} \qquad (12)$$

$$\frac{\partial E_y}{\partial t} = (\frac{\partial H_x}{\partial z} - \frac{\partial H_z}{\partial x})\frac{1}{\varepsilon} \qquad (13)$$

$$\frac{\partial E_z}{\partial t} = (\frac{\partial H_y}{\partial x} - \frac{\partial H_x}{\partial y}) \frac{1}{\varepsilon} \tag{14}$$

Then the finite differential equations are constructed according to (9) to (14).

$$\frac{H_x^{n+1/2}(i, j+\frac{1}{2}, k+\frac{1}{2}) - H_x^{n-1/2}(i, j+\frac{1}{2}, k+\frac{1}{2})}{\Delta t} = \frac{E_y^n(i, j+\frac{1}{2}, k+1) - E_y^n(i, j+\frac{1}{2}, k)}{\mu \Delta z} \tag{15}$$
$$- \frac{E_z^n(i, j+1, k+\frac{1}{2}) - E_z^n(i, j, k+\frac{1}{2})}{\mu \Delta y}$$

$$\frac{E_x^n(i+\frac{1}{2}, j, k) - E_x^{n-1}(i+\frac{1}{2}, j, k)}{\Delta t} = \frac{H_z^{n-1/2}(i+\frac{1}{2}, j+\frac{1}{2}, k) - H_z^{n-1/2}(i+\frac{1}{2}, j-\frac{1}{2}, k)}{\varepsilon \Delta y} \tag{16}$$
$$- \frac{H_y^{n-1/2}(i+\frac{1}{2}, j, k+\frac{1}{2}) - H_y^{n-1/2}(i+\frac{1}{2}, j, k-\frac{1}{2})}{\varepsilon \Delta z}$$

(15) and (16) are differential equations of H_x and E_x. Other equations can be obtained by exchanging the x, y and z subscripts. The differential equations are divided into finite difference equivalents in a grid of space Δx, Δy, and Δz, and time nodes Δt. One equivalent in one grid point is related to the neighbor grid point.

To numerically simulate the results, some numerical parameters are required. For basic FDTD problem, a finite domain, a boundary condition, and spatial and temporal grids are defined before the simulation. Perfect matched layer (PML) is the most common boundary condition FDTD method used. Both electric and magnetic conductivities remains constant at PML and the energy is absorbed without reflection. However, periodic boundary conditions (PBC) are employed for photonic crystal simulation. PBC is chosen to ensure the equivalent infinite repeated structures. The spatial and temporal

grids are chosen small enough to produce accurate simulation. The stability of simulation depends on the relationship of spatial and temporal grids.

$$\frac{1}{\sqrt{(1/\Delta x)^2 + (1/\Delta y)^2 + (1/\Delta z)^2}} > c\Delta t \qquad (17)$$

The denser the grid points in the FDTD problem, the more exact solutions it has. The time and memory consuming will increase significantly as well with small grid. The development of various FDTD methods allows calculating some complicated cases such as metallic or metallo-dielectric photonic crystals [63, 64].
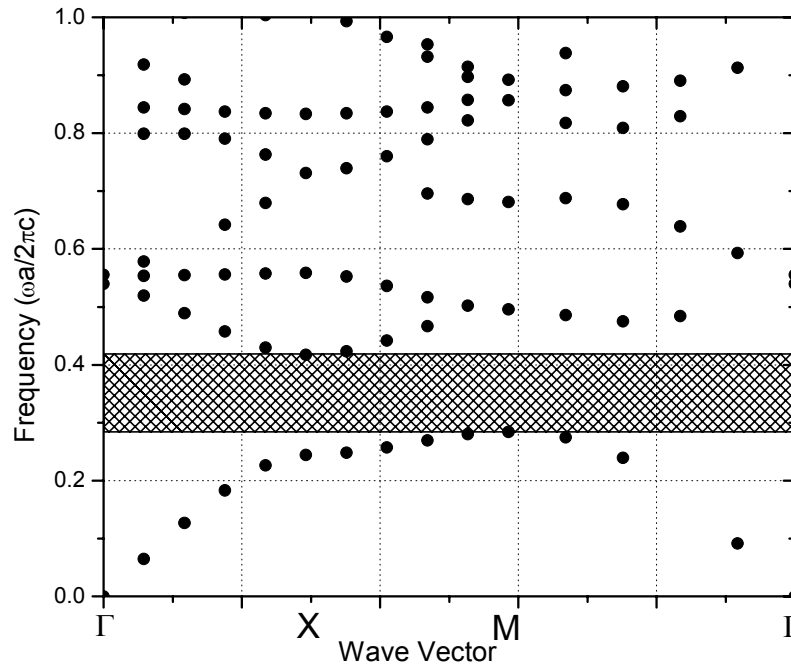
Figure 2-2. TM Band structure of 2D square silicon cylinder array with $\varepsilon=11.7$ and $r/a=0.2$, calculated by FDTD method.

Fig. 2-2 gives a band structure example of the same 2D Si photonic crystals as Fig. 2-1. It shows that there is same band gap between 0.28(c/a) to 0.42(c/a).

There are some commercial softwares (such as Rsoft) and free softwares (such as F2P) available to calculate and design photonic crystals.

2.3   Transfer Matrix Method (TMM)

Transfer Matrix Method for photonic crystals calculation is developed by J.B. Pendry et. al. [47]. This method can handle most photonic crystal structures, including the photonic crystal defects and the metallic photonic crystals [55].

Given the field in one point, let's say at (x1, y1, z1), by solving the Maxwell's equations, the field in another point at (x2, y2, z2) can be calculated when they are in the same space and other conditions such as materials are known. If we make it a little simple and suppose the x and y are fixed, only the z changes from 0 to a.

If $F(z=0)=(Ex,Ey,Hx,Hy)$ at z=0

and $F(z=a)=(Ex,Ey,Hx,Hy)$ at z=a

We get

$$F(z=a)=T(a,0)F(z=0)$$

Here T is defined as transfer matrix.

T(a,0) can be treated as a matrix of combining of transmission and reflection coefficients in photonic system. In photonic crystals, because of the periodic structures, we can apply the Bloch condition in this equation.

$$F(z=0)e^{ik(\omega)a}=F(z=a)=T(a,0)F(z=0) \quad \text{So,} \quad T(a,0)=e^{ik(\omega)a}$$

So the band structure k(ω) is from the calculation of eigenvalues of T(a,0).

The detail description from Ref. 55 of TMM is below.

By taking Fourier transform to (1) and (2), we get

$$\vec{k} \times \vec{E} = \omega \vec{B} \tag{18}$$

$$\vec{k} \times \vec{H} = -\omega \vec{D} \tag{19}$$

Here, the approximations are made for (18)

$$k_x \approx (\exp(ik_x a) - 1)/ia = k_x^E$$

$$k_y \approx (\exp(ik_y b) - 1)/ib = k_y^E \tag{20}$$

$$k_z \approx (\exp(ik_z c) - 1)/ic = k_z^E$$

and for (19)

$$k_x \approx -(\exp(-ik_x a) - 1)/ia = k_x^H$$

$$k_y \approx -(\exp(-ik_y b) - 1)/ib = k_y^H \tag{21}$$

$$k_z \approx -(\exp(-ik_z c) - 1)/ic = k_z^H$$

Where a, b, c are vectors in x, y, z directions. These approximations are based on the difference equations in real space [47, 55].

$$a^{-1}[E(r + ax) - E(r)] \leftrightarrow [(\exp(ik_x a) - 1)/ia]E(k) \quad \text{etc.} \tag{22}$$

$$\text{real space} \quad \leftrightarrow \quad (k, \omega) \text{ space}$$

From the above approximations, bring (20) and (21) to (18) and (19), we get

$$\{k_x^E, k_y^E, k_z^E\} \times \{E_x, E_y, E_z\} = \begin{vmatrix} ia & ib & ic \\ k_x^E & k_y^E & k_z^E \\ E_x & E_y & E_z \end{vmatrix} = \omega \vec{B} \tag{23}$$

$$\left\{ k_x^H, k_y^H, k_z^H \right\} \times \left\{ H_x, H_y, H_z \right\} = \begin{vmatrix} ia & ib & ic \\ k_x^H & k_y^H & k_z^H \\ H_x & H_y & H_z \end{vmatrix} = -\omega \vec{D} \qquad (24)$$

Transform (23) and (24) to real space by relationship of (22) and eliminate z-components, we get

$$E_x(r+c) = E_x(r) + \frac{c^2\omega^2}{c_0^{\,2}}\mu(r)H_y{'}(r) + \frac{c^2}{a\varepsilon(r)}\left[\frac{H_y{'}(r-a)-H_y{'}(r)}{a} - \frac{H_x{'}(r-b)-H_x{'}(r)}{b} \right]$$

$$-\frac{c^2}{a\varepsilon(r+a)}\left[\frac{H_y{'}(r)-H_y{'}(r+a)}{a} - \frac{H_x{'}(r+a-b)-H_x{'}(r+a)}{b} \right]$$

$$E_y(r+c) = E_y(r) + \frac{c^2\omega^2}{c_0^{\,2}}\mu(r)H_x{'}(r) + \frac{c^2}{b\varepsilon(r)}\left[\frac{H_y{'}(r-a)-H_y{'}(r)}{a} - \frac{H_x{'}(r-b)-H_x{'}(r)}{b} \right]$$

$$-\frac{c^2}{b\varepsilon(r+b)}\left[\frac{H_y{'}(r-a+b)-H_y{'}(r+b)}{a} - \frac{H_x{'}(r)-H_x{'}(r+b)}{b} \right]$$

$$(25)$$

$$H_x{'}(r+c) = H_x{'}(r) + \varepsilon(r+c)E_y(r+c)$$

$$-\frac{c_0^{\,2}}{a\omega^2\mu(r-a+c)}\left[\frac{E_y(r+c)-E_y(r-a+c)}{a} - \frac{E_x(r-a+b+c)-E_x(r-a+c)}{b} \right]$$

$$+\frac{c_0^{\,2}}{a\omega^2\mu(r+c)}\left[\frac{E_y(r+a+c)-E_y(r+c)}{a} - \frac{E_x(r+b+c)-E_x(r+c)}{b} \right]$$

$$H_y{'}(r+c) = H_y{'}(r) - \varepsilon(r+c)E_x(r+c)$$

$$-\frac{c_0^{\,2}}{b\omega^2\mu(r-b+c)}\left[\frac{E_y(r+a-b+c)-E_y(r-b+c)}{a} - \frac{E_x(r+c)-E_x(r-b+c)}{b} \right]$$

$$+\frac{c_0^{\,2}}{b\omega^2\mu(r+c)}\left[\frac{E_y(r+a+c)-E_y(r+c)}{a} - \frac{E_x(r+b+c)-E_x(r+c)}{b} \right]$$

$$(26)$$

Where $\vec{H}{'} = \dfrac{i}{c\omega\varepsilon_0}\vec{H}$ and $c_0^{\,2} = \dfrac{1}{\varepsilon_0\mu_0}$.

So if we know the E and H field on one side of the structure, from above equations, the field on the other side can be decided.

The transfer matrix is

$$\begin{bmatrix} E_x(r+c) \\ E_y(r+c) \\ H_x(r+c) \\ H_y(r+c) \end{bmatrix} = \sum_{r'} \begin{bmatrix} T_{11}(r,r') & T_{12}(r,r') & T_{13}(r,r') & T_{14}(r,r') \\ T_{21}(r,r') & T_{22}(r,r') & T_{23}(r,r') & T_{24}(r,r') \\ T_{31}(r,r') & T_{32}(r,r') & T_{33}(r,r') & T_{34}(r,r') \\ T_{41}(r,r') & T_{42}(r,r') & T_{43}(r,r') & T_{44}(r,r') \end{bmatrix} \begin{bmatrix} E_x(r') \\ E_y(r') \\ H_x(r') \\ H_y(r') \end{bmatrix} \qquad (27)$$

For photonic crystals, the periodicity is L*c, so

$$\begin{bmatrix} E_x(r+Lc) \\ E_y(r+Lc) \\ H_x(r+Lc) \\ H_y(r+Lc) \end{bmatrix} = \sum_{r'} T(L,0) \begin{bmatrix} E_x(r') \\ E_y(r') \\ H_x(r') \\ H_y(r') \end{bmatrix} \qquad (28)$$

where $T(L,0) = \prod_{j=1}^{L} T(j, j-1)$

Apply Bloch's theorem,

$$\sum_{r'} T(L,0) \begin{bmatrix} E_x(r') \\ E_y(r') \\ H_x(r') \\ H_y(r') \end{bmatrix} = \exp(iK_z La) \begin{bmatrix} E_x(r) \\ E_y(r) \\ H_x(r) \\ H_y(r) \end{bmatrix} \qquad (29)$$

At a given frequency, we can calculate the eigenvalues and get the entire Bloch wave. The advantage of TMM is that the calculation is from a given frequency to find the field and corresponding coefficients. Because the dielectric constant is fixed at a given frequency, this makes calculation of the frequency dependent materials very simple.
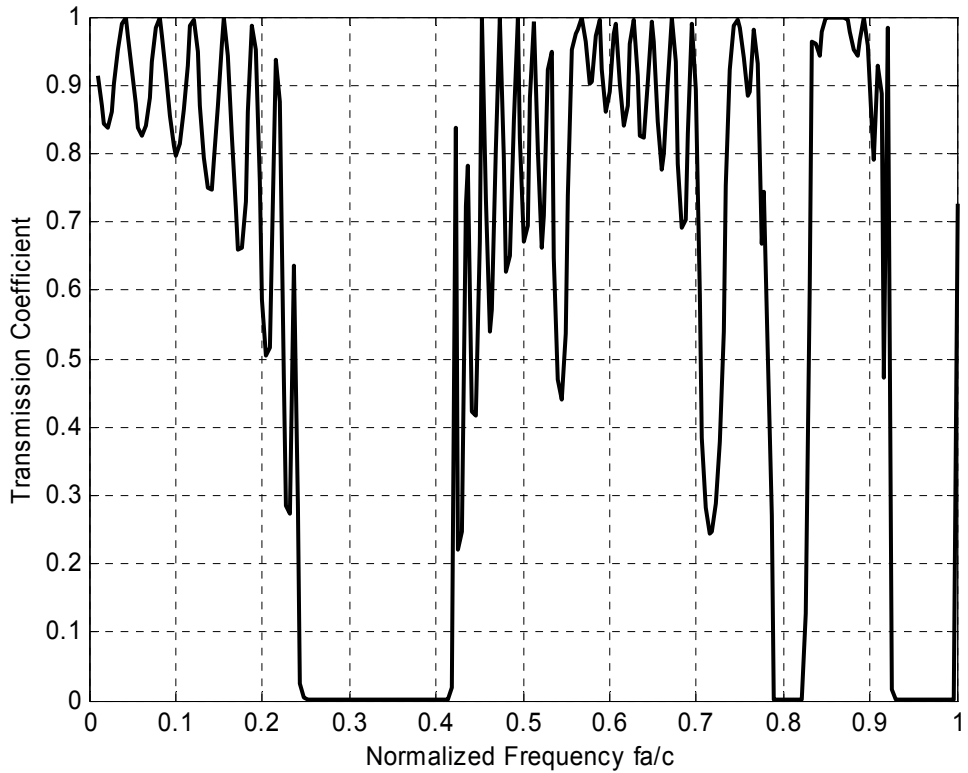
Figure 2-3. Transmission coefficient of normal incidence (TM) on 8 columns 2D square silicon cylinder array with ε=11.7 and r/a=0.2, Calculated by TMM.

Fig. 2-3 shows the transmission of a 2D photonic crystal calculated by TMM [65]. The incident direction of wave is (10) of square lattice. The first band gap is from 0.24(a/c) to 0.42(a/c). Some softwares were developed to apply this powerful method, and they include 'PHOTON' of P. M. Bell et. al. and 'Translight' of A. L. Reynolds.

2.4 Complex dielectric constant and Drude model

To analyze the properties of dielectric and metallic photonic crystal structures, the dielectric constant plays a very important role.

The dielectric constant is one of the primary properties of materials. Any material has the dielectric constant, which is usually frequency and temperature dependent. The dielectric constants of insulator, semiconductor and metal have huge difference.

The refractive index, which is popular in wave or optical analysis, is related to the dielectric constant as below.

$$\varepsilon_c = \varepsilon_r + i\varepsilon_i$$

$$n_c = n + in_i$$

$$\varepsilon_c = n_c^2 = (n + in_i)^2 \tag{30}$$

Where, ε_c is the complex dielectric constant, ε_r is the real part of dielectric constant, ε_i is the imaginary part of dielectric constant, n_c is the complex refractive index, n is the refractive index, and n_i is the extinction index.

The relationship between the absorption coefficient α and the imaginary part of refractive index n_i is

$$\alpha = 4\pi n_i / \lambda_0 \tag{31}$$

For frequency-dependent materials such as metals, Drude model fits most of them [80]. The simple Drude model treats the free carriers in a metal as classical point charges with random collisions. The collision damping is independent of the carrier velocity. The Drude model is

$$\varepsilon_c = \varepsilon_\infty + i\sigma /(\varepsilon_0 \omega) = \varepsilon_\infty - \omega_p^2 /(\omega^2 + i\omega\omega_\tau) \tag{32}$$

ε_∞ is the high frequency dielectric constant and is the contribution of the bound electrons.

ω_p is the plasma frequency of materials. It is a basic parameter of materials.

$$\omega_p = (\frac{Ne^2}{m^* \varepsilon_\infty})^{1/2} \qquad (33)$$

N is the free electron density, e is electron charge, m^* is the effective mass of electrons, and c is the velocity of light.

ω_τ is the damping frequency.

$$\omega_\tau = \frac{1}{\tau} \qquad (34)$$

τ is the electron lifetime.

$$\varepsilon_r = \varepsilon_\infty - \frac{\omega_p^3}{\omega^3 + \omega\omega_\tau^2} \qquad (35)$$

$$\varepsilon_i = \frac{\omega_p^2 \omega_\tau}{\omega^3 + \omega\omega_\tau^2} \qquad (36)$$

The complex conductivity can be given by

$$\sigma = \sigma_{dc} i\omega_\tau /(\omega + i\omega_\tau) = i\varepsilon_0 \omega_p^2 /(\omega + i\omega_\tau) \qquad (37)$$

The plasma frequency and damping frequency are usually fixed for the materials. If the absorption coefficient or refractive index with frequency dependence can be measured, the measurement results can be compared with the theoretical results [79].

CHAPTER III

FABRICATION OF THZ PHOTONIC CRYSTAL STRUCTURES

3.1 Introduction of fabrication methods for THz Photonic crystal structures

Photonic crystals in the real world are not as easy to obtain as semiconductors, which are extracted from sands and minerals by chemical or physical methods. The photonic crystals range from microwave to optical frequency and can only be obtained by artificial fabrication.

For microwave photonic crystals, the fabrication methods are not very complicated because the scale range is in the range of several millimeters. We can employ mechanical machining methods such as drilling, dicing, polishing and molding to fabricate the photonic structures [3]. When the scale is down to sub-millimeter or micrometer, the methods in semiconductor industry are used frequently. Lithography, etching, deposition, and oxidation are popular fabrication techniques of photonic crystals in this scale [80].

The fabrication methods used in THz region still concentrate in semiconductor manufacturing techniques, because the structure scale of the THz photonic crystals is

from 50um to 500um. Lithography with dry or wet etching is the most popular way to pattern the semiconductor photonic crystals [19, 42]. Fig. 3-1 (a) is an example of deep reactive ion etching in silicon [40]. On the other hand, laser drilling, dicing [81], shown in Fig. 3-1(b), and LIGA [81], shown in Fig. 3-1(c), are other frequently used methods.

a

b

c
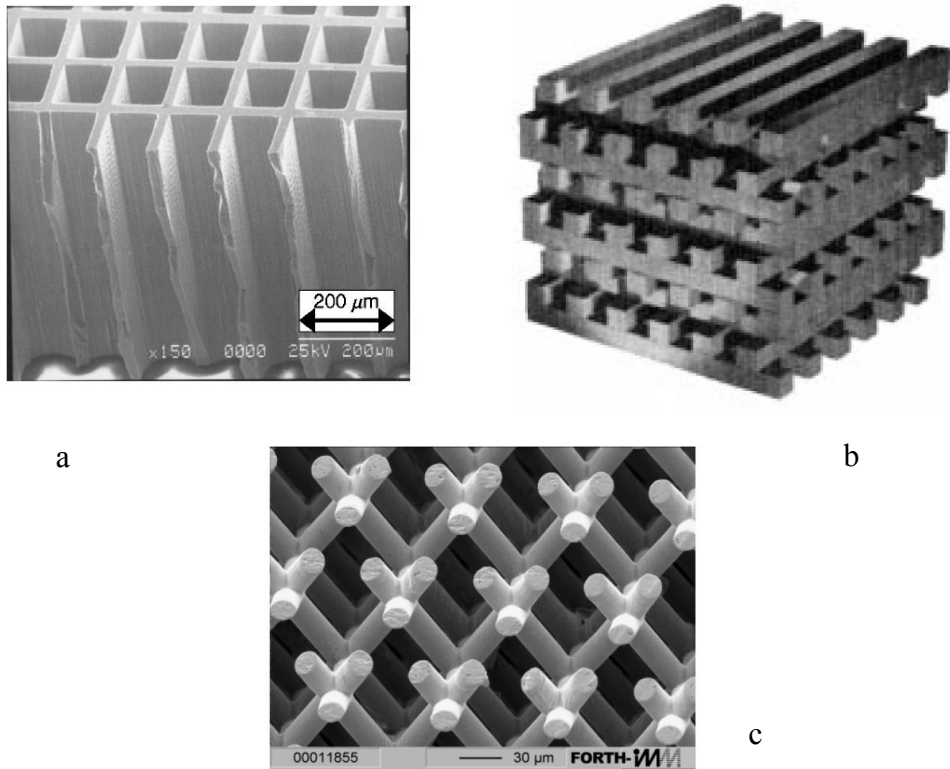
Figure 3-1. Some examples of fabrication for THz photonic crystal structures. (a) 2D photonic crystals by deep reactive ion etching [40], (b) 3D woodpile structures by dicing [81], (c) 'Three-cylinders' model by LIGA [80].

## 3.2 MEMS technology for polymer and metallic photonic crystal

   structures

We employ Micro-Electro-Mechanical-Systems (MEMS) technology [82] to make the high quality THz 2D photonic crystal structures. Uniform photonic crystal structures with very smooth sidewalls are easily formed without undercutting by using the MEMS approach [46].

Polymer photonic crystal structures

Fig. 3-2 shows the four main steps of the fabrication process for polymer (SU-8) photonic crystal structures. First, a 3 inch, 400 μm thick Si wafer without any pattern was coated with a 300 nm Al layer by thermal evaporator. Then, as the key MEMS processing step [82], SU-8 2025 negative photoresist from MicroChem Inc. was spun onto the metal coated surface of the Si wafer with speed of 1000 rpm. This speed forms an unusually thick 70 to 80 μm film. The softbake performed on hotplates with 65°C and 95°C separately. After cooling down, the wafer was placed in contact with the predefined lithographic mask of photonic crystal structures and UV exposed for about 90s. The exposure time depends on the thickness of the SU-8 film and the power of UV source. Then the wafer was baked again with 65°C and 95°C. After a relatively long 15 minute development time, which acts similar to etching, photonic crystal arrays of SU-8 photoresist structures were left standing on the wafer. The development step must follow the SU-8 manual to use SU-8 developer and high grade alcohol to guarantee the structure

quality. A five minute higher temperature bake at 150° C changed the photoresist arrays into arrays of hard polymer standing structures. Finally, the processed Si wafer was diced into oriented 25 mm-wide by 10 mm-long chips to fit over the lower plate of the waveguide. Fig. 3-3 shows a scanning electron microscope (SEM) image of the SU-8 cylinders. Similarly, the SU-8 holes can also be realized by this method (Fig. 3-4). We successfully employed this method in THz parallel plate photonic waveguides [44].
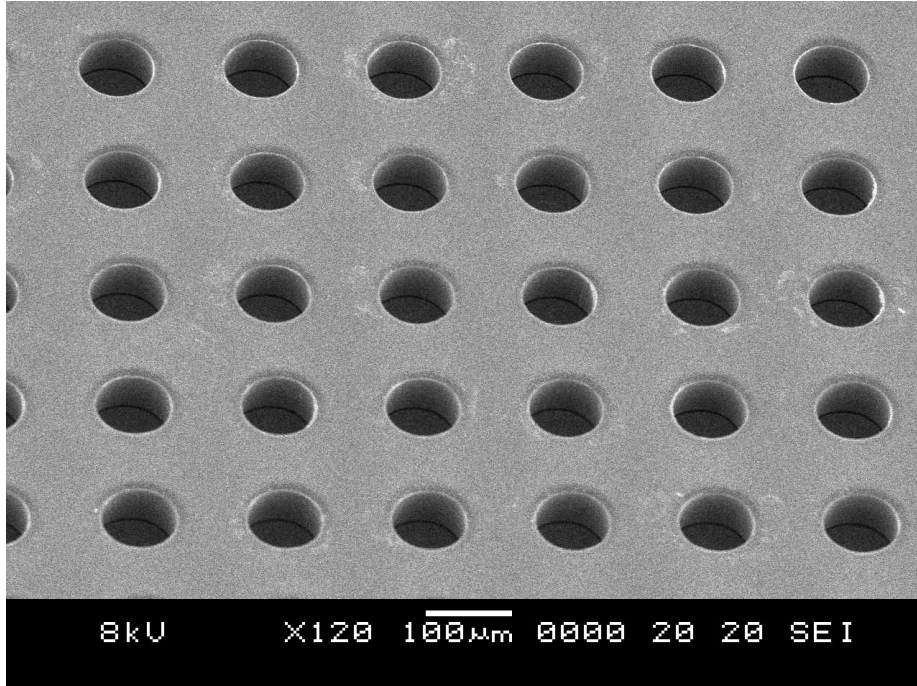
(a)

(b)

(c)

(d)
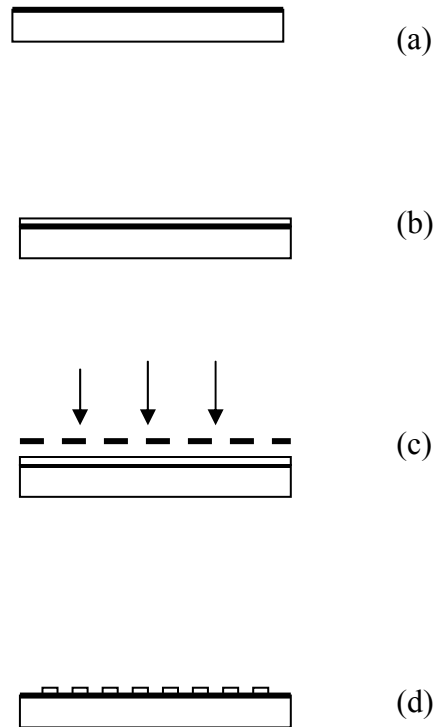
Figure 3-2. Fabrication of SU-8 photonic crystal structures. (a) 300nm Al deposition; (b) SU-8 apply; (c) Expose; (d) Development.
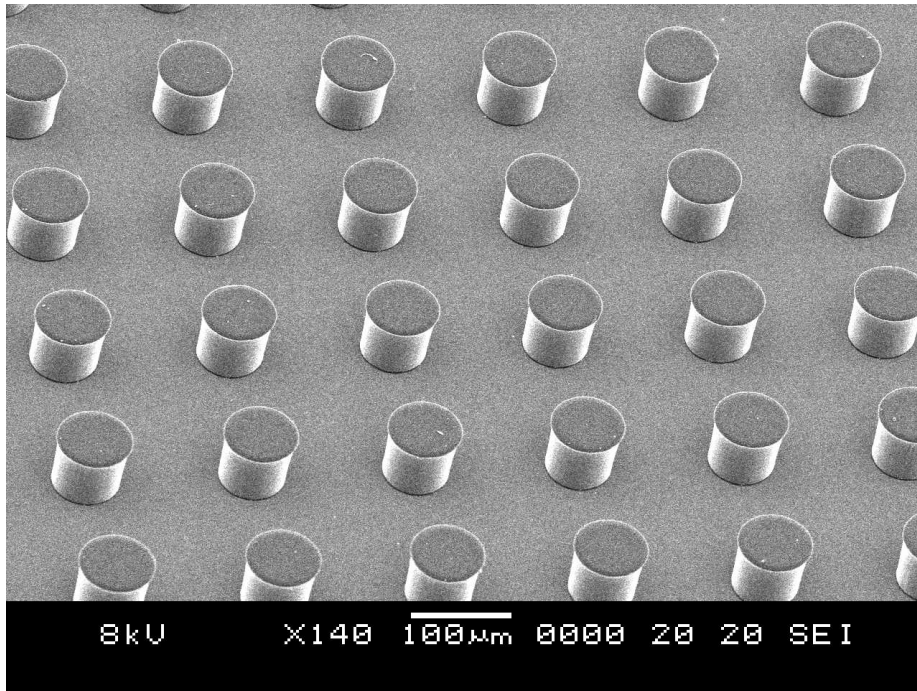
**Figure 3-3.** SEM picture of SU-8 polymer cylinders on 3 inch Si wafer [44].

Figure 3-4. SEM picture of SU-8 polymer holes on 3 inch Si wafer [44].

Metallic photonic crystal structures

The first part of process for metallic photonic crystal structure is the same as the SU-8 photonic crystal structures. After changing to the polymer by the long high temperature baking, a thick layer of metal is coated on the sample surface to transform polymer photonic crystals into metallic photonic crystals. The critical issue for photonic crystal coating is to guarantee the film quality of structures' sidewall. We employed two methods to coat the samples, sputtering and glancing angle deposition.

Sputter deposition is a type of physical vapor deposition (PVD). It is a widely used technique for depositing thin metal layers on semiconductor substrate. And these layers are used as diffusion barrier, primary conductors and so on. The theory of sputtering is well known as to physically remove portions of a coating material (target), and deposit a thin, firmly bonded film onto an adjacent surface (substrate). Sputtering can successful coat a variety of substrates for both conductive and non-conductive materials. The plasma created by sputtering machine not only takes care of the vertical surface of sample, but also the other directions of the sample (Fig. 3-5). Therefore, it has good step coverage. The Cressington 108 Auto sputter coater was employed for the sample coating. The settings for the sputtering are the current of 40mA, the operation pressure of 0.1mBar, and the vacuum pressure of 0.02mBar. The coating rate is about 0.25nm/s. The deposition process is intentionally divided to three periods to avoid overheating the samples.
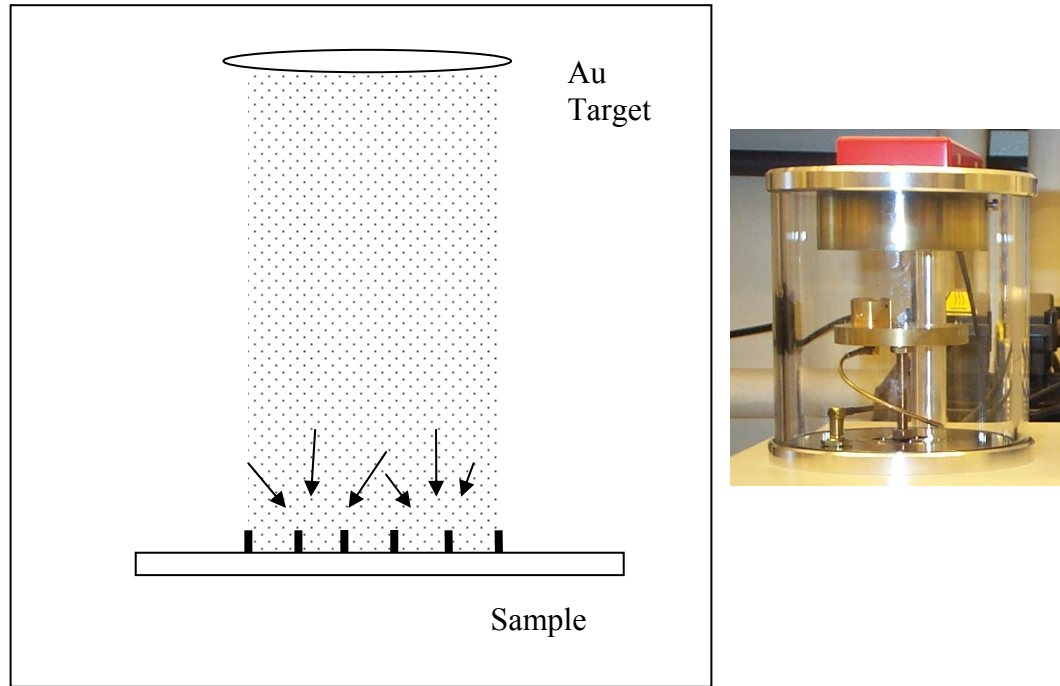
Figure 3-5. Schematic diagram of Sputtering deposition with good step coverage. The photo in the right shows the sputter coater chamber.

The other method we employed is called Glancing Angle Deposition (GLAD), which is a technique by using oblique angle deposition flux and substrate motion for fabricating materials with controlled structure. The method of GLAD is to set an angle between the substrate plane normal and the incident flux, which is called flux angle (θ). This flux angle can be changed manually or automatically by using some transmission devices. For our case, the purpose is to make a smooth film. The sample is tilted and rotated at certain speed in the thermal evaporator, while the step coverage is not good if there is no tilting and rotation. In our case, the surface to be coated only has two directions, vertical and horizontal. So the sample is tilted about 45 degree and rotate (Fig. 3-6). The rotation speed is about 50-60 rpm. The deposition process was conducted under vacuum pressure

lower than 3×10^{-5} Bar. The stable deposition rate of 4nm/s was achieved with the boat heating.
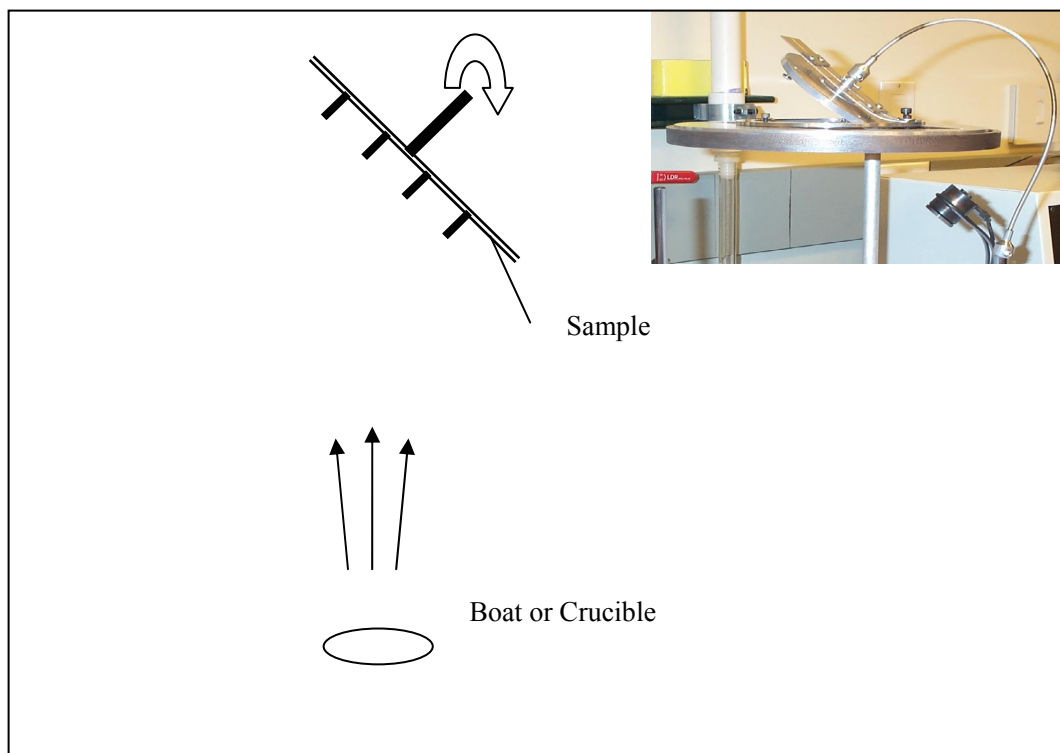
Figure 3-6 Schematic diagram of glancing angle deposition in the thermal evaporator. The insert is the picture of the rotation part, where a flexible arm transfers motor rotation to the sample holder.

3.3 Dicing for semiconductor photonic crystal structures

Micromachining is powerful tool to fabricate the 1D, 2D and 3D photonic crystal structures. It includes dicing, drilling and molding. The dicing machine for semiconductor chip has a resolution better than 1μm, which makes it easy to realize the THz photonic crystal structures. R. Gonzalo et. al. have demonstrated this method to fabricate 3D layer by layer or woodpile photonic crystal structures in submillimeter frequencies [81].
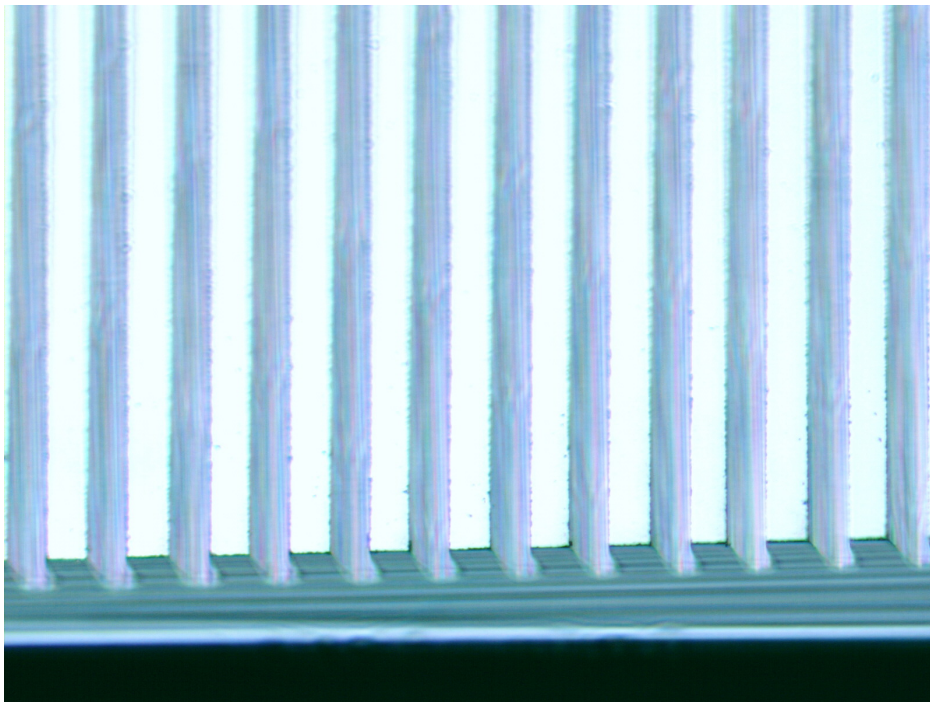
Figure 3-7.   Si 1D photonic crystals by dicing

For our sample, the silicon chip was waxed on an aluminum plate to keep the symmetry of the waveguide holder. The dicing depth needs to adjust carefully to cut through the silicon chip but not the aluminum plate. Fig. 3-7 shows the picture of the 1D

photonic crystal sample. The blades used in dicing machine have different types. There are hubless or hub blade with various thickness. According to the periodicity of the structures, different type of blade should be selected. Usually, the resulted width of cuts is broader than the thickness of the blade because of kerf loss.
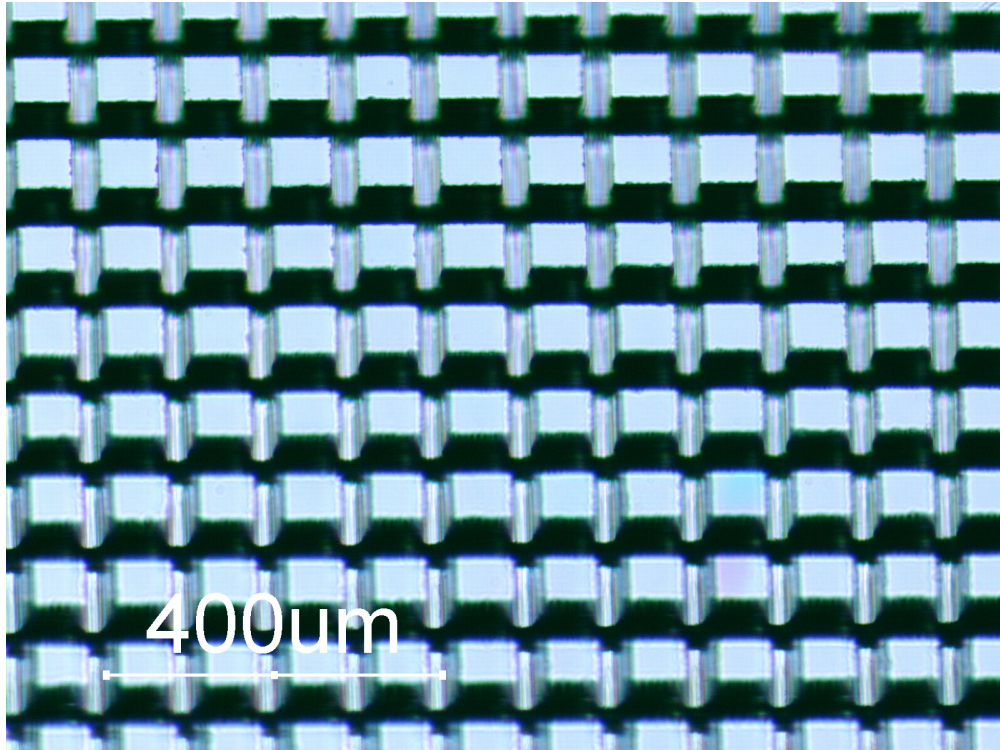
Figure 3-8　Si 2D photonic crystals by dicing

For 2D photonic crystal sample, we cut silicon chip along one direction with fixed separations. Then we cut the same chip along the 90° rotation direction with the same periodicity. The sample diced in that way shows in Fig. 3-8.

3.4　Etching for semiconductor photonic crystal structures

Here, we just briefly mention this method because we don't have high quality deep reaction ion etching machine (DRIE). The reaction ion etching machine (RIE) can etch a thick silicon chip but has severe undercutting. We use SU-8 negative photoresist as the etching mask to protect the unetched parts. For RIE operation, the gas applied in the chamber combined SF_6 and O_2 with 80% and 20% ratio (SF_6 is 12.5sccm and O_2 is 1.5sccm). RF power is at 400W. The base pressure is set to 60mTorr. The etching rate is about 5um/min.
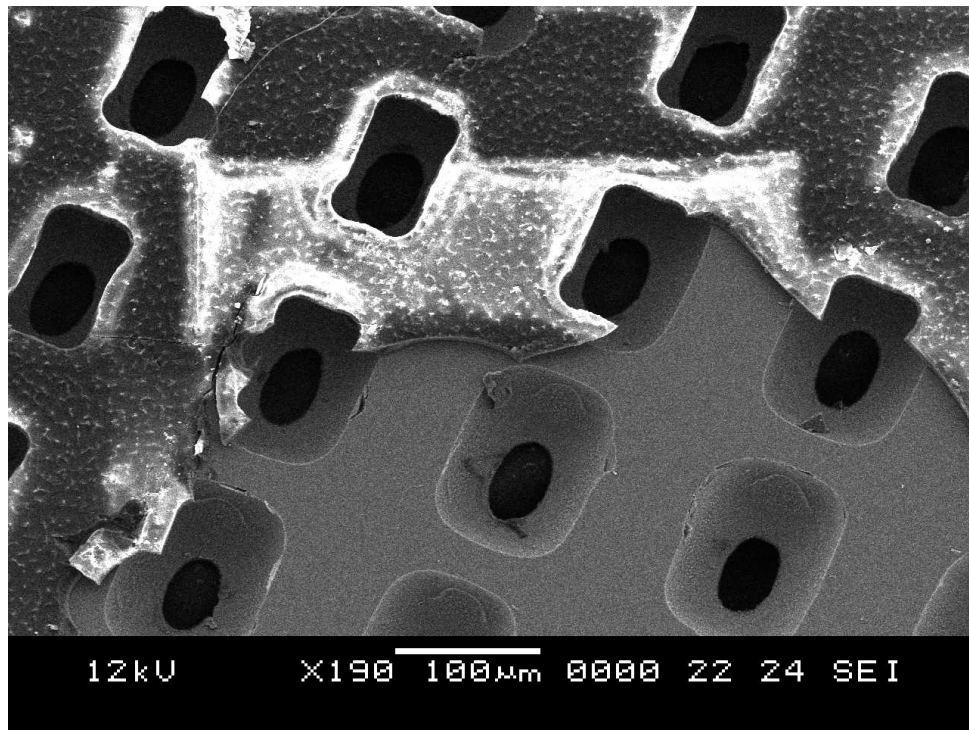
Figure 3-9   Si 2D photonic crystals by etching

In a 50um thick silicon piece, we formed the periodic structure shown on Fig. 3-9. We can clearly see the SU-8 mask and undercutting in the figure. Although the structure is not perfect, this kind of structure can create band gap. However, the simulation may be

a little bit difficult. By this method, some other experiments such as THz surface-plasma polaritons can also be done and extraordinary transmission from this structure was observed [83].

CHAPTER IV

EXPERIMENTAL SETUP

4.1   The samples design

First, the samples are sandwiched between two metal plates. We need to take advantage of the single TEM mode and good coupling properties of parallel plate waveguide. Second, we also need to consider about the delay of reflection from the edge of photonic crystal structures to ensure the complete signal sampling. So the sample design must have enough distance from the silicon lens to the edge of the photonic crystal structures. Fig. 4-1 shows one of the samples. The patterns on the top and bottom are functional as spacers which give enough mechanical support for the sample patterns in the center.

The design of photonic crystal structures depends on three parameters: the dielectric constants of two materials (such as air and polymer in our case); the filling ratio, or the radius and lattice constant ratio; and the lattice pattern of the samples (such as triangular, square). The development of computation technology provides an easy way to simulate the results before fabrication.
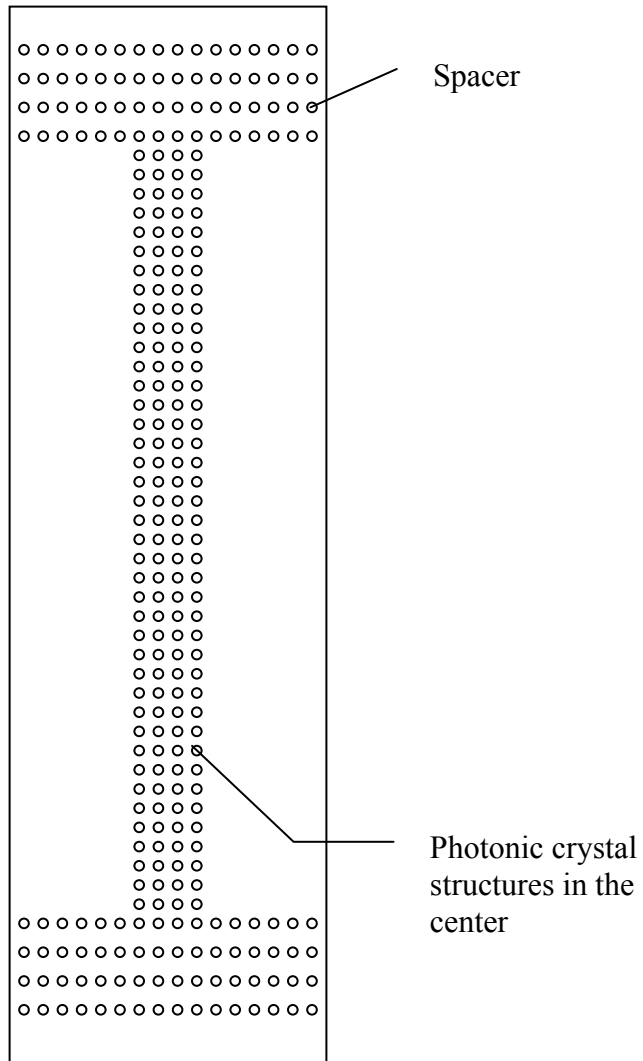
Figure 4-1. Schematic of one sample chip. The dimension of sample chip is 10mm×25mm.
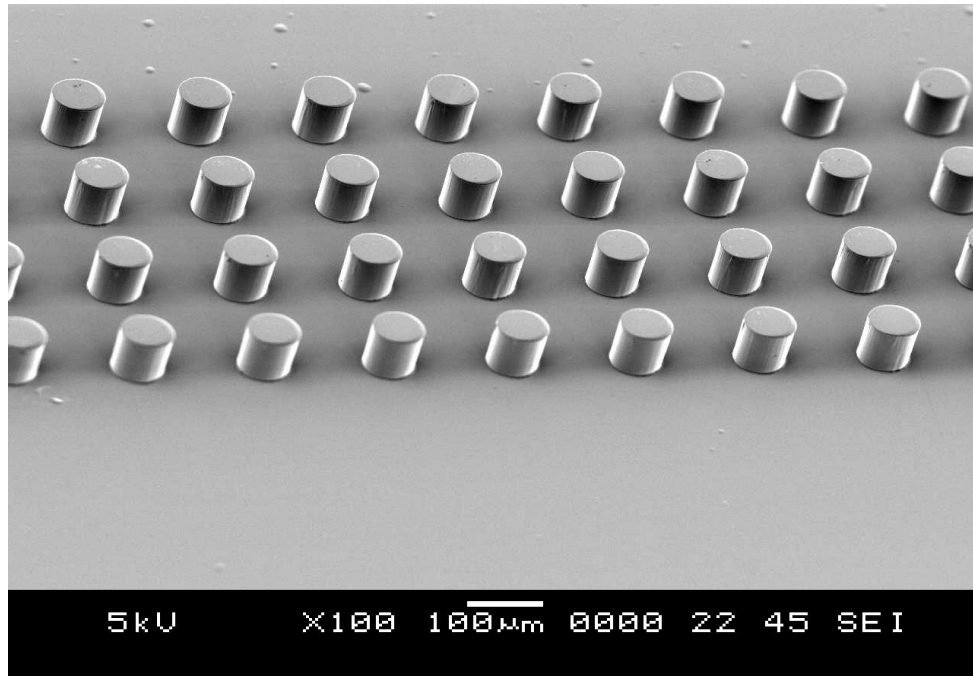
Figure 4-2. SEM picture of part of 4-C chip [46].

Fig. 4-2 shows a SEM picture of 4-C sample. The sample chip is designed as 10mm wide and 25mm long. The width of real photonic crystal structures between two spacers is more than 20mm to ensure the THz beam goes through the photonic crystal pattern instead of spacers. Typical 2D photonic crystal samples consist of a matrix array of m columns with n rows, where m << n and n = (20 mm/160 μm) +1 = 126 for our case. The total number of cylinders is m × n.

4.2   Parallel plate waveguide

Metal parallel plate waveguides (PPWG) [85, 86] consist of two conducting plates (Aluminum) put together forming a thin gap between the plates to guide the propagating THz wave. The air gap between the two plates determines the modes propagated in the

waveguide. The cutoff frequency is defined by $f_c = \frac{mc}{2bn}$, where m is mode number, b is the gap of two plates, and n is the refractive index of material between two plates. With a 70 μm gap, the cutoff frequency of TM_1 is 2.1 THz. But the odd TM_1 mode does not couple into PPWG. The cutoff frequency of TM_2 is 4.2 THz, which means that only the TEM mode existed below 4.2 THz. The concepts and utility of the single TEM mode THz PPWG have been extended to a much larger two-dimensional (2D) plane [84]. TEM-mode propagation is preserved in this larger parallel plate (x,z) structure (Fig. 4-3) with elements of 2D (x,z) shapes, but with no y dependence. Within this plane, 2D reflective, refractive and diffractive quasi-optical components [86] have been demonstrated to behave as their 3D counterparts in free space. For this plane 2D line waves are analogous to 3D plane waves. This situation allows for the precise experimental realization of many situations that are difficult to obtain in free space. Also, most cylindrical type geometry experiments and situations in 3D with linear polarization along the cylindrical axis, which may be infinite, can be realized in this 2D plane with finite thickness or gap.

The 2D photonic crystal structures were completed by placing the top Al metal plate (polished to a mirror-like surface) over and in contact with the tops of the array of standing cylinders. The top and bottom spacer-like structures (70 μm, refer to section 4.1) separated the top Al plate and the regions of unstructured metal surface of the Si plate. As shown in Fig. 4-3, the THz pulse propagation is perpendicular to the columns of cylinders with the polarization parallel to the cylinders, designated as TM, s or E-polarization. The resulting 2D photonic crystal structures centered within the 10 mm-long PPWG's were characterized by the standard THz-TDS system [8].
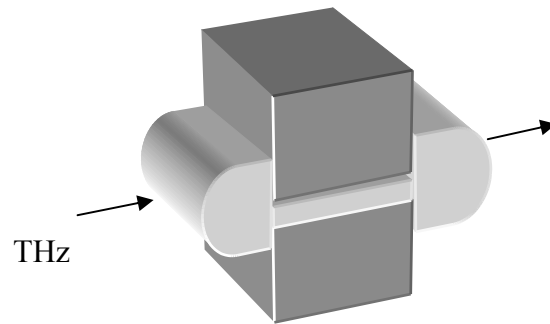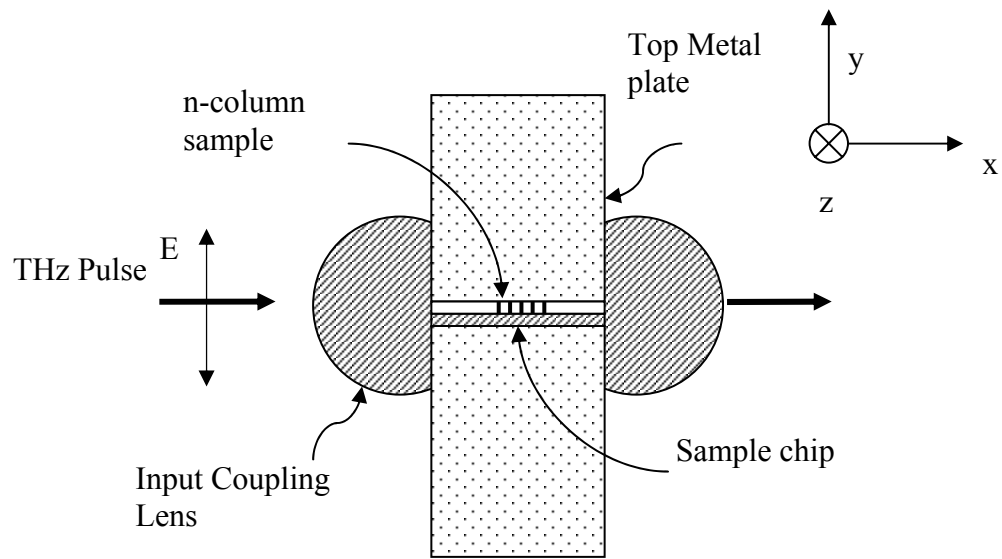
Figure 4-3. The not-to-scale sideview and 3D view of the setup of the sample in the waveguide with the wave coupling by two silicon lenses [77].

4.3   Setup in THz-TDS

The THz optical arrangement converts the incident 3D plane wave from the THz transmitter into an incident 2D line wave matched to the waveguide and couples the waveguide output 2D line wave into an outgoing 3D plane wave which is then efficiently coupled into the THz receiver [85]. Two plano-cylindrical high-resistivity silicon lenses (Figure 4-3) are used to couple the radiation into and out of the reference or sample waveguide, placed at the confocal beam waist of the THz-TDS system (Fig. 4-4). The lenses are 15 mm x 10 mm x 6.56 mm with a 5 mm radius of curvature. The input lens focuses the incoming THz radiation to an elliptical spot with a frequency independent minor axis of 150 μm, perpendicular to the waveguide plates, and a linearly wavelength-dependent major axis parallel to the plates with a 1/e amplitude diameter $d = 9$ mm at 1 THz. Within the PPWG this situation gives a frequency independent 2D THz beam divergence $\theta \cong \lambda/d = 0.3/9 = 0.033$ rad, which is also the angular acceptance of the THz receiver. This narrow acceptance angle of the THz receiver is important for our measurements, because the forward (zero order) transmission through the photonic crystal structures is expected to be sharply angular dependent, which is similar to a transmission grating, requiring good angular resolution to obtain the proper on-axis signal strength.

The pump and probe laser pulse beams are created by a KLM Ti:Sapphire laser which is pumped by a Spectral Physics Millennia cw laser. The laser beam has 40fs pulse train with a nominal wavelength of 820nm and a repetition rate of 100MHz. The average powers of pump and probe laser beam are adjusted to about 10mW. The transmitter is biased with 70V DC and the receiver has a very highly sensitive current amplifier. A

mechanical chopper is placed between the transmitter and the paraboloidal mirror for the lock-in amplifier, which connects to current amplifier, to get the received signal. The computer controls the delay of probe beam by stepper moving reflector, and reads the output signal from the lock-in amplifier. The special LabView program fulfills this job perfectly.
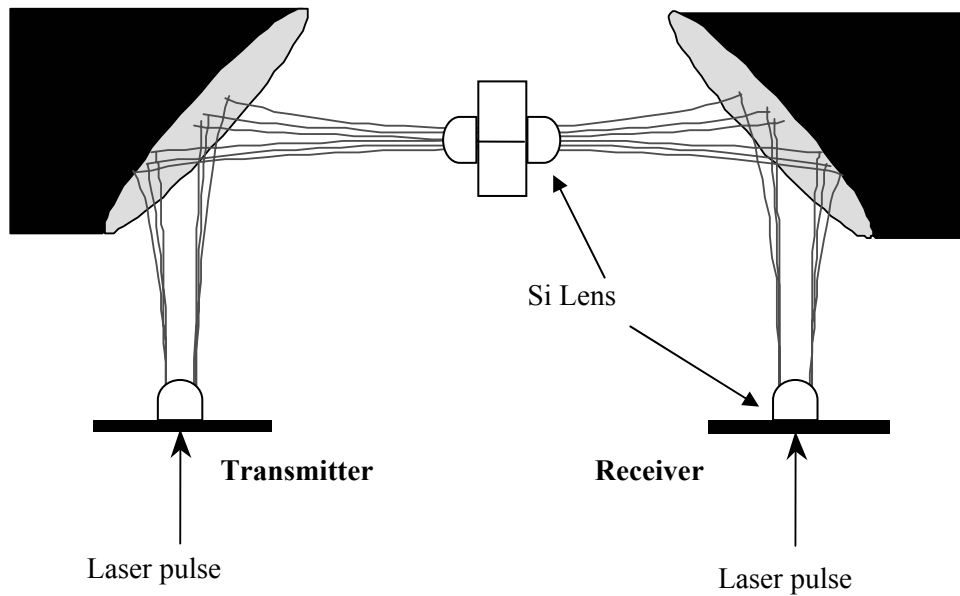
Figure 4-4. Whole THz-TDS setup with sample setup in the center of THz path.

CHAPTER V

STUDY OF BASIC THz PHOTONIC CRYSTALS

5.1   Polymer (SU-8) photonic crystal structures

Dielectric photonic crystals are the major subjects for science research in meta-
materials [3]. The first investigation of THz photonic crystals was based on dielectric
materials [19]. In order to understand the behavior of photonic crystals in PPWG, it is
necessary to conduct the dielectric (polymer) research on this setup [46]. The 2D polymer
sample fabrication followed the method of section 3.2. The photonic crystal structures
consist of a square array of cylinders in air with lattice constants of 160μm, diameters of
65μm and heights of 70μm. Four samples with zero-column (blank), 4-column (4-C), 8-
column (8-C) and 60 column (60-C) arrays of cylinders were separately fabricated for the
polymer (SU-8) photonic crystal experiment.

Fig. 5-1 shows the transmitted THz reference pulse together with three different
sample pulses, which have propagated through the 4-C, 8-C, or 60-C, 2D photonic crystal
structures, respectively. The baselines of the three sample pulses in Fig. 5-1(a) have been
offset for clarity. The THz reference pulse was transmitted without distortion through the
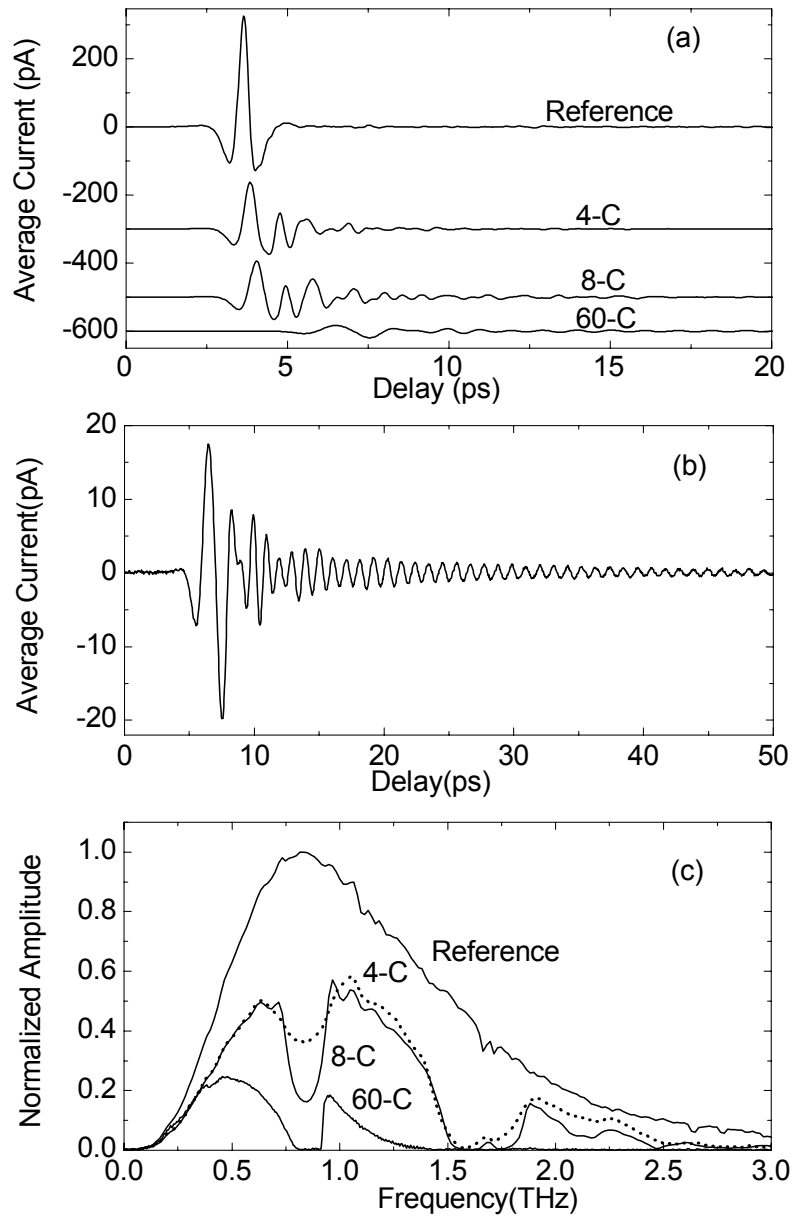
Figure 5-1. The measurement results of SU-8 photonic crystals [46]. (a). Measured reference, 4-C, 8-C and 60-C transmitted THz pulses, respectively. (b). Expanded view of 60-C transmitted pulse. (c) Corresponding amplitude spectra for reference, 4-C, 8-C, and 60-C pulses.

25 mm wide by 10 mm long PPWG with 70 μm plate separation and no photonic crystal structure in place (blank sample). Compared to the reference pulse, the sample pulses were attenuated, reshaped, and developed a low-level ringing structure extending to approximately 20 ps for the 4-C and 8-C pulses, and to 100 ps for the 60-C pulse. In addition, the leading edges of the sample pulses show slight propagation delays with respect to the reference pulse, which propagates at the free-space speed of light c. These delays of 0.2 ps for 4-C, 0.4 ps for 8-C and 2.9 ps for 60-C structures are in approximate agreement with those calculated from a simple filling factor argument. The filling factor F is given by the ratio of the cross-sectional area of a cylinder to the lattice spacing area.

$$F = \pi \times (65 \mu m / 2)^2 / (160 \mu m)^2 = 0.130 \qquad (38)$$

The calculated delay D is then given by

$$D = N \times (160 \mu m) \times F \times (n-1) / c \qquad (39)$$

Where N is the number of columns, $n = 1.7$ is the refractive index of the SU-8 cylinders, and c is the speed of light. The calculated values from the above equation are D = 0.19, 0.39 and 2.91 ps for $N = 4$, 8 and 60, respectively.

Fig. 5-1(b) shows more detail of the 60-C pulse. It presents the complex reshaped waveform with a ringing monotonic decay, measured with a signal-to-noise ratio (SNR) of approximately 300. Fig. 5-1(c) shows the corresponding amplitude spectra of the reference pulse and the three sample pulses, demonstrating the filtering capability of the 4-C, 8-C and 60-C structures. Well resolved spectral features are observed, which increase in strength from the 4-C compared to the 8-C compared to the 60-C structure. The amplitudes of the spectral peaks have been reduced by the dielectric absorption of

the cylinders. In order to have the highest frequency resolution, the 60-C spectrum is the transform of the complete 60-C pulse extending to 100 ps.

Fig. 5-2 (a) shows the amplitude transmission for all three samples. Here, the arising of the band gap feature strength with the number of columns is clearly demonstrated. The 60-C spectrum shows a well-defined band gap from 0.81 to 0.91 THz with a very sharp (0.01 THz) turn-on at 0.91 THz. The 8-C transmission shows the same band gap in a developing stage and another developing band gap at a higher frequency range from 1.5 to 1.84 THz, which contains a small relatively sharp transmission peak at 1.70 THz. One discrepancy is that the measured transmission from low frequencies to the edge of the first band gap at 0.8 THz is significantly lower than theoretical predictions for a plane wave propagating through a similar 3D array of endless columns of infinitely long cylinders. A possible reason for this reduction is that the finite extent of our 2D beam reduces the on axis (zero-order) transmission by broadening the angular divergence. Fig. 5-2 (b) presents the relative phase of the sample pulses with respect to the reference pulse. The dashed lines associated with each sample pulse are the phase shifts Φ determined by the filling factor time delay.

$$\Phi = 2\pi N \times (160\,\mu m\,/\,\lambda) \times F \times (n-1) \qquad (40)$$

The observable features deviating from the dashed lines describe the phase response associated with 2D band gap features in the transmission of Fig. 5-2(a). The large absorption of the 60-C sample truncated the phase determination below 1 THz.
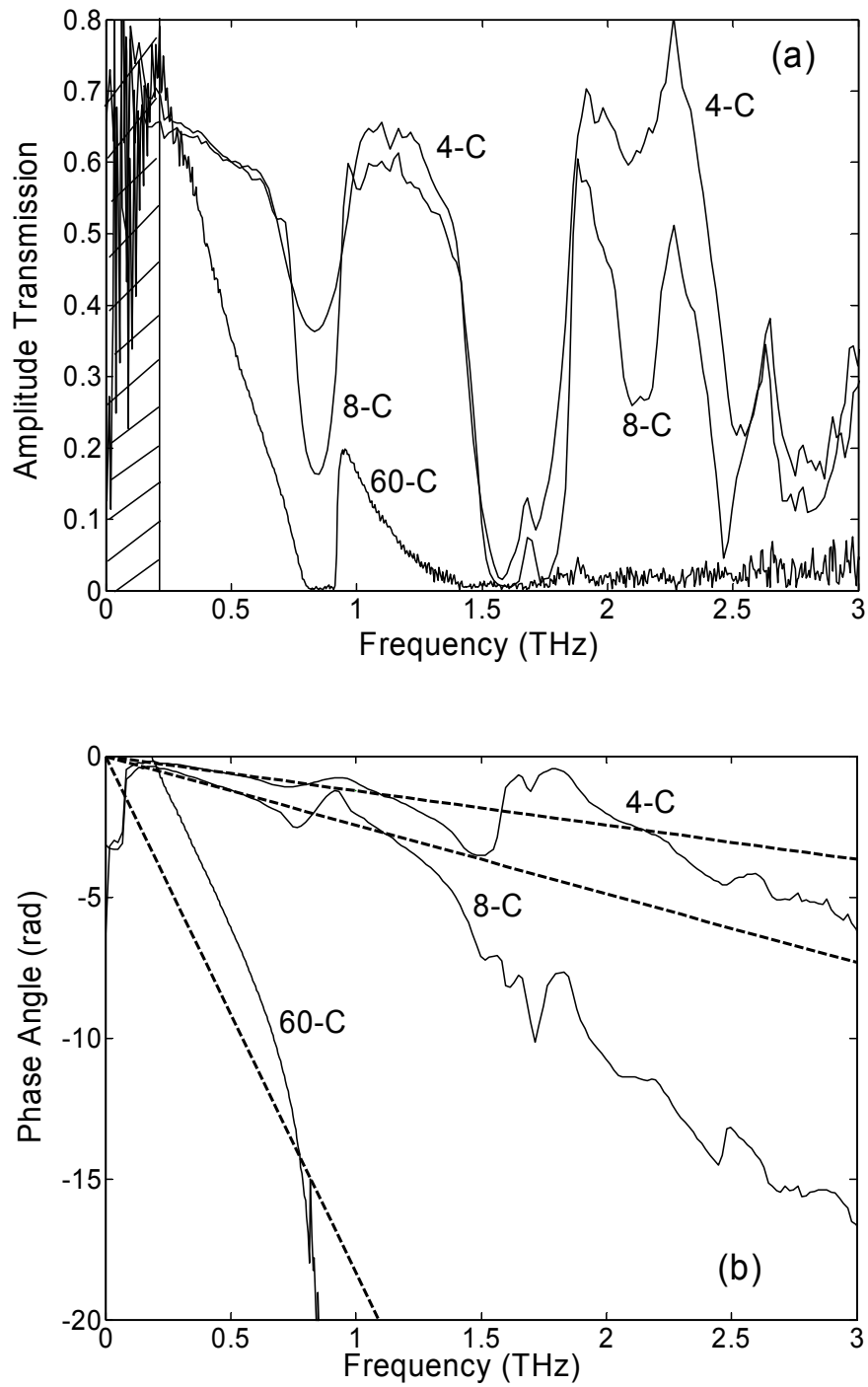
Figure 5-2. (a). Amplitude transmission of the 4-C, 8-C and 60-C samples, respectively. (b). Calculated phase shift (dashed curves) and measured relative phase shift (solid curves) for 4-C, 8-C, and 60-C pulses [46].

48
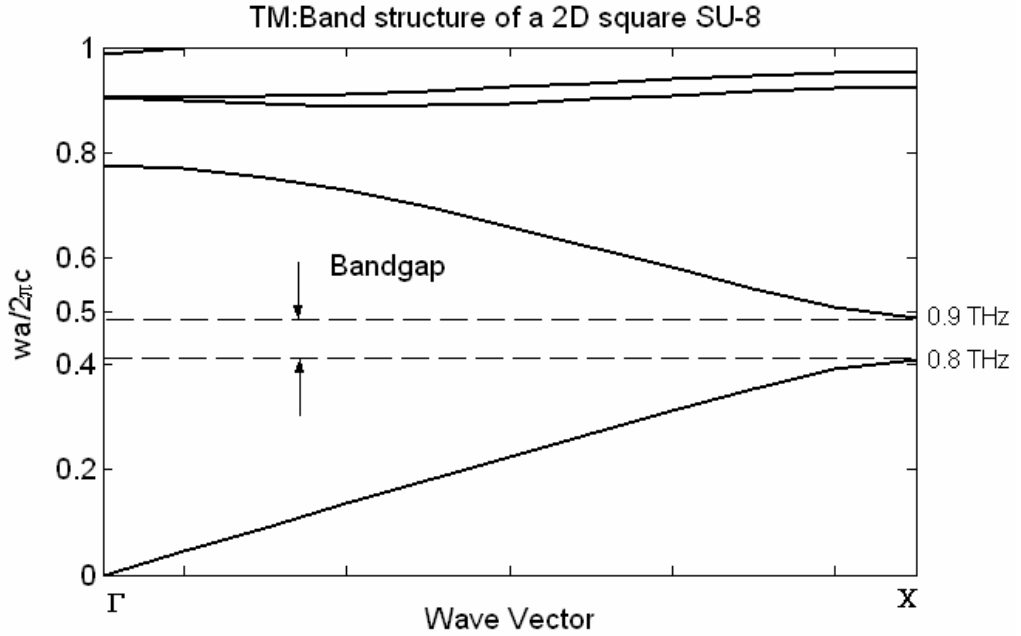
Figure 5-3. Band structure of 2-D square polymer photonic crystals with a=160μm, d=70μm and infinite height.

Figure 5-3 is the band structure calculated by PWE method. The wave vectors from Γ to X represent that the incident direction is same as the experimental case (10). Bandgap shown in dashed lines is from 0.8 to 0.9 THz which corresponds to the measurement result. From 1.5 to 1.8 THz in the band structure, it is clear that there is a narrow state at around 1.7 THz, which shows a peak in the Fig. 5-2(a). Although PWE method precisely indicate the bandgap positions, it is hard to observe how much power transmitted from the structures, because PWE does not consider the loss of the signal in the materials.
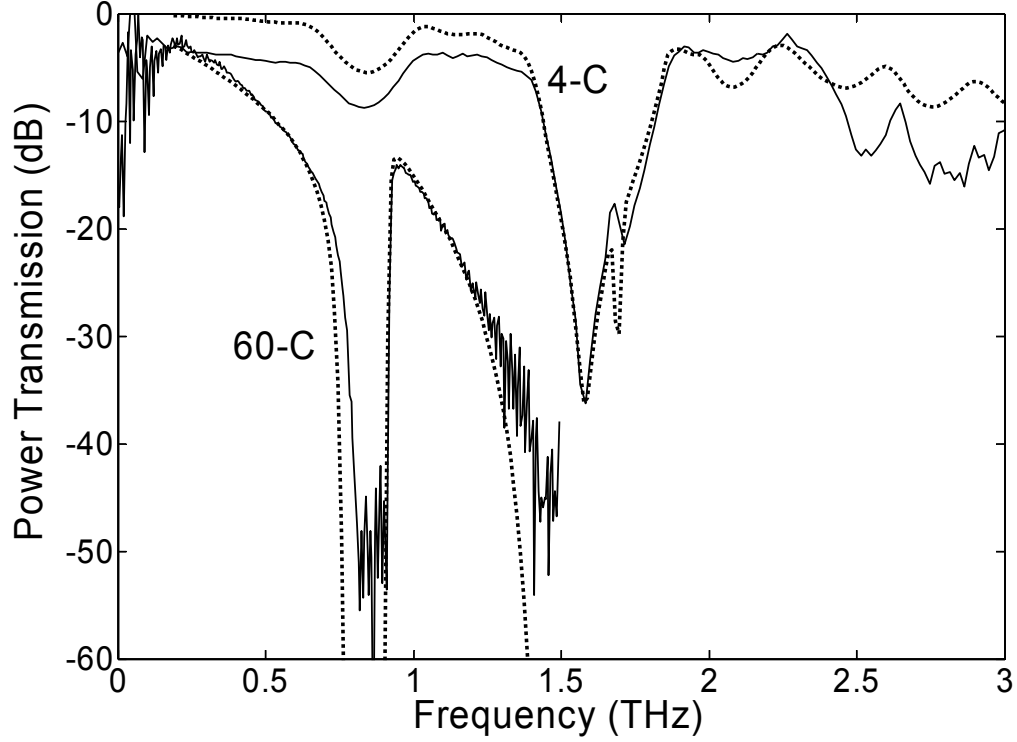
Figure 5-4. Measured power transmission for the 4-C and 60-C samples (solid curves) compared with theory (dotted curves).

Fig. 5-4 shows the power transmission measurements $T(\omega)$ in dB of the 4-C and 60-C structures. The $T(\omega)$ calculated by

$$T(\omega) = 20 \log \left| \frac{S(\omega)}{R(\omega)} \right| \qquad (41)$$

Where $S(\omega)$ is the sample amplitude spectrum and $R(\omega)$ is the reference spectrum.

Here, we compare our experimental results with numerical TMM calculations [65]. For our case the ratio of cylinder radius to the square lattice constant is (32.5 μm)/(160 μm) = 0.203; based on our THz-TDS measurements of cured SU-8 2025 photoresist and previous THz-TDS measurements [87], the real part of the frequency-dependent index of

refraction is approximated by the constant value $n_r = 1.7$; the frequency dependent absorption $\alpha = 4\pi n_i /\lambda$ is approximated by the constant complex index of refraction $n_i = 0.044$, giving the complex dielectric constant $\varepsilon = 2.88 + i0.15$, used in the calculation. The resulting comparison with theory gives excellent agreement with the location and depths of the transmission minima for the 4-C sample out to 2 THz; from 2 to 3 THz theory shows a simple oscillation in approximate synchronization with experiment, but not in agreement with magnitude. Theory is in good agreement with the 60-C sample, except for too much attenuation on the low frequency edge of the band gap at 0.8 THz. Excellent agreement is obtained for the fast turn-on at 0.91 THz, including the peak height of the transmission. The comparison stops at 1.5 THz, beyond which the transmission is lost in the noise.

The TMM calculation is based on the infinite cylinders, while the real samples have finite thickness, which is called as photonic crystal slab. The theory shows there are some effects for photonic crystal slab because of the loss in vertical direction [62]. The results shown by other groups also proved the shift or band gap changing between the finite photonic crystal slab and infinite photonic crystal calculation. The photonic crystal slab in air background has been investigated intensive [62]. The total internal reflection happens between high refractive index of photonic crystal materials and low refractive index of air. This index guiding changes the shape and position of band gaps and introduces the concept of light cone. In our case, the setup should be called photonic crystal slab by metallic cladding (metallic waveguide) [88]. However, the third dimension on the vertical direction in a waveguide introduces new phenomena that do not occur in an ideal infinite 2D photonic crystal structures. The most significant

confinement effect is the mixing of modes with different polarizations, TE or TM polarized in 2D structures. The mixing modifies the band structure, causing anticrossings where modes of opposite polarization intersect. The mixing can also lead to polarization conversion if symmetry allows. This kind of polarization conversion was observed in waveguide propagation measurements [89].

The advantage of our experimental setup is that there is only a single TEM mode existing in the waveguide. The mixing of TE and TM polarization does not happen. The way of using 2D structures to simulate 3D structures with infinite thickness are realized and proved by our setup and experiment. In the experiments, the single mode is conserved below 4 THz as calculated in section 4.2. The simulation result matches the experimental result well without shift and band changing. However, we can see a little band changing in 60-C sample, which may be contributed by the frequency dependent index and absorption, as well as the reflection at the edge of the 60-C sample.

5.2   Metallic photonic crystal structures

Metallic photonic crystals (MPCs) have shown unique characteristics over the dielectric photonic crystals, such as wider bandgap, lighter weight, smaller size [4]. The method to fabricate high quality pure metallic photonic crystals needs precise mechanical machines. Instead of that, the metal coating method is easier to design and fabricate. The metal coating photonic crystal structures also show the same properties as the pure metallic photonic crystals.

Two samples are tested in the THz-TDS system using parallel plate waveguide to guide THz in and out from the photonic crystal structures. These two samples, with Al and Au coating, have the same structures consisting of 4 columns cylinders. The periodicity is 160μm, the diameter of the cylinders is 70μm and the height of the cylinders is 70μm. The experiment process is the same as that in the section 5.1.

Fig. 5-5 shows the reference pulse and spectrum. Fig. 5-6 shows 4-C Al sample and 4-C Au sample pulses and spectra. The pulses from the samples have ringing structure extended to 30 ps. The propagation delay of both sample pulses is about 0.2 ps with respect to the reference pulse. From the spectra, it is clear that the bandgaps are from low frequency around 0 to 1.1 THz and from 1.2 to 1.65 THz. We noticed that the positions of bandgaps are almost same, because Au and Al samples have similar dimensions. The amplitude of Au is a little higher than that of Al samples due to the difference of conductivity, which relates to the loss on metal surface.
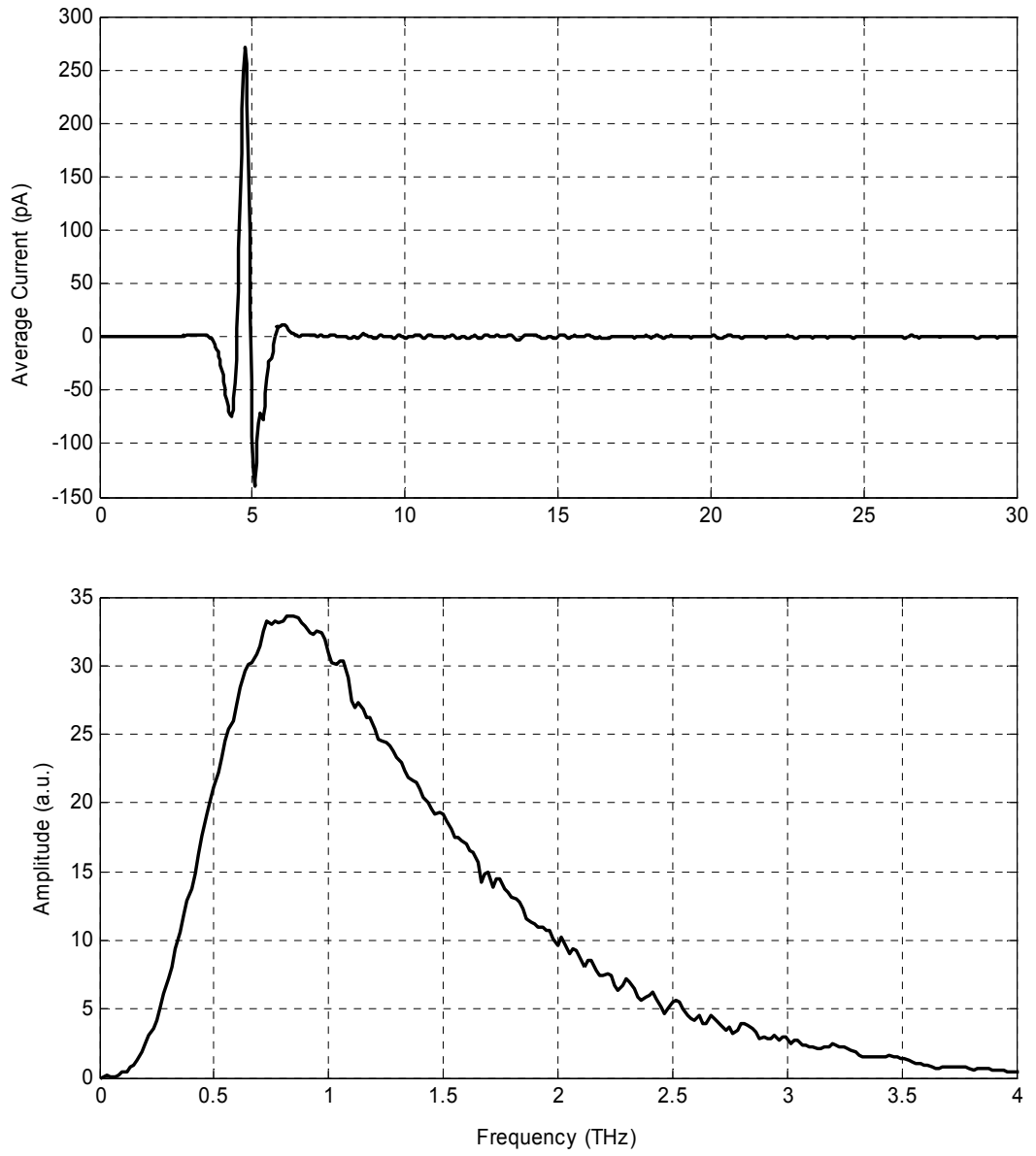
Figure 5-5. Transmitted THz pulse through the reference sample and the corresponding amplitude spectrum.
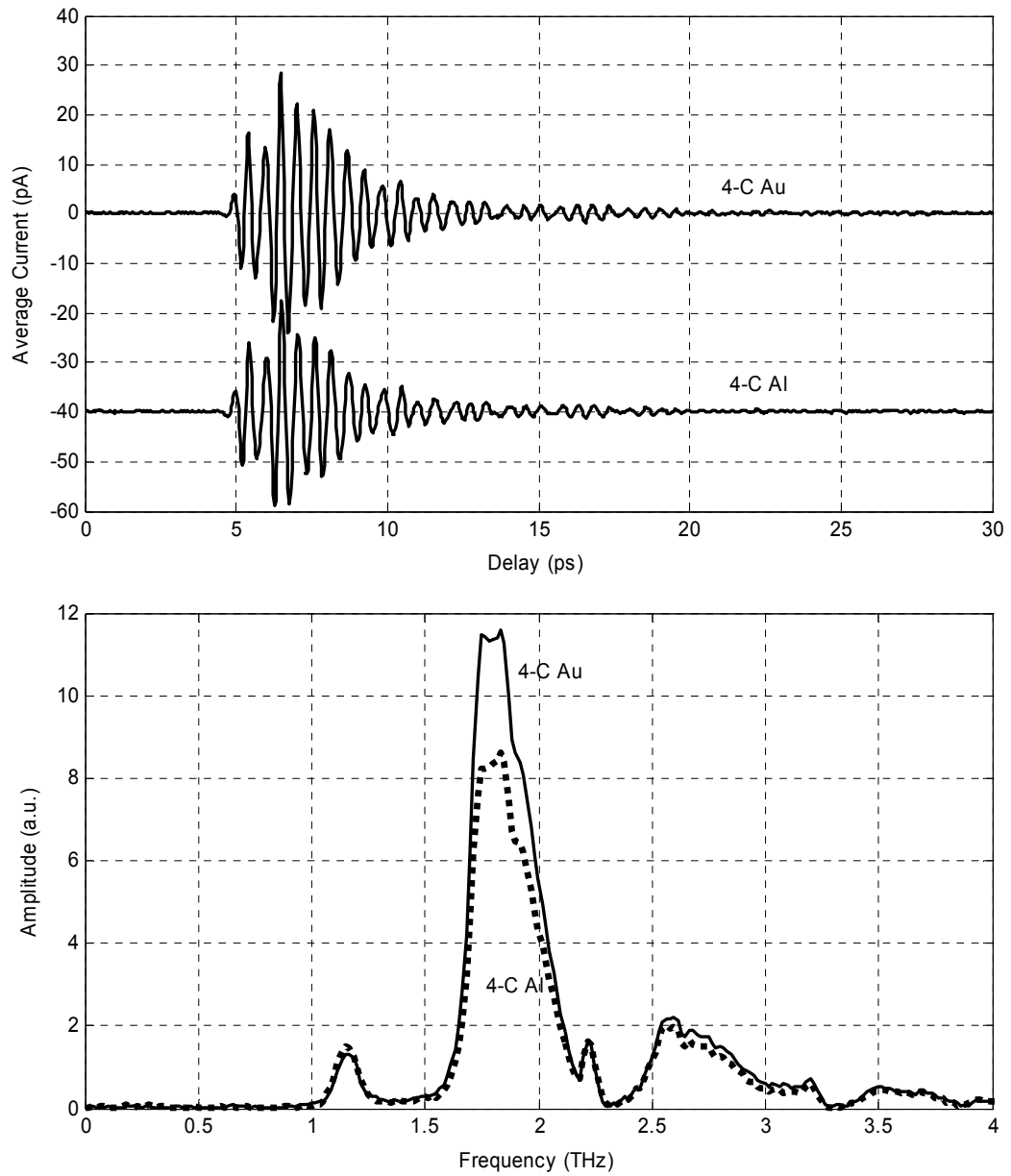
Figure 5-6. Measured 4-C Al (dotted curve), 4-C Au (solid curve) transmitted THz pulses and spectra, respectively.
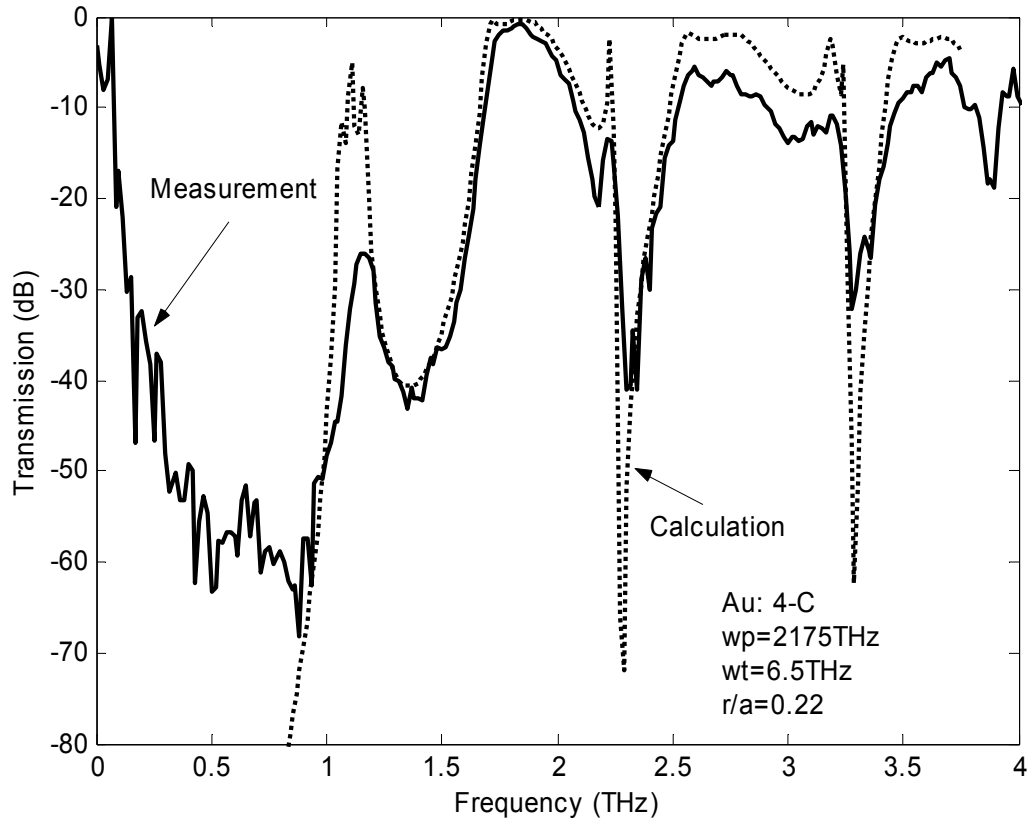
Figure 5-7. Measured power transmission for the 4-C Au sample (solid curve) compared with theory (dotted curve).

At THz frequencies, within the approximations of the simple Drude model, the real part of the dielectric constant of metal is a negative constant, while the much larger imaginary part is to a good first order approximation proportional to the wavelength [9]. This information is needed for the theoretical modeling. The simple Drude model [90] treats the free carriers in a metal as classical point charges subject to random collisions, for which the collision damping is independent of the carrier velocity. According to the model, the frequency-dependent complex dielectric constant ε_c (the square of the complex index of refraction $n_c = n + in_i$) is given in SI units as

$$\varepsilon_c = \varepsilon_\infty + i\sigma/(\varepsilon_0\omega) = \varepsilon_\infty - \omega_p^2/\omega(\omega + i\omega_\tau) \qquad (42)$$

where the corresponding Drude complex conductivity is given by

$$\sigma = \sigma_{dc}i\omega_\tau/(\omega + i\omega_\tau) = i\varepsilon_0\omega_p^2/(\omega + i\omega_\tau) \qquad (43)$$

For the above relationships, ε_∞ is the contribution of the bound electrons, $\omega_\tau = 1/\tau$ is the damping rate, and τ is the average collision time. The plasma angular frequency ω_p is defined by $\omega_p^2 = Ne^2/(\varepsilon_0 m)$, where N is the number density of carriers, e is the electronic charge, ε_0 is the free-space permittivity, and m is the effective carrier mass. The dc conductivity σ_{dc} is given by $\sigma_{dc} = e\mu N$ with the mobility $\mu = e/(m\omega_\tau)$. The above expression for ε_c can be rewritten in the form

$$\varepsilon_c = \varepsilon_\infty - \frac{\sigma_{dc}\omega_\tau}{\varepsilon_0\omega(\omega + i\omega_\tau)} = \varepsilon_\infty + \frac{i\sigma_{dc}}{\varepsilon_0\omega(1 - i\omega/\omega_\tau)} \qquad (44)$$

For the microwave and THz frequency ranges the ratio $\omega/\omega_\tau \ll 1$, and the above expression for ε is, to a good first order approximation, given by

$$\varepsilon_c \approx \varepsilon_\infty - \sigma_{dc}/(\varepsilon_0\omega_\tau) + i\sigma_{dc}/(\varepsilon_0\omega) \qquad (45)$$

For the case of conducting metals ε can, to an excellent approximation, be further reduced to

$$\varepsilon_c \approx -\sigma_{dc}/(\varepsilon_0\omega_\tau) + i\sigma_{dc}/(\varepsilon_0\omega) \qquad (46)$$

In order to perform our numerical simulation, using the transfer matrix method (TMM) [55, 65], we need two input parameters, the plasma frequency ω_p and the damping rate ω_τ. These parameters are related to σ_{dc} by

$$\sigma_{dc}\omega_\tau = \varepsilon_0\omega_p^2 \qquad (47)$$

Given the measurement of $\omega_\tau/2\pi = 6.5$ THz for gold [79], and given the handbook Au

conductivity of $\sigma_{dc} = 4.10 \times 10^7/(\Omega \cdot m)$ [91], ω_p as calculated by the relationship $\omega_p = (\sigma_{dc}\omega_\tau/\varepsilon_0)^{1/2}$, is equal to $\omega_p / 2\pi = 2,175$ THz. For Al, $\omega_p = 3570$ THz, $\omega_\tau = 19.4$ THz.

Fig. 5-7 compares the experimental power transmission of the 4-C Au coating sample and the calculated power transmission of the 4-C pure Au sample. The results fit very well beyond 0.8 THz. Below 0.8 THz, there are some difference between the experimental result and the calculated result because of the finite thickness of metal film. The wave can penetrate the thin film when the skin depth is greater than the thickness of the thin metal film, where the skin depth is inversely proportional to the square root of frequency. If we take -30dB as the threshold, the band gaps are from 0.15 to 1.1 THz and 1.22 to 1.57 THz for experimental result. And the band gaps are from 0 to 1.03 THz and 1.22 to 1.55 THz for calculated result. The positions of the dips and peaks of measurement results are identical with the calculated results. The amplitude deference is believed to be caused by the alignment, fabrication and the loss of the samples.

Fig. 5-8 compares the experimental power transmission of the 4-C Al coating sample and the calculated power transmission of the 4-C pure Al sample. The results fit well beyond 0.85 THz. Below 0.85 THz, there are some difference between the experimental result and the calculated result for the same reason as the Au sample. We still take -30dB as the threshold. The first two band gaps are from 0.31 to 1.09 THz and from 1.34 to 1.6 THz for experimental result. And the first two band gaps are from 0 to 1.06 THz and from 1.23 to 1.59 THz for the calculated result.
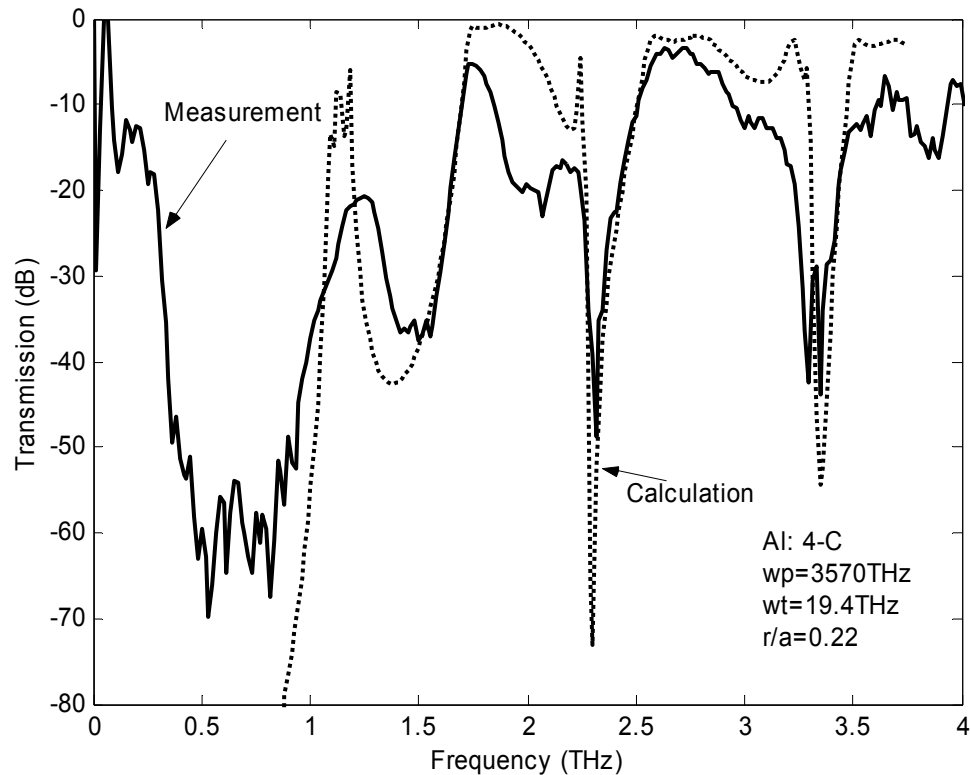
Figure 5-8. Measured power transmission for the 4-C Al sample (solid curve) compared with theory (dotted curve).

Additionally, the TMM simulation change with different incident angle for 4-C Au sample is shown in Fig. 5-9. The wide bandgap from 0 to 1.2 THz is angle-independent. This angle independent property is very important for real photonic devices because many devices require whole bandgap to guarantee there is no leak from any direction of propagation. The typical devices such as photonic waveguide, photonic network and photonic fiber are based on this property. And the wide bandgap of metallic photonic crystals also benefit the wide band wave propagation.

The metallic photonic crystal experiment proves again that the 2D ideal photonic crystal can be simulated by the 2D photonic crystal slab in single mode PPWG. The well fitted band gaps, deeps and peaks are shown in figures, especially in 4-C Au samples.
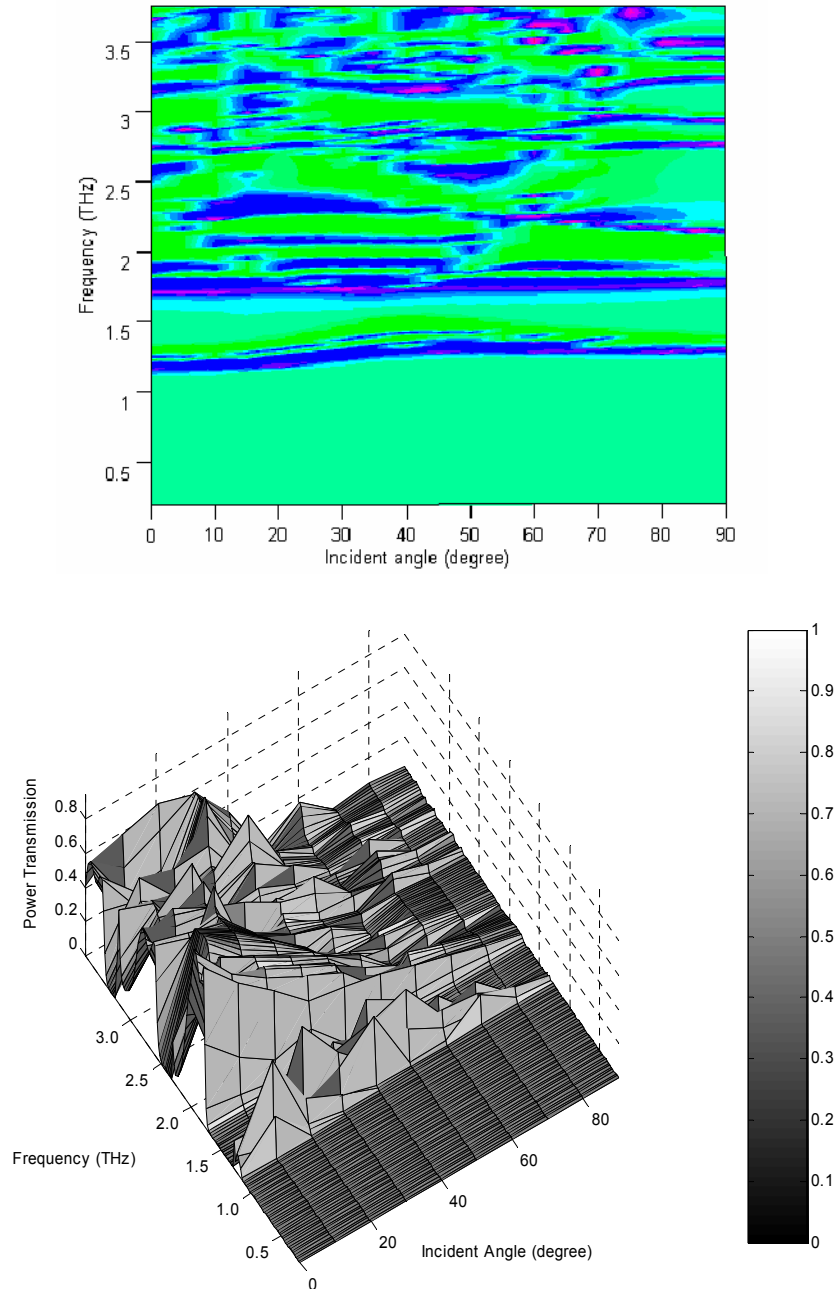
Figure 5-9. 2D and 3D Band diagram of 4-C Au sample with changing incident angle

5.3 Metallic photonic crystals with point defects and Fabry-Perot defect

The metallic photonic crystals with defects [9] consist of a square array of 126 rows of cylinders in air with lattice constant L = 160 μm, diameter d = 70 μm and height h = 80 μm. The structures were first fabricated by SU-8, and then coated with 150 nm Au by the sputter coater. Three different samples with 5-column (5-C) arrays of cylinders were fabricated. As shown in Fig. 5-10(a), Sample A has 5-C cylinders without any defects, Sample B has 5-C cylinders with the removal of one cylinder every 5 rows from the center column, and Sample C has 5-C cylinders with the removal of the center column to form the F-P defect (Fabry-Perot cavity). Fig. 5-10(b) shows the SEM image of Sample B. The structures on the two sides of the chips were used as the spacers, which have the same height as the cylinders in the center (Fig. 5-10(a)). The reference chip has the same spacer structures, but no cylinders in the center.

Fig. 5-11 shows the transmitted TEM-mode THz pulse through the Reference Sample and the corresponding amplitude spectrum, which are similar to the THz pulse and spectrum in free space. The reference pulse is only shown to 10 ps to detail the pulse shape; the complete scan extended to 30 ps. The incoming THz beam, focused by the cylindrical Si lens, has been shown single TEM(TM$_0$) mode coupling in the PPWG with plate separation less than 150 μm [84-86].

Sample A   Sample B   Sample C

(a)

THz

(b)
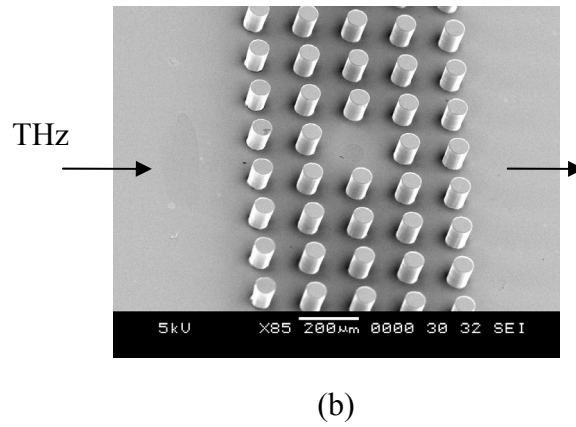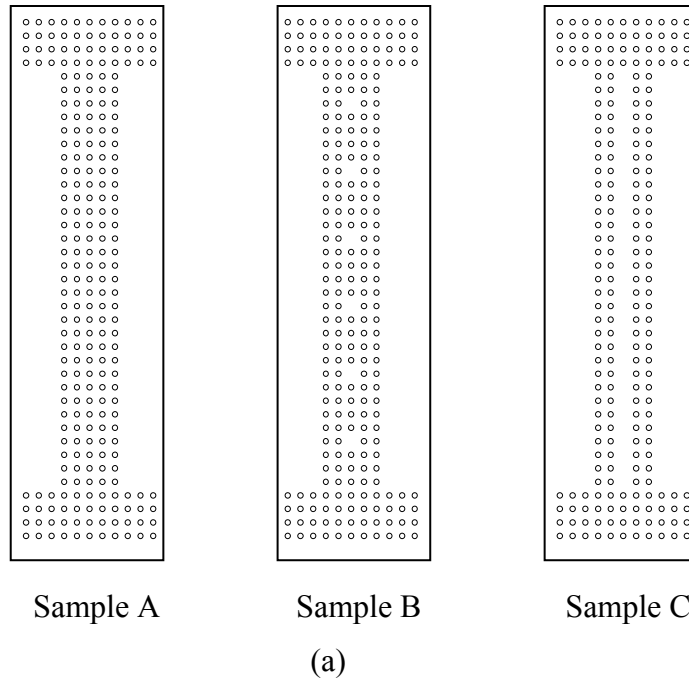
Figure 5-10. (a) The not-to-scale schematic diagram of the samples. (b) SEM image of Sample B. [9]
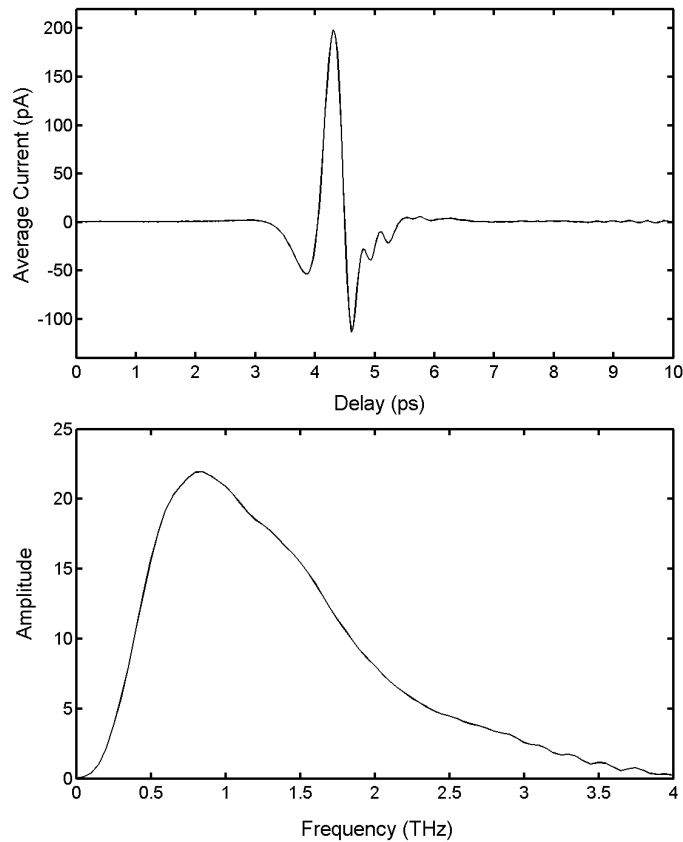
Figure 5-11. Transmitted THz pulse through the Reference Sample and the corresponding amplitude spectrum. [9]

This TM_0 mode selectivity is due to the following properties. For the linear THz polarization perpendicular to the waveguide plates, coupling is possible only to the TM modes, which is described in section 4.2. For the 80 μm plate separation, the cutoff frequencies of the TM_1, TM_2, and TM_3 modes are 1.88, 3.75 and 5.62 THz, respectively. The overlap integral of the focused incoming THz beam with the TM_1 mode at the waveguide face is zero by symmetry arguments, thereby giving no coupling. Furthermore, for the TM_2 mode, the THz beam at focus is broad enough so that the overlap integral is very small and coupling is negligible. Finally, our spectral range is below cutoff frequency for the TM_3 mode of 5.62 THz.

63
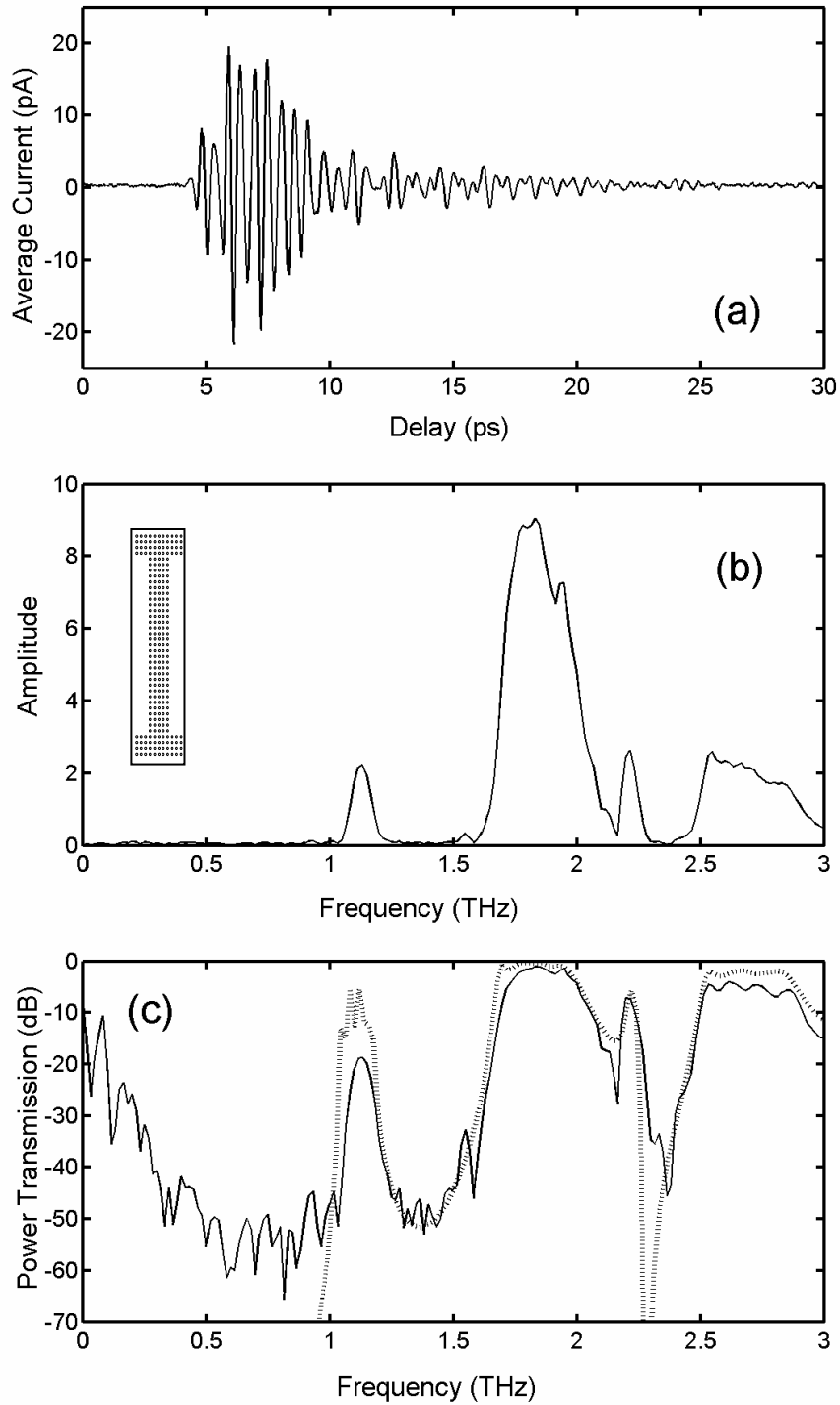
Figure 5-12. (a) Transmitted THz pulse through Sample A. (b) Amplitude Spectrum of transmitted THz pulse. (c) Power transmission in dB of Sample A (solid line) and numerical simulation (dotted line). [9]

64

Figures 5-12(a) and 5-12(b) show the transmitted THz pulse through Sample A and the corresponding amplitude spectrum. The transmitted pulse from the sample has a ringing structure extending to 25 ps. There is a small 0.2 ps propagation delay of the sample pulse with respect to the reference pulse. From the spectrum, it is clear that the first two bandgaps extend from low frequency to 1.0 THz and from 1.2 THz to 1.6 THz.

We simulated the results with TMM software [65]. The dielectric constant of metal is frequency dependent and negative. It is difficult to apply this kind of dielectric constant in to TMM. As sections 3.4 and 5.2 mentioned, the plasma frequency ω_p and damping frequency ω_τ can be related to the dielectric constant. The metallic photonic crystal simulation (TMM) employs these two parameters instead of the dielectric constant. For Au, ω_p= 2175 THz, ω_τ = 6.5 THz.

Fig. 5-12(c) compares the measured power transmission of Sample A and the simulated power transmission of a 5-C solid Au sample. Beyond 1 THz the results fit very well. However, below 1 THz, there is significant difference considered to be due to the finite thickness of the metal film. The THz waves can penetrate the 150 nm Au film (leakage) when the skin depth is greater than the film thickness; the skin depth is inversely proportional to the square root of frequency. For example, the skin depth of Au is 102 nm at 0.5 THz. If we take -30 dB as the threshold, the measured band gaps are from 0.22 to 1.07 THz and from 1.20 to 1.62 THz. In comparison, the calculated band gaps are from 0 to 1.03 THz and from 1.19 to 1.60 THz. The corresponding positions of the dips and peaks of the experimental results are in good agreement with the calculated results.
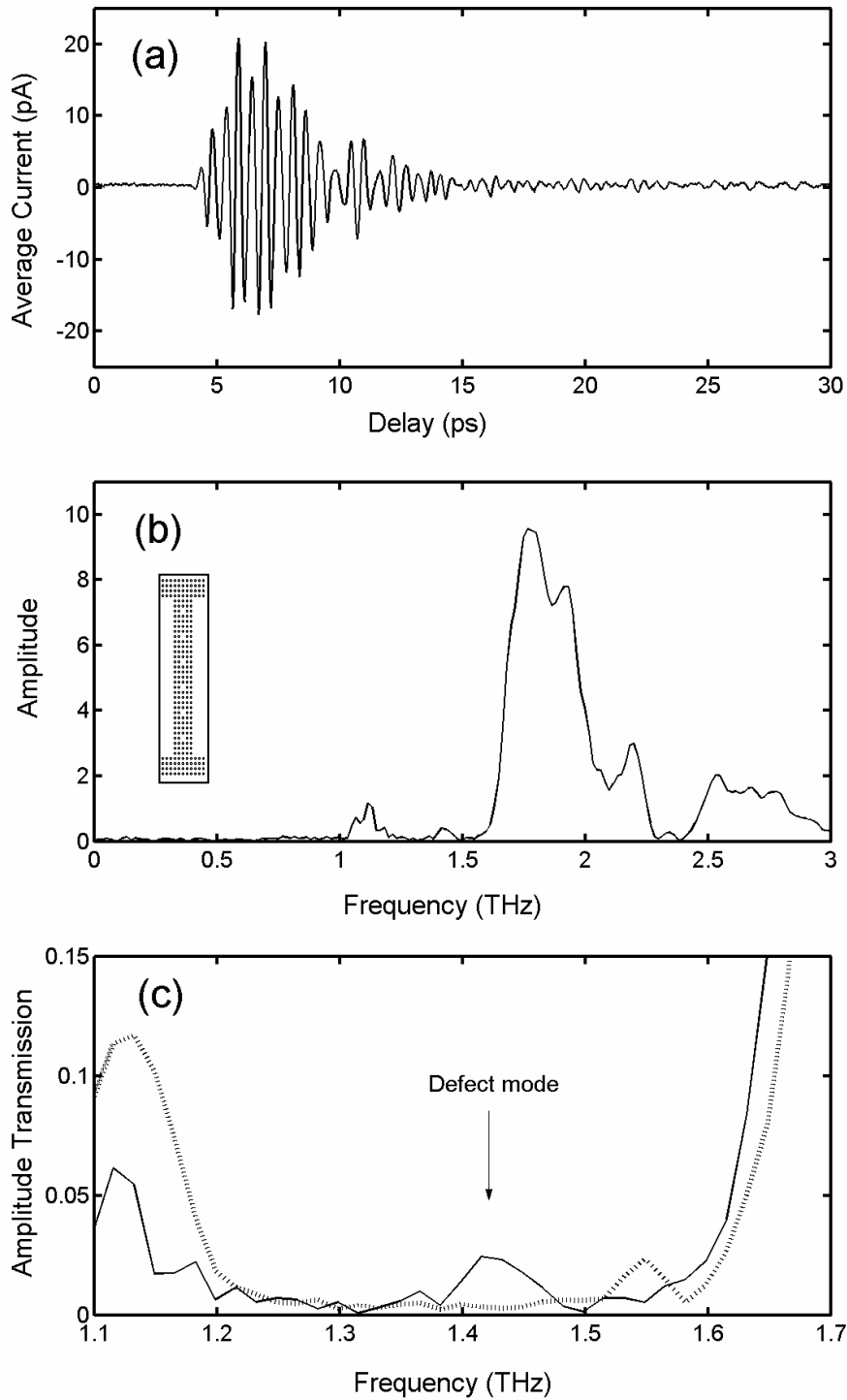
Figure 5-13. (a) Transmitted THz pulse through Sample B. (b) Amplitude spectrum of transmitted pulse. (c) Amplitude transmission of Sample B (solid line) compared to Sample A (dotted line). [9]

66

Figures 5-13(a) and 5-13(b) show the transmitted THz pulse and the corresponding amplitude spectrum from Sample B. Figure 5-13(c) compares the amplitude transmission of Sample A with Sample B. The transmissions are similar, except that for Sample B there is a peak (defect mode) at 1.42 THz in the second bandgap from 1.2 THz to 1.6 THz. The peak has 2.5% amplitude transmission. Similar metallic photonic structures (solid copper rods, r/a = 0.2) have been theoretically studied using the finite-difference time domain method [63]. In that work, the resonant frequency for one defect mode is given by the numerical result $f_0 = 0.753(c/a)$, where c is the speed of light [63]. For our case, the corresponding theoretical frequency is 1.412 THz, in good agreement with our observation of 1.42 THz (gold coated rods, r/a = 0.22).

To gain higher transmission of the defect mode, Sample C with the F-P defect was measured. Figures 5-14(a) and 5-14(b) show the transmitted THz pulse and the corresponding amplitude spectrum for Sample C. Here, the peak pulse amplitude and peak transmitted spectra are clearly larger than for Sample A, thereby demonstrating the transmission enhancements of the F-P defect. Figure 5-14(c) shows the comparison of the amplitude transmissions of Sample A and Sample C. Similar to the amplitude transmission of Sample B, there is a peak (defect mode) in the second bandgap from 1.2 THz to 1.6 THz of Sample C. The position of this peak at 1.46 THz has shifted about 0.04 THz from the result of Sample B, because of mode coupling effects [22] and experimental variation.
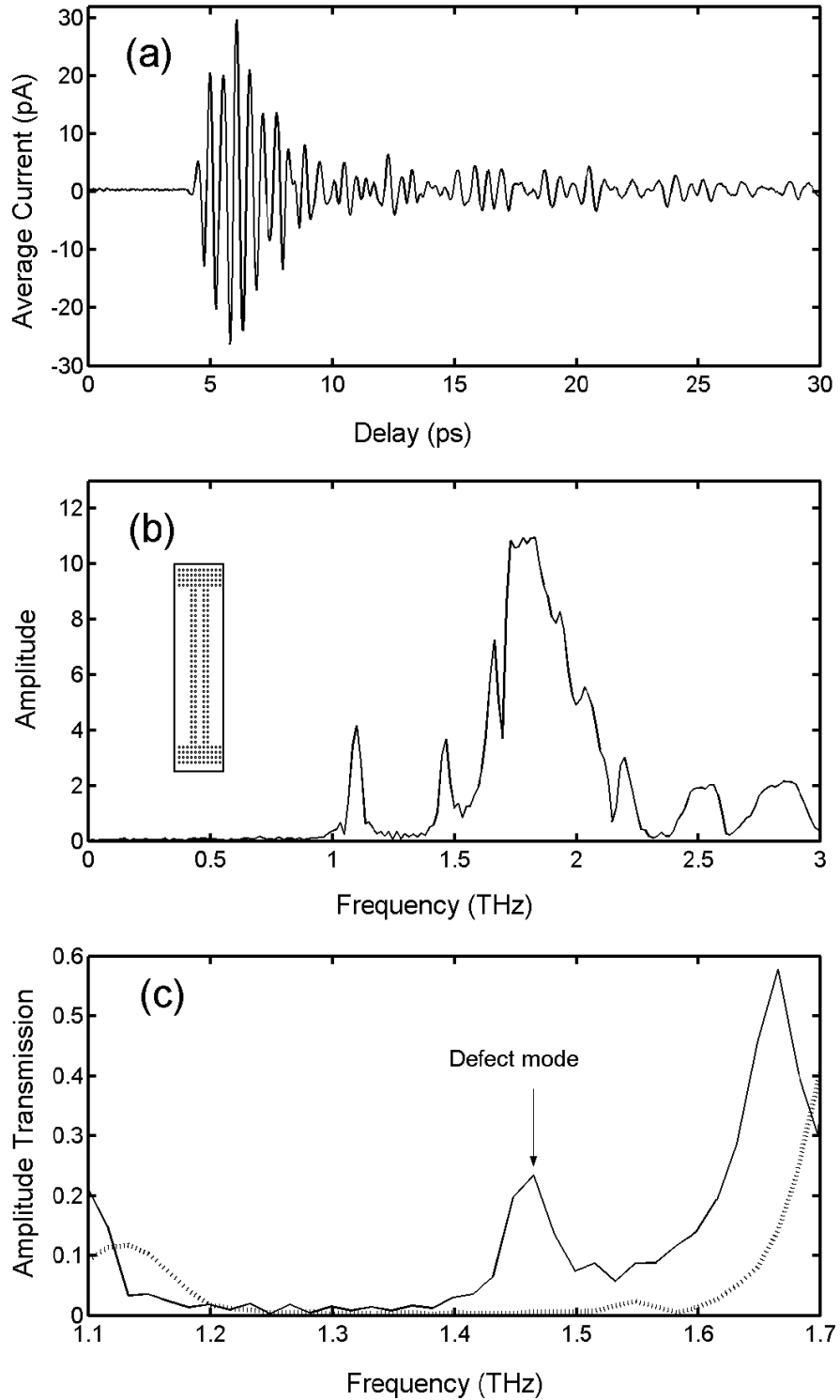
Figure 5-14. (a) Transmitted THz pulse through Sample C. (b) Amplitude spectrum of transmitted pulse. (c) Amplitude transmission of Sample C (solid line) compared to Sample A (dotted line). [9]

The peak with 22% amplitude transmission shows a very strong localization effect compared with the point defect of Sample B. The defect mode frequency f_r in the F-P defect can be calculated by the F-P resonance condition $f_r = (2m\pi - \phi)c/(4\pi L)$, where m is the mode number, ϕ is the total phase contribution of two mirrors, and L is the separation between the mirrors ($L = 160$ μm) [22]. For the defect mode at 1.46 THz, m is evaluated as 2 and ϕ as 159 degrees.

For completeness, we compare these results with our unsuccessful attempt to create and characterize 2D metallic photonic crystals in the PPWG by THz-TDS [44]. Initially, we used a 2D photonic crystal of sputtered metal coated cylinders, 70 μm tall, 70 μm diameter, and arranged on a 160 μm square lattice, lithographically fabricated on a 25.4mm-square Si plate. This 25.4 mm long structure filled the space between the plates of the PPWG. However, due to the large number of metal coated columns (n=160), the THz transmission through this structure was not observable. In order to obtain some transmission, we broke the 2D symmetry by increasing the space between the waveguide plates to let the tops of the metal coated cylinders form the surface of a 100 μm air gap to the second plate. For this (theoretically undescribed) new class of air-spaced parallel plate photonic waveguides, we observed strong photonic transmission effects, with stop bands or transmission having contrasts of as much as 90 dB [44].

The measurements and characterizations of effectively 2D metallic photonic crystals have been presented in the THz range. Wide bandgaps from 0 THz to 1.0 THz and from 1.1 THz to 1.6 THz were realized in the metallic photonic crystals, which fit well with the simulation results. Strong localizations of the point defect mode and the F-P defect were also observed. The convenient fabrication method and powerful metal PPWG setup

69

may enable applications, such as THz metallic photonic crystal cavities and photonic networks.

The fact that these 2D photonic crystal structures were lithographically fabricated using custom designed lithographic masks, demonstrates that any 2D photonic crystal geometry consistent with the broad applicability of lithography can be achieved. Furthermore, the fact that the theoretical simulations agree with experiment will allow for accurate simulations of proposed structures, before mask design and fabrication. Consequently, this work shows the possibility of design and fabrication of 2D photonic crystals within the PPWG with specified frequency-dependent transmission.

CHAPTER VI

APPLICATIONS OF THZ PHOTONIC CRYSTALS

6.1   Metallic photonic crystal waveguide

We tried to remove one row to see the response of the single line guide in photonic crystal structures, which is also called as photonic crystal waveguide. The theory shows that there are guided modes in a 2D metallic photonic crystal waveguide [66]. The cutoff frequency and consequently a mode gap at low frequencies existed in the metallic photonic crystal waveguide. By comparing with the conventional metallic rectangular waveguide, the main difference between them is due to the loss of the translational symmetry in metallic photonic crystal waveguide.
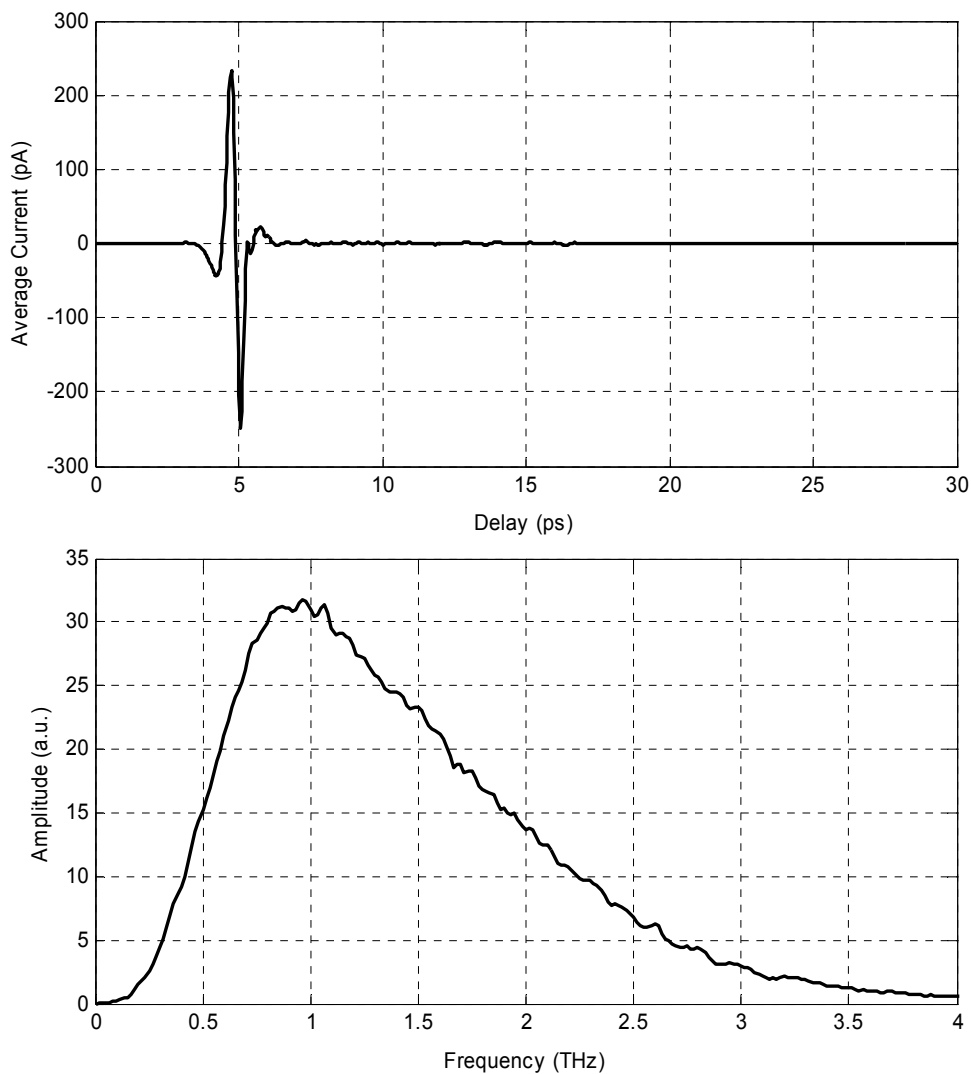
Figure 6-1. Measured reference THz pulses

Fig. 6-1 shows the reference pulse and spectrum of this experiment from blank chip. The setup is the same as the setup of section 5.2. The photonic crystal waveguide uses the same cylinders coated by Au. A 4-C sample with periodicity of 160μm, cylinder diameter of 70μm and cylinder height of 70μm, one row is removed in the center, as shown in the inset of Fig. 6-1.
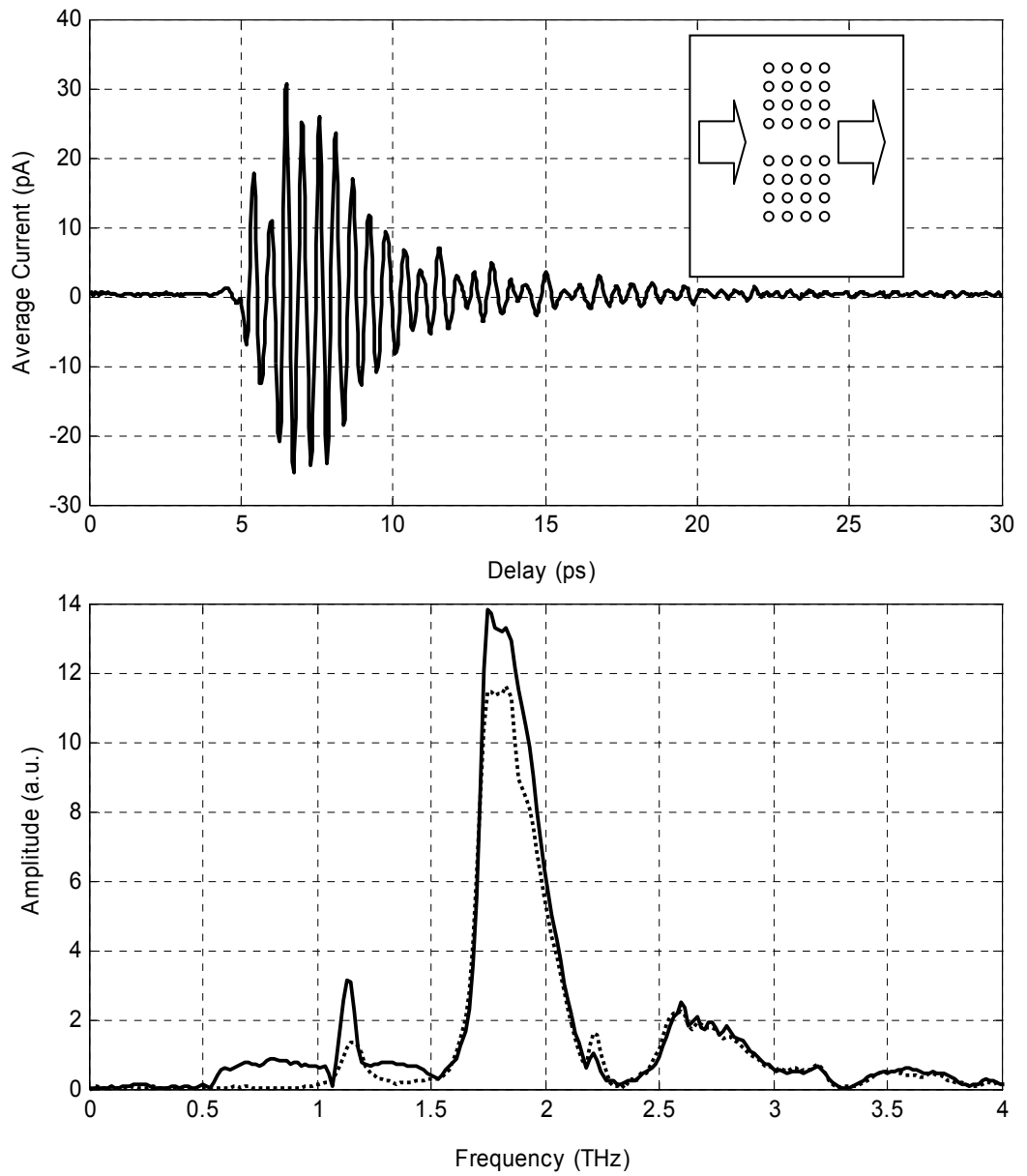
Figure 6-2. Measured 4-C Au with line defect transmitted THz pulses, the dot line is the spectrum of 4-C Au without line defect; the inset shows the schematic of 4-C waveguide.
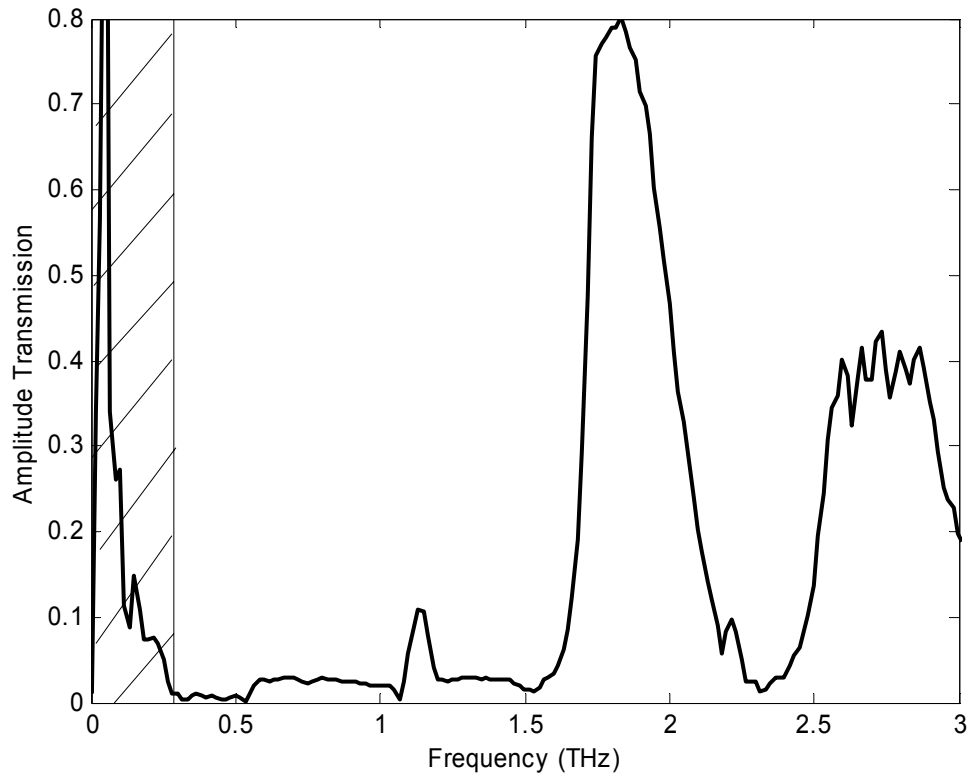
Figure 6-3. Measured amplitude transmission for the 4-C Au with line defect sample

Fig. 6-2 shows the measured pulse and spectrum from the 4-C Au sample with one line removed. With comparing to the spectrum of 4-C Au without line defect (dot line in Fig. 6-2), there are some transmission in the first gap from 0.53 to 1.0 THz and the second gap from 1.2 to 1.5 THz. The amplitude transmission of the sample is shown in Fig. 6-3, where the transmission between two gaps can be clearly seen.
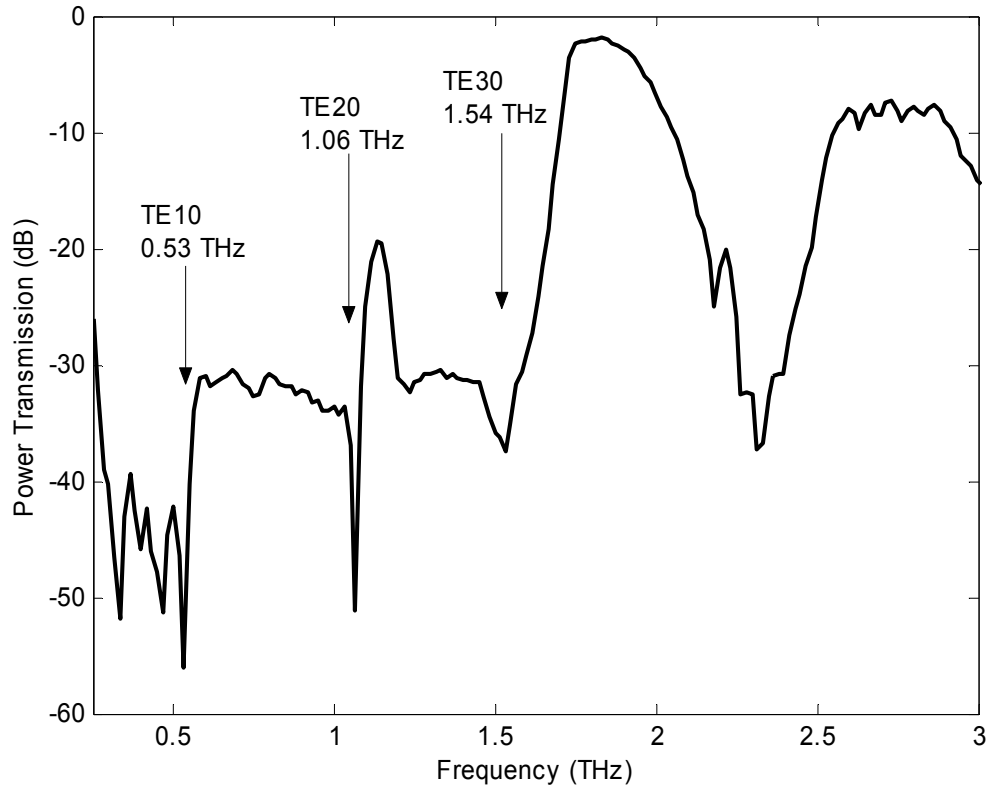
Figure 6-4. Measured power transmission for the 4-C Au with line defect sample

Fig. 6-4 shows the power transmission of the sample. The cutoff frequencies in the dB graph can easily be found.

The cutoff frequency of rectangular waveguide is

$$f_c = \frac{1}{2\pi\sqrt{\mu\varepsilon}} \sqrt{\left(\frac{m\pi}{a}\right)^2 + \left(\frac{n\pi}{b}\right)^2}$$

$$= \frac{c}{2\pi} \sqrt{\left(\frac{m\pi}{a}\right)^2 + \left(\frac{n\pi}{b}\right)^2} \qquad \text{for free space} \qquad (48)$$

Where a is the width of the waveguide and b is the height of the waveguide.

For lowest mode TE$_{10}$, m=1 and n=0, $f_c = \dfrac{c}{2a}$.

When one row is removed from the 160μm periodic lattices, the effective width of photonic crystal waveguide should be between 250μm (the edge to edge of cylinders) and 320μm (the center to center of cylinders). The experimental cutoff frequency is about 0.53 THz. The effective width from the above equation is about 283μm. For 250μm and 320μm, the calculated cutoff frequency is 0.6 THz and 0.47 THz, respectively. Apparently, the experimental result can be explained by the rectangular waveguide theory with effective width. Ref. 66 mentions the calculated result is about 0.278(c/a), which corresponds to 0.52 THz in our case. There also exist dips at 1.06 THz and 1.54 THz, which correspond to the cutoff frequencies of TE_{20} and TE_{30}.

We noticed the transmitted power from the waveguide is very weak. The reason of that is the coupling in THz beam through the plano-cylindrical silicon lens is a line source instead of a point source. Most of the coupled power is consumed by the standard 4-C photonic crystal structure. The future setup using a spherical silicon lens is under test. In that case, the point source can couple more power into the waveguide.

6.2 Tunable photonic bandgap realization

It is well known that the photonic crystals have ability that can manipulate the propagation wave [1, 2, 67]. The most important property of photonic crystals is the photonic bandgaps. The bandgaps in photonic crystals depend on the periodic pattern, properties of construction materials, such as the dielectric constants, the plasma frequencies. Recently, there has been growing interest in the realization of tunable photonic bandgap, because there are many important applications by using tunable

structures, such as filtering, switching and photonic devices. Therefore, many practical methods are proposed to control the photonic bandgap. These proposals include the modifying of the external magnetic field [92], the tuning of magnetic permeability [93] and dielectric permittivity [94], the changing of plasma frequency [95], and the structure changing of the photonic crystals by strain [96].

Here, we propose an easy method to realize the photonic bandgap tuning by changing the air gap between the top of the two dimensional (2D) metallic photonic crystal structures and the cover metal plate, which are bounded in parallel plate waveguide (PPWG). The bandgap by this way can be controlled from 0.062 THz to 0.918 THz. This structure can be compared to our early work on the air-spaced, broken-symmetry photonic PPWG [44], which showed sharp responses in regions as large as 1 THz. For standard metallic photonic crystals, it has large bandgap, light weight, and smaller size [4]. These advantages are suit for the photonic device design. For periodic boundary condition waveguide, the mathematical model can be thought as a cascade connection of equivalent impedance networks [97]. And the propagated wave depends on these impedances, which are determined by the physical conditions of the waveguide, such as the gap distance, periodicity, and so on. With the air gap appearing between the photonic crystal structures and the cover metal plate, the situation becomes complicated. The transmitted wave in this case will combine the effects of pure metallic photonic crystal structures and the effects of the waveguide with periodic boundary conditions, and it is hard to fit with any existing theory.
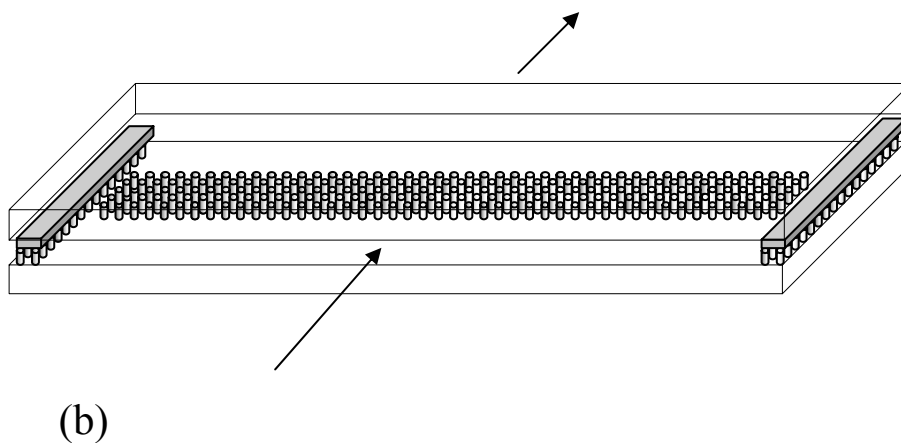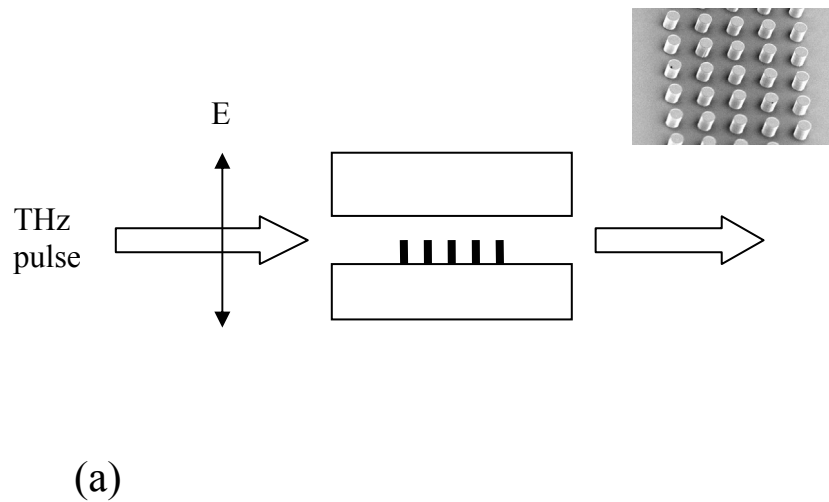
Figure 6-5. Not to scale schematic diagram showing THz propagation direction perpendicular to the columns of the array. (a) Cross section diagram. The inset is SEM image of part of 5 columns sample. (b) Three dimension experimental setup diagram. The air gap is changed by replacing different spacers.

The tunable 2D photonic crystal structure was completed by placing a polished Al plate over and in contact with the top of the array of standing metallic cylinders. Edge spacers are placed between the Al plate and the top of the metallic photonic crystal

78

surface. As shown in Fig. 6-5(a), the THz pulse propagation is perpendicular to the columns of cylinders in the (10) direction of square pattern with the polarization parallel to the cylinders. The resulting tunable photonic crystal structure centered within the 10 mm-long PPWG (Fig. 6-5(b)) were characterized by the standard THz-TDS system [8]. Two plano-cylindrical high-resistivity silicon lenses are used to couple the radiation into and out of the waveguide setup, placed at the confocal beam waist of the THz-TDS system [84]. The lenses are 15 mm x 10 mm x 6.56 mm with a 5 mm radius of curvature. The input lens focuses the incoming THz radiation to an elliptical spot with a frequency independent minor axis of 150μm, perpendicular to the waveguide plates, and a linearly wavelength-dependent major axis parallel to the plates with a 1/e amplitude diameter d = 9 mm at 1 THz. The THz experimental arrangement converts the incident 3D plane wave from the THz transmitter into an incident 2D line wave matched to the waveguide and couples the waveguide output 2D line wave into an outgoing 3D plane wave which is then efficiently coupled into the THz receiver.
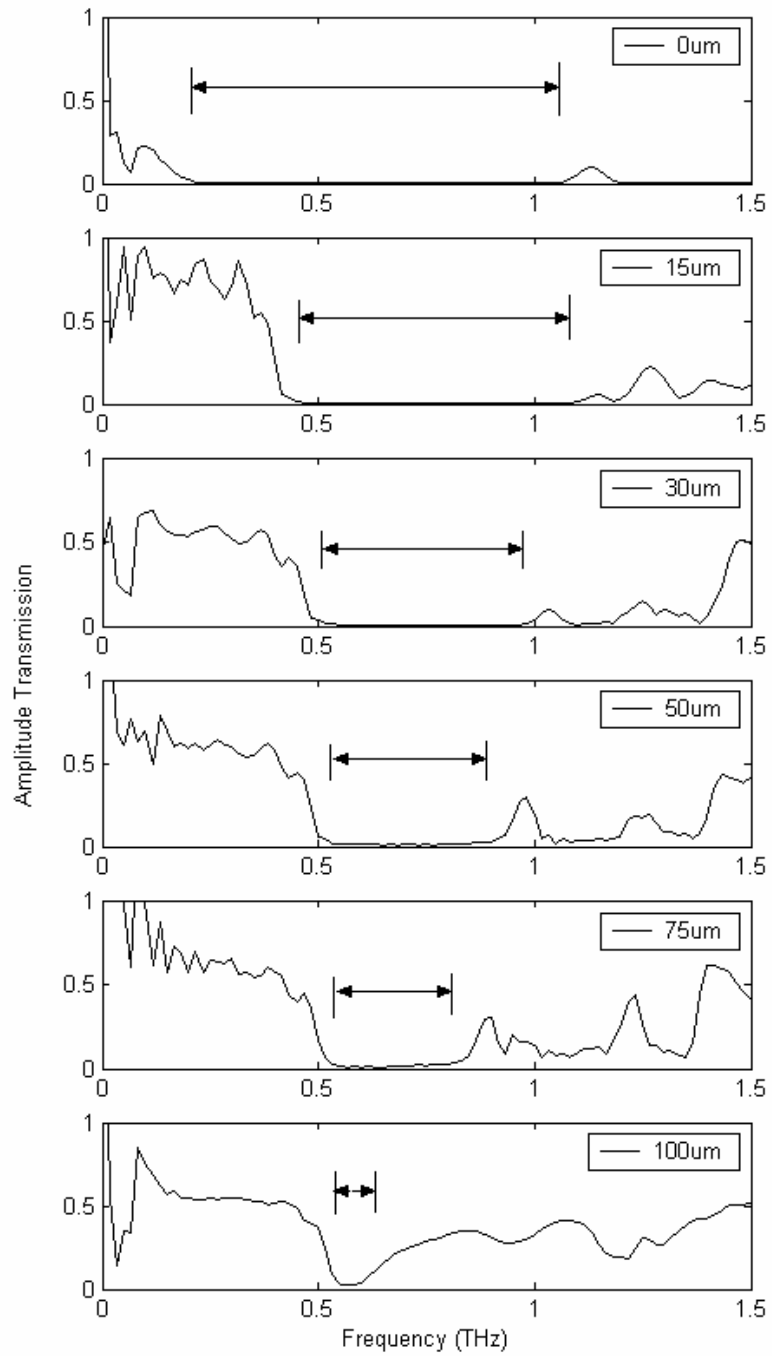
Figure 6-6. Measured amplitude transmission with the air gap of 0μm, 15μm, 30μm, 50μm, 75μm, and 100μm, respectively.
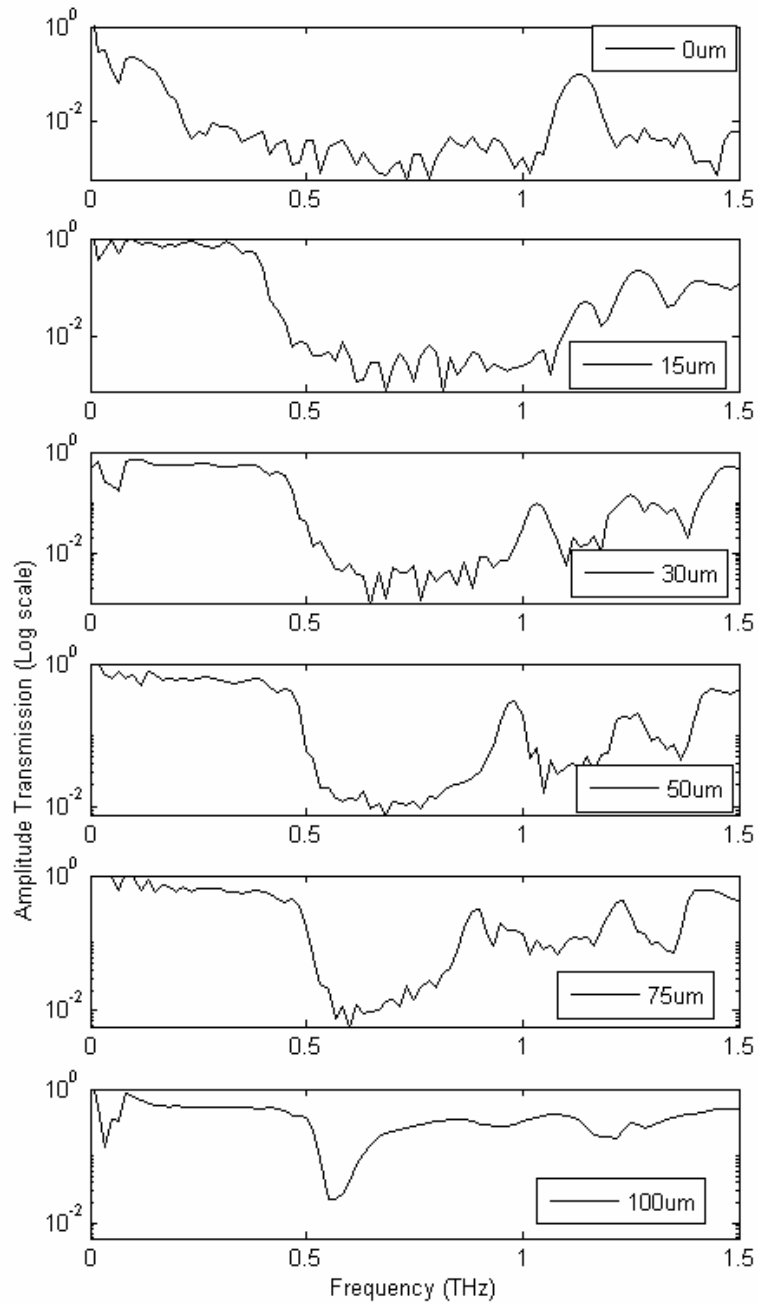
Figure 6-7. Measured amplitude transmission (Log scale) with the air gap of 0μm,

15μm, 30μm, 50μm, 75μm, and 100μm, respectively.

Fig. 6-6 shows the amplitude transmissions from 0 to 1.5 THz with the air gap from 0μm to 100μm. The THz reference pulse and spectrum was measured by the standard PPWG with 80μm air gap, which is the height of the cylinders. The pulses and spectra of the sample were measured by changing the spacer thickness, 0μm, 15μm, 30μm, 50μm, 75μm, and 100μm, respectively. The amplitude transmissions are achieved by the ratios of the sample spectrum and the reference spectrum, $T(f) = S(f) / R(f)$, where $T(f)$ is amplitude transmission, $S(f)$ is sample spectrum and $R(f)$ is reference spectrum. Fig. 6-7 uses log scale to show this bandgap change more clearly. The wave coupled into the PPWG has single TEM mode because the cutoff frequency of that single mode in PPWG for maximum couple gap 80μm (columns) + 100μm (air) = 180μm is 1.67 THz [84], where the maximum frequency 1.5 THz in the measurement is in the single mode range. This single mode situation enables the capability of the two dimensional structures to simulate the infinitely long three dimensional structures [86], consisting of two infinitely-long identical column arrays separated by twice the air gap. Obviously, the first bandgap shown in Fig. 6-6 and Fig. 6-7 is narrowing and the band edge is changing with increasing air gap.
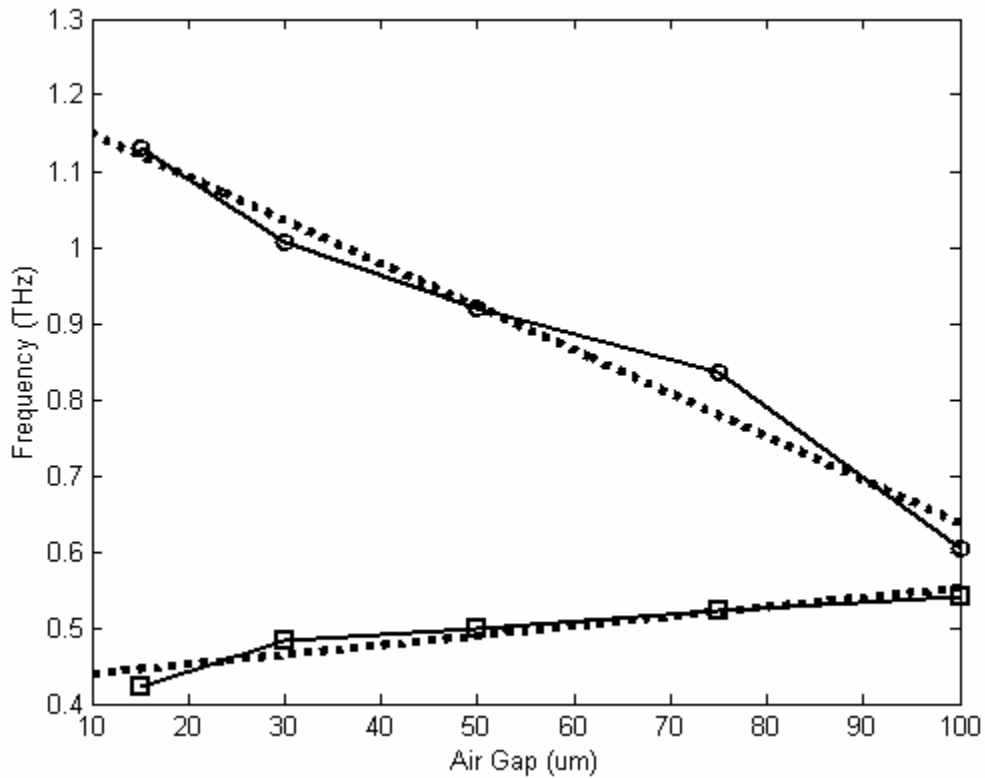
Air gap (μm)	Lower band edge (THz)	Upper band edge (THz)	Bandgap (THz)
0	0.176	1.094	0.918
15	0.422	1.130	0.708
30	0.482	1.006	0.524
50	0.500	0.920	0.420
75	0.522	0.836	0.314
100	0.542	0.604	0.062

Figure 6-8. The plot of the measured (solid lines) and linear fitted (dotted lines) lower and upper band edges as a function of the air gap from 10μm to 100μm. The table shows the value of band edges and band width by using 5% amplitude transmission as a threshold.

Fig. 6-8 shows the plot of the bandgap changing. The table lists the values of the band edges and bandgaps with the different air gap. These values use 5% (-13dB) amplitude

transmission as the threshold, which was selected for comparison conveniently. The lower and upper band edge plots demonstrate the linear relationship between the air gap and the frequency. The measured results in solid lines and the linear fit in dotted lines of Fig. 6-7 indicate the realization of the bandgap tuning. Except the result of the air gap of 0um, the band edge changing is basically linear. The upper band edge drops very fast from 1.13 THz with 15μm gap to 0.604 THz with 100μm gap. And the lower band edge raises slowly from 0.422 THz with the 15μm gap to 0.542 THz with 100μm gap. The total photonic bandgap is changed from 0.708 THz to 0.062 THz.

According to the measurement results, the tunable THz photonic crystal device can be realized by replacing the edge spacers with the piezoelectric actuators to control the air gap. With the precise air gap adjustment, the certain bandgap will be achieved. If the photonic crystal pattern and size are changed, the various bandgap changing speed and width should be easily observed. It is believable that this tunable structure can apply to the microwave and optical regime due to the scaling principle.

CHAPTER VII

CONCLUSIONS

In this thesis, the concepts of photonic crystals are first introduced. The PWE approach is the basic method to analyze the band structure of photonic crystals. The dielectric photonic crystal structures without loss are easy to apply in the PWE method. For lossy and dispersive materials and more complex structures, FDTD and TMM are better choices.

Our fabrication capability of making THz chips enables us to apply photonic crystal structures easily. The integration of the MEMS method and traditional lithography shows its advantage in making the dielectric and metallic photonic crystal structures. The very high aspect ratio structures are formed by this approach and the almost ideal properties are shown in these structures.

We demonstrated the 2D THz polymer (SU-8), which shows the bandgaps from 0.81 to 0.91 THz and 1.5 to 1.84 THz at the (10) incident direction. These effectively 2D photonic bandgap structures are embedded in THz PPWG setup and show the comparable results with ideal infinite structures. This experiment demonstrated that the bounded space between metal PPWG can be used to create physical embodiments of effectively 2D THz TEM-mode propagation experiments. The same setup was also used in metallic photonic crystal structures, which show wide bandgaps from 0 to 1.0 THz and from 1.1 to

1.6 THz. For the point defect and F-P defect photonic structures, the strong localization (defect modes) are investigated. The experimental results matched the simulation results very well. The advantages of the single mode PPWG and the quasi-optic coupling method give us a powerful tool to simulate infinite 2D ideal photonic crystal structures, and to do further research of THz photonic crystal structures.

Some applications are demonstrated in this thesis. THz metallic photonic crystal waveguide is tested in the PPWG setup and shows obvious cutoff frequencies which corresponded to the rectangular metal waveguide. We also report the experimental realization of a tunable THz photonic bandgap structure. The tunable structure is built inside the PPWG and operates by changing the air gap, with air gap changing between the top of the metallic photonic crystal slab and the cover metal plate. The photonic bandgap can be linearly controlled by adjusting the distance of the air gap. The bandgap adjustable from 0.062 THz to 0.918 THz is achieved by using this method.

REFERENCES

1. E. Yablonovitch, "Inhibited spontaneous emission in solid-state physics and electronics," Phys. Rev. Lett., Vol. 58, 2059, 1987.

2. S. John, "Strong localization of photons in certain disordered dielectric superlattices", Phys. Rev. Lett., Vol. 58, 2486, 1987.

3. J. D. Joannopoulos, R. D. Meade, and J. N. Winn, "Photonic Crystals: Molding the Flow of Light". Princeton, NJ: Princeton Univ. Press, 1995.

4. D. R. Smith, S. Schultz, N. Kroll, M. Sigalas, K. M. Ho, C. M. Soukolis, "Experimental and theoretical results for a two-dimensional metal photonic band-gap cavity", Appl. Phys. Lett., Vol. 65, 645, 1994.

5. S. –Y. Lin, E.Chow, V. Hietala, P.R. Villeneuve, J. D. Joannopoulos, "Experimental Demonstration of Guiding and Bending of Electromagnetic Waves in a Photonic Crystal", Science, Vol. 282, 274, 1998.

6. D. R. Smith, Willie J. Padilla, D. C. Vier, S. C. Nemat-Nasser and S. Schultz, "A composite medium with simultaneously negative permeability and permittivity," Phys. Rev. Lett., Vol. 84, 4184, 2000.

7. Michael Scalora, Jonathan P. Dowling, Charles M. Bowden, and Mark J. Bloemer, "The photonic band edge optical diode," J. Appl. Phys., Vol. 76, 2023, 1994.

8. Martin van Exter and D. Grischkowsky, "Characterization of an Optoelectronic Terahertz Beam System", IEEE Transactions on Microwave Theory and Techniques, Vol. 38, 1684, 1990.

9. Yuguang Zhao, D. Grischkowsky, "Two-dimensional THz Metallic Photonic Crystals in Parallel Plate Waveguides", Submitted to IEEE Transactions on Microwave Theory and Techniques (2006)

10. E. Yablonovitch, T. J. Gmitter, and K. M. Leung, "Photonic Band Structure: The Face-Centered-Cubic Case Employing Nonspherical Atoms," Phys. Rev. Lett., Vol. 67 (17), 2295, 1991.

11. E. Yablonovitch, T. J. Gmitter, R. D. Meade, A. M. Rappe, K. D. Brommer, and J. D. Joannopoulos, "Donor and Acceptor Modes in Photonic Band Structure," Phys. Rev. Lett., Vol. 67 (24), 3380, 1991.

12. S. L. McCall, P. M. Platzman, R. Dalichaouch, David Smith, and S. Schultz, "Microwave Propagation in Two-Dimensional Dielectric Lattices," Phys. Rev. Lett., Vol. 67 (15), 2017, 1991.

13. W. M. Robertson, G. Arjavalingam, R. D. Meade, K. D. Brommer, A. M. Rappe, and J. D. Joannopoulos, "Measurement of Photonic Band Structure in a Two-Dimensional Periodic Dielectric Array," Phys. Rev. Lett., Vol. 68 (13), 2023, 1992.

14. D. R. Smith, R. Dalichaouch, N. Kroll, S. Schultz, S. L. McCall and P. M. Platzman, "Photonic band structure and defects in one and two dimensions," J. Opt. Soc. Am. B, Vol. 10 (2), 314, 1993.

15. W. M. Robertson, G. Arjavalingam, R. D. Meade, K. D. Brommer, A. M. Rappe, and J. D. Joannopoulos, "Measurement of the photon dispersion relation in two-dimensional ordered dielectric arrays," J. Opt. Soc. Am. B, Vol. 10 (2), 322, 1993.

16. S. Y. Lin and G. Arjavalingam, "Photonic bound states in two-dimensional photonic crystals probed by coherent-microwave transient spectroscopy," Opt. Soc. Am. B, Vol. 11, 2124, 1994.

17. E. Ozbay, E. Michel, G. Tuttle, R. Biswas, M. Sigalas, and K. −M. Ho, "Micromachined millimeter-wave photonic band-gap crystals," Appl. Phys. Lett., Vol. 64 (16), 2059, 1994.

18. E. Ozbay, A. Abeyta, G. Tuttle, M. Tringides, R. Biswas, C. T. Chan, C. M. Soukoulis, and K. M. Ho, "Measurement of a three-dimensional photonic band gap in a crystal structure made of dielectric rods," Phys. Rev. B, Vol. 50 (3), 1945, 1994.

19. E. Ozbay, E. Michel, G. Tuttle, R. Biswas, K. M. Ho, J. Bostak, and D. M. Bloom, "Terahertz spectroscopy of three-dimensional photonic band-gap crystals," Opt. Lett., Vol. 19 (15), 1155, 1994.

20. E. R. Brown and O. B. McMahon, "Large electromagnetic stop bands in metallodielectric photonic crystals, " Appl. Phys. Lett., Vol 67 (15), 2138, 1995.

21. E. Ozbay, G. Tuttle, M. Sigalas, C. M. Soukoulis, and K. M. Ho, "Defect structures in a layer-by-layer photonic band-gap crystal," Phys. Rev. B, Vol. 51 (20), 13961, 1995.

22. E. Ozbay and B. Temelkuran, "Reflection properties and defect formation in photonic crystals," Appl. Phys Lett., Vol. 69 (6), 743, 1996.

23. Shawn-Yu Lin, V. M. Hietala, S. K. Lyo, and A. Zaslavsky, "Photonic band gap quantum well and quantum box structures: A high Q resonant cavity," Appl. Phys. Lett., Vol. 68 (23), 3233, 1996.

24. J. S. McCalmont, M. M. Sigalas, G. Tuttle, K. –M. Ho, and C. M. Soukolis, "A layer-by-layer metallic photonic band-gap structure," Appl. Phys. Lett., Vol. 68 (19), 2759, 1996.

25. E. Ozbay, B. Temelkuran, M. Sigalas, G. Tuttle, C. M. Soukoulis, and K. M. Ho, "Defect structures in metallic photonic crystals," Appl. Phys. Lett., Vol. 69 (25), 3797, 1996.

26. F. Gadot, A. Chelnokov, A. De Lustrac, P. Crozat, J. M. Lourtioz, D. Cassagne and C. Jouanin, "Experimental demonstration of complete photonic band gap in graphite structure," Appl. Phys. Lett., Vol. 71 (13), 1780, 1997.

27. Michael C. Wanke, Olaf Lehmann, Kurt Muller, Qingzhe Wen, and Michael Stuke, "Laser Rapid Prototyping of Photonic Band-Gap Microstructures," Science, Vol. 275, 1284, 1997.

28. A. Kao, K. A. McIntosh, O. B. McMahon, R. Atkins, and S. Verghese, "Calculated and measured transmittance of metallodielectric photonic crystals incorporating flat metal elements," Appl. Phys. Lett., Vol. 73 (2), 145, 1998.

29. C. Jin, B. Cheng, Z. Li, D. Zhang, L.M. Li, and Z.Q. Zhang, "Two dimensional metallic photonic crystal in the THz range," Opt. Commun., Vol. 166, 9, 1999.

30. F. Gadot, A. de Lustrac, J.-M. T. Brillat, A. Ammouche, and E. Akmansoy, "High-transmission defect modes in two-dimensional metallic photonic crystals," J. Appl. Phys., Vol. 85 (12), 8499, 1999.

31. G. Guida, T. Brillat, A. Ammouche, F. Gadot, A. De Lustrac and A. Priou, "Dissociating the effect of different disturbances on the band gap of a two-dimensional photonic crystal," J. Appl. Phys., Vol. 88 (8), 4491, 2000.

32. Hideaki Kitahara, Naoki Tsumura, Hirotaka Kondo, Mitsuo Wada Takeda, Joseph W. Haus, Zhenyu Yuan, Noriko Kawai, Kazuaki Sakoda, and Kuon Inoue, "Terahertz wave dispersion in two-dimensional photonic crystals," Phys. Rev. B, Vol. 64, 045202-1, 2001.

33. B. Temelkuran, Mehmet Beyindir, E. Ozbay, J. P. Kavanaugh, M. M. Sigalas and G. Tuttle, "Quasimetallic silicon micromachined photonic crystals," Appl. Phys. Lett., Vol. 78 (3), 264, 2001.

34. Mehmet Bayindir, E. Cubukcu, I. Bulu, T. Tut, E. Ozbay, and C. M. Soukoulis, "Photonic band gaps, defect characteristics, and waveguiding in two-dimensional disordered dielectric and metallic photonic crystals," Phys. Rev. B, Vol. 64, 195113-1, 2001.

35. N. Katsarakis, M. Bender, L. Singleton, G. Kiriakidis and C. M. Soukoulis, "Two-dimensional metallic photonic band-gap crystals fabricated by LIGA," Microsystem Tech., Vol. 8, 74, 2002.

36. Ali Serpenguzel, "Transmission Characteristics of Metallodielectric Photonic Crystals and Resonators," IEEE Microwave and Wireless Components Letters, Vol. 12 (4), 134, 2002.

37. Philippe Gay-Balmaz, Claudio Maccio, and Olivier J. F. Martin, "Microwire arrays with plasmonic response at microwave frequencies," Appl. Phys. Lett., Vol. 81 (15), 2896, 2002.

38. Shao-Wei Wang, Wei Lu, Xiao-Shuang Chen, Zhi-Feng Li, Xue-Chu Shen, and Weijia Wen, "Two-dimensional photonic crystal at THz frequencies constructed by metal-coated cylinders," J. of Appl. Phys., Vol. 93 (11), 9401, 2003.

39. Dongmin Wu, Nicholas Fang, Cheng Sun, and Xiang Zhang, Willie J. Padilla, Dimitri N. Basov, David R. Smith, and Sheldon Schultz, "Terahertz plasmonic high pass filter," Appl. Phys. Lett., Vol. 83 (1), 201, 2003.

40. Nathan Jukam and Mark S. Sherwin, "Two-dimensional terahertz photonic crystals fabricated by deep reactive ion etching in Si," Appl. Phys. Lett., Vol. 83 (1), 21, 2003.

41. Timothy D. Drysdale, Richard J. Blaikie, and David R. S. Cumming, "Calculated and measured transmittance of a tunable metallic photonic crystal filter for terahertz frequencies," Appl. Phys. Lett., Vol. 83 (26), 5362, 2003.

42. Z. Jian, J. Pearce, and D. Mittleman, "Defect modes in photonic crystal slabs studied using terahertz time-domain spectroscopy," Opt. Lett., Vol. 29 (17), 2067, 2004.

43. M. Golosovsky, Y. Neve-Oz, D. Davidov, and A. Frenkel, "Phase shift on reflection from metallodielectric photonic bandgap materials," Phys. Rev. B, Vol. 70, 115105-1, 2004.

44.   A. Bingham, Y. Zhao and D. Grischkowsky, "THz parallel plate photonic waveguides," Appl. Phys. Lett., Vol. 87, 051101-1, 2005.

45.   Zhongping Jian, Jeremy Pearce and Daniel M Mittleman, "Two-dimensional photonic crystal slabs in parallel-plate metal waveguides studied with terahertz time-domain spectroscopy," Semicond. Sci. Technol., Vol. 20, S300, 2005.

46.   Yuguang Zhao and D. Grischkowsky, "Terahertz demonstrations of effectively two-dimensional photonic bandgap structures," Opt. Lett., Vol. 31 (10), 1534, 2006.

47.   J. B. Pendry and A. MacKinnon, "Calculation of Photon Dispersion Relations," Phys. Rev. Lett., Vol. 69 (19), 2772, 1992.

48.   Arthur R. McGurn and Alexei A. Maradudin, "Photonic band structures of two- and three-dimensional periodic metal or semiconductor arrays," Phys. Rev. B, Vol. 48 (23), 17576, 1993.

49.   V. Kuzmiak, A. A. Maradudin, and F. Pincemin, "Photonic band structures of two-dimensional systems containing metallic components," Phys. Rev. B, Vol. 50 (23), 16835, 1994.

50.   M. M. Sigalas, C. T. Chan, K. M. Ho, and C. M. Soukoulis, "Metallic photonic band-gap materials," Phys. Rev. B, Vol. 52 (16), 11744, 1995.

51.   N. A. Nicorovici, R. C. McPhedran, and L. C. Botten, "Photonic band gaps for arrays of perfectly conducting cylinders," Phys. Rev. E, Vol. 52 (1), 1135, 1995.

52.   Toshio Suzuki and Paul K. L. Yu, "Dispersion relation at point L in the photonic band structure of the face-centered-cubic lattice with active or conductive dielectric media," J. Opt. Soc. Am. B, Vol. 12 (4), 583, 1995.

53.   Toshio Suzuki and Paul K. L. Yu, "Complex photonic band structures of a conductive metal lattice by a quadratic eigensystem," Opt. Lett., Vol. 20 (24), 2520, 1995.

54.   M. M. Sigalas, C. M. Soukoulis, C. –T. Chan, and D. Turner, "Localization of electromagnetic waves in two-dimensional disordered systems," Phys. Rev. B, Vol. 53 (13), 8340, 1996.

55.   J. B. Pendry, "Calculating photonic band structure," J. Phys.: Condens. Matter, Vol. 8, 1085, 1996.

56.   J. Carbonell, O. Vanbesien, and D. Lippens, "Electric field patterns in finite two-dimensional wire photonic lattices," Superlattices and Microstructures, Vol. 22 (4), 597, 1997.

57. G. Tayeb and D. Maystre, "Rigorous theoretical study of finite-size two-dimensional photonic crystals doped by microcavities," J. Opt. Soc. Am. A, Vol. 14 (12), 3323, 1997.

58. Manvir S. Kushwaha, "Stop-bands for periodic metallic rods: Sculptures that can filter the noise," Appl. Phys. Lett., Vol. 70 (24), 3218, 1997.

59. Lie-Ming Li, Zhao-Qing Zhang, and Xiangdong Zhang, "Transmission and absorption properties of two-dimensional metallic photonic-band-gap materials," Phys. Rev. B, Vol. 58 (23), 15589, 1998.

60. Lie-Ming Li and Zhao-Qing Zhang, "Multiple-scattering approach to finite-sized photonic band-gap materials," Phys. Rev. B, Vol. 58 (15), 9587, 1998.

61. Toshio Suzuki and Paul K. L. Yu, "Method of projection operators for photonic band structures with perfectly conducting elements," Phys. Rev. B, Vol. 57 (4), 2229, 1998.

62. S. G., Johnson, Shanhui Fan, P. R., Villeneuve, J. D., Joannopoulos, and L. A. Kolodziejski, "Guided modes in photonic crystal slabs," Phys. Rev. B, Vol. 60 (8), 5751, 1999.

63. Min Qiu, Sailing He, "Numerical method for computing defect modes in two-dimensional photonic crystals with dielectric or metallic inclusions," Phys. Rev. B, Vol. 61 (19), 12871, 2000.

64. M. Qiu and S. He, "A nonorthogonal finite-difference time-domain method for computing the band structure of a two-dimensional photonic crystal with dielectric and metallic inclusions," J. Appl. Phys., Vol. 87 (12), 8268, 2000.

65. Andrew L. Reynolds, Translight Software, based on the transfer matrix method (TMM), University of Glasgow, UK, Version Pre-Beta, Sep. 2000.

66. Min Qiu and Sailing He, "Guided modes in a two-dimensional metallic photonic crystal waveguide," Phys. Lett. A, Vol. 266, 425, 2000.

67. J. D. Joannopoulos, Pierre R. Villeneuve and Shanhui Fan, "Photonic crystals: putting a new twist on light," Nature, Vol. 386, 143, 1997.

68. I. El-Kady, M. M. Sigalas, R. Biswas, K. M. Ho, and C. M. Soukoulis, "Metallic photonic crystals at optical wavelengths," Phys. Rev. B, Vol. 62 (23), 15299, 2000.

69. B.-Y Shew, H.-C Li, C.-L Pan, and C.-H Ko, "X-ray micromachining SU-8 resist for a terahertz photonic filter", J. Phys. D: Appl. Phys. Vol. 38, 1097, 2005.

70. D. Wu, N. Fang, C. Sun, and X. Zhang, W. J. Padilla, D. N. Basov, D. R. Smith, and S. Schultz, "Terahertz plasmonic high pass filter", Appl. Phys. Lett., Vol. 83 (1), 201, 2003.

71. T. D. Drysdale, G. Mills, S. M. Ferguson, R. J. Blaikie, and D. R. S. Cumming, "Metallic tunable photonic crystal filter for terahertz frequencies", J. Vac. Sci. Technol. B, Vol. 21 (6), 2878, 2003.

72. C. Lin, C. Chen, G. J. Schneider, Z. Lu, and D. W. Prather, "Fabrication of terahertz two-dimensional photonic crystal lens on silicon-on-insulator", Proc. of SPIE, Vol. 5411, 116, 2004.

73. C. Lin, C. Chen, G. J. Schneider, P. Yao, S. Shi, A. Sharkawy, and D. W. Prather, "Wavelength scale terahertz two-dimensional photonic crystal waveguides", Optics Express, Vol. 12 (23), 5723, 2004.

74. H. Park, M. Cho, J. Kim, and H. Han, "Terahertz pulse transmission in plastic photonic crystal fibres", Phys. Med. Biol., Vol. 47, 3765, 2002.

75. J. W. Haus, P. Powers, P. Bojja, M. Torres-Cisneros, M. Scalora, M. Bloemer, N. Akozbek, and M. Meneses-Nava, "Terahertz generation in photonic crystals", Proc. of SPIE, Vol. 5354, 18, 2004.

76. H. Kurt, and D. S. Citrin, "Photonic crystals for biochemical sensing in the terahertz region", Appl. Phys. Lett., Vol. 87, 041108, 2005.

77. S. Guo, S. Albin, "Simple plane wave implementation for photonic crystal calculations," Opt. Express, Vol. 11, 167, 2003.

78. Kane S. Yee, "Numerical solution of initial boundary value problems involving maxwell's equations in isotropic media," IEEE Tran. on Antennas and Propagation, AP-14, No. 3, 302, 1966.

79. M. A. Ordal, R. J. Bell, R. W. Alexander, L. L. Long, and M. R. Querry, "Optical properties of fourteen metals in the infrared and far infrared: Al, Co, Cu, Au, Fe, Pb, Mo, Ni, Pd, Pt, Ag, Ti, V, and W," Appl. Opt., Vol. 24, 4493, 1985.

80. K. Inoue and K. Ohtaka, eds., "Photonic Crystals: Physics, Fabrication and Applications", Springer Series in Optical Sciences, Vol.94, Springer-Verlag, New York, 2004.

81. R. Gonzalo, B. Martinez, C. M. Mann, H. Pellemans, P. H. Bolivar, "A Low-Cost Fabrication Technique for Symmetrical and Asymmetrical Layer-by-Layer Photonic Crystals at Submillimeter-Wave Frequencies", IEEE Tran. on micro. theory and tech., Vol. 50 (10), 2384, 2002.

82. H. Lorenz, M. Despont, N. Fahrni, N. LaBlanca, R. Renaud, and P. Vettiger, "SU-8: a low-cost negative resist for MEMS," J. Micromech. Microeng., Vol. 7, 121, 1997.

83. Abul K. Azad, Y. Zhao and W. Zhang," Transmission properties of terahertz pulses through an ultrathin subwavelength silicon hole array" Applied Physics Letters, Vol. 86, 141102-1, 2005.

84. R. Mendis and D. Grischkowsky, "Undistorted guided wave propagation of sub-picosecond THz pulses," Opt. Lett., Vol. 26, 846, 2001.

85. R. Mendis and D. Grischkowsky, "THz Interconnect with Low Loss and Low Group Velocity Dispersion," IEEE Microw. Wirel. Compon. Lett., Vol. 11, 444, 2001.

86. S. Coleman and D. Grischkowsky, "A THz TEM-mode two dimensional interconnect layer incorporating quasi optics," Appl. Phys. Lett., Vol. 83, 3656, 2003.

87. S. Arscott, F. Garet, P. Mounaix, L. Duvillaret, J.-L. Coutaz and D. Lippens, "Terahertz time-domain spectroscopy of films fabricated from SU-8," Electronics Lett., Vol. 35, 243, 1999.

88. D. M. Whittaker, I S Culshaw, V N Astratov and M S Skolnick.,"Photonic bandstructure of patterned wave-guides with dielectric and metallic cladding", Phys. Rev. B, Vol. 65 (7), 073102, 2001.

89. E. Chow, S. Y. Lin, S. G. Johnson, P. R. Villeneuve, J. D. Joannopoulos, J. R. Wendt, G. A. Vawter, W. Zubrycki, H. Hou, and A. Alleman, "Three-dimensional control of light in a two dimensional photonic crystal slab," Nature, Vol. 407, 983, 2002.

90. Martin Van Exter and D. Grischkowsky, "Carrier dynamics of electrons and holes in moderately doped silicon," Phys Rev. B, Vol. 41 (17), 12140, 1990.

91. Alok Nayer, "The Metals Databook," McGraw-Hill, New York, 1997.

92. C. Xu, X. Hu, Y. Li, X. Liu, R. Fu, and J. Zi, "Semiconductor-based tunable photonic crystals by means of an external magnetic field," Phys. Rev. B, Vol. 68, 193201, 2003.

93. C.-S. Kee, H. Lim, Y.-K. Ha, J.-E. Kim, and H.Y. Park, "Two-dimensional tunable metallic photonic crystals infiltrated with liquid crystals," Phys. Rev. B, Vol. 64, 085114, 2001.

94. E. Yablonovitch and T. J. Gmitter, "Photonic band structure: The face-centered-cubic case," Phys. Rev. Lett., Vol. 63, 1950, 1989.

95. M. S. Kushwaha and B. Djafari-Rouhani, "Band-gap engineering in two-dimensional periodic photonic crystals," J. Appl. Phys., Vol. 88, 2877, 2000.

96. S. Kim and V. Gopalan, "Strain-tunable photonic band gap crystals," Appl. Phys. Lett., Vol. 78, 3015, 2001.

97. R. E. Collin, "Field Theory of Guided Waves", Ch. 9, IEEE press, 1991.

VITA

Yuguang Zhao

Candidate for the Degree of

Doctor of Philosophy

Thesis: STUDY OF PHOTONIC CRYSTAL STRUCTURES BY THz-TDS

Major Field: Electrical Engineering

Biography:

Personal Data: Born in Chongqing, China, son of Zexun Zhao and Huixiang Tan.

Education: Received the Bachelor of Science degree in Detection Techniques and Instruments from Northwest Polytechnic University, China, in July 1993; and received Master of Science degree in Multidisciplinary Science from Rensselaer Polytechnic Institute, Troy, NY, in August 2002. Completed the requirements for the Doctor of Philosophy of Science degree with a major in Electrical Engineering at Oklahoma State University in December 2006.

Experiences: Employed by Chongqing Sichuan Instrument Co., Ltd., China, as an electrical engineer, 1993 to 2001; employed by Rensselaer Polytechnic Institute, Department of Physics as a research assistant, 2001 to 2002; employed by Oklahoma State University, Department of Electrical Engineering as a research assistant, 2003 to present.

Name: Yuguang Zhao   Date of Degree: December, 2006

Institution: Oklahoma State University   Location: Stillwater, Oklahoma

Title of Study: STUDY OF PHOTONIC CRYSTAL STRUCTURES BY THz-TDS

Pages in Study: 95   Candidate for the Degree of Doctor of Philosophy

Major Field: Electrical Engineering

Scope and Method of Study: The purpose of this study was to examine the behavior of dielectric and metallic photonic crystal structures embedded in single mode metal parallel plate waveguide (PPWG). The terahertz (THz) pulse was coupled in and out by two plano-cylindrical silicon lenses. The photonic crystals were fabricated by using Micro-Electro-Mechanical-Systems (MEMS) technology, which constructed very high aspect ratio structures. The transmission properties of the THz radiation of these structures were investigated using terahertz time-domain spectroscopy (THz-TDS).

Findings and Conclusions: We demonstrated the transmitted THz bandgaps in the 2D polymer (SU-8) photonic crystal structures, 2D metallic photonic crystal structures and 2D metallic photonic crystal defect structures. The experimental results matched the transfer matrix method (TMM) and the finite difference time domain (FDTD) simulation results very well. A very important conclusion is that the advantages of single mode PPWG and the coupling method give us a powerful tool to simulate infinite 2D ideal photonic crystal structures. This method can be used to do the farther research of THz photonic crystal structures. Some applications such as photonic crystal waveguide and tunable photonic bandgap are also investigated and demonstrated.

ADVISER'S APPROVAL: _____ Dr. Daniel Grischkowsky _____